DOCTOR THESIS

Study of Effects of Donor-Acceptor Interaction in Silicon Nanoscale Co-Doped Devices

Chitra Pandy

Graduate School of Science and Technology

Department of Nanovision Technology

Shizuoka University

Japan

2021

博士論文

シリコンナノスケール共ドープデバイスにおける
ドナー-アクセプター相互作用効果の研究

チトラ　パンディ

静岡大学

大学院自然科学系教育部

令和 3 年

This thesis is submitted in partial fulfillment

of the requirements

for the degree of Doctor of Engineering,

Graduate School of Science and Technology

Shizuoka University

2021

Committee members:

Assoc. Professor Daniel Moraru (chairman)

Professor Hidenori Mimura (supervisor)

Professor Yukinori Ono

Professor Hirokazu Tatsuoka

Assoc. Professor Yoichiro Neo

Abstract

In order to achieve higher performance of the integrated circuits (ICs), a drive for continuous miniaturization of silicon (Si) electronic devices has brought the characteristic features of metal-oxide-semiconductor field-effect transistors (MOSFETs) to dimensions on the order of just a few nanometers. In such low-dimensionality, the device operation is known to be affected by a variety of factors, including fluctuations and discreteness of dopant distributions. Although such problems are typically seen as affecting the threshold voltage controllability, there have been numerous reports in past decade about the role of dopants as active units in electron transport and even as quantum dots (QDs). New mechanisms of tunneling (even at the level of single-electron tunneling) mediated by dopant-atoms (or clusters) can provide new opportunities for the next generation of electronics.

Tunneling is an even more critical phenomenon in devices such as tunnel field-effect transistors (TFETs), which propose to use band-to-band tunneling (BTBT) as the main mechanism for the on/off switching. BTBT transport is known for more than 60 years, reported from the tunnel (Esaki) diodes, which are pn diodes with very high doping concentrations. In such devices, it is expected that the depletion-layer width is naturally in the sub-10-nm regime. Moreover, with further miniaturization, the role of dopants in such nanoscale depletion-layers becomes even more significant. Such a mechanism would actually offer the opportunity to relax the momentum conservation condition that limits the BTBT rate and implicitly the “on” current in Si BTBT-devices.

This work addresses the above two fundamental types of devices from a theoretical perspective, combining first-principles (ab initio) and semi-empirical simulations of Si-nanowires containing discrete dopants. The simulation package used

allows the analysis of the density of states (DOS) spectra, transmission spectra, and also the simulation of the current-voltage characteristics based on the non-equilibrium Green's function (NEGF) approach.

First, this fundamental analysis is applied to nanoscale transistors (with a simplified structure) containing a few-dopant "cluster" between electrostatically-doped source and drain, without and with counter-dopants nearby. A main case focuses on a triple-P-donor cluster flanked by B-acceptors, all substitutionally introduced in the Si nanowire. It is found that the donor-cluster can contribute to the modulation of the coherent-transport with its discrete energy states, while the acceptors raise overall the potential in the channel, with a minor distortion to the cluster's energy spectrum. Although the electrical characteristics are only weakly dependent on the atomistic positions of the acceptors, they are found to be strongly sensitive to the number of acceptors introduced between the cluster and the leads (in so-called "barrier" regions).

Second and most importantly, an analysis is carried out on the impact of discrete dopants in BTBT transport in nanoscale pn diodes. After confirming the basic characteristics, the effect of a donor-acceptor (1P-1B) pair is investigated. It is found that, as the inter-dopant distance is increased, the current increases overall, most likely due to an increase in the coupling of each dopant to its respective lead. Inter-dopant coupling is also analyzed as a key parameter. From the various configurations studied, sharper enhancement of the current has also been observed in particular cases, ascribed to favorable situations when discrete energy states near leads (affected by the high electric field and by the presence of dopants) are aligned in such a way that the BTBT rate is significantly enhanced. The combination of the high electric field and discreteness of a donor-acceptor pair can reveal new phenomena that can further contribute to BTBT current, if understood more deeply.

Finally, a few experimental examples are provided from devices, such as co-doped nanoscale Si transistors or highly-doped Si pn (tunnel) diodes, fabricated in silicon-on-insulator (SOI). The examples of electrical characteristics have been selected as promising candidates to draw a tentative parallel between the theoretical and experimental analyses, despite the gap currently existing in terms of device dimensionality.

In summary, the results contained in this thesis illustrate, from a fundamental theoretical analysis, the strong and constructive impact that discrete dopants (in counter-doped Si-transistor nano-channels or in nanoscale depletion-layers of Si tunnel diodes) have on the DOS spectra and implicitly on the transport properties. As such, these findings may pave the way for utilizing counter-doping in Si-nanowire devices for developing new concepts for *dopant-based electronics* and other fields.

Acknowledgements

Thanks to almighty. It gives me immense pleasure to acknowledge and thank all the people who supported me and made this research possible at Research Institute of Electronics, Shizuoka University, Japan. Foremost, I would like to express my heartfelt gratitude to my supervisor Professor Hidenori Mimura, Director, Research Institute of Electronics, Shizuoka University for giving me an opportunity to come to Japan and extending his guidance both in research and work-life balance.

I would like to express my sincere gratitude and debt to my Co-supervisor, Associate Professor Daniel Moraru, Research Institute of Electronics, Shizuoka University for his contribution towards my research career and personal development cannot be understated. His technical insight into addressing research problem, enthusiasm, motivation, and infinite patience helped me to show more interest in my research work. Whenever I do mistakes technically, he is very patient and kind enough not only in correcting the mistakes but also in encouraging me to come out with more innovative ideas. Apart from these, he guided me on how to write a technical document, how to approach problems, and find solutions. I thank him for devoting his precious time to complete my final dissertation.

I must also thank Emeritus Professor Michiharu Tabe for his discussions and valuable guidance towards this research. His experience and wisdom have been utmost importance in my research progress and publications.

I would also like to thank Professor Hirokazu Tatsuoka, Professor Yukinori Ono, Professor Yoichiro Neo for their valuable comments, suggestions, and discussions on several points related to this research and thesis documentation.

My immense gratitude also lies with Keiko Kawai and Miki Masuda for their support on many matters ensuring a comfortable life in Japan. I am grateful for the essential contributions to this research and my life in Japan to former and present members and colleagues of both the Moraru Lab and the Mimura Lab: Taruna Teja Jupali, Ananta Debnath, Yuya Iwatsuki, Tsutomu Kaneko, Yuta Tamura. Special thanks to Gaurang Prabhudesai, Kensuke Yamaguchi for always providing me technical insights, support, and recommendations throughout my research work. Special thanks to Taku Miyake for his guidance and support towards my stay in Japan.

I cannot stop expressing my gratitude to my father, mother, brother, father-in-law, and mother-in-law for their love, support, encouragement, and prayers they have sent my way along this journey. Special thanks to my dear lovable husband, Prof V N Ramakrishnan, the man behind me, his encouragement, and valuable suggestions to improve my research, without his support, help, patience, and sacrifice this would have been impossible and unimaginable during this COVID-19 pandemic. Finally, special thanks to my sweet daughter Lakshanya Swathy and little smiling cute boy Lohitaksha Sai for making me stronger and more dedicated to this research than I could have ever thought of.

Contents

Chapter 1: Introduction

1.1. Research Background

1.1.1. The ultimate stages of Moore's law

The concept of the transistor as an "apparatus for controlling electric currents" has been proposed since 1930 by Lilienfeld,[1] but it was demonstrated by the team of Bardeen, Brattain and Shockley in 1947. This event represented a significant breakthrough because solid-state devices could now be used for on/off switching rather than the bulky, fragile and unstable vacuum tubes (as used until that point). After further development for semiconductor purification and fabrication technology, the concept of metal-oxide-semiconductor field-effect transistor (MOSFET) – a refined variant of transistor – was demonstrated and introduced in 1959-1960.[2]

Soon after, the integrated circuits (ICs) were proposed by J. Kilby and R. Noyce in the 1960s as complex and versatile concepts for high-performance electronics, coupling larger and larger numbers of such transistors into a chip. Owing to continuous improvement of the semiconductor fabrication technology (largely driven by the demand for increasing performance at reasonable costs and compact design), the ICs became the basic unit of the computational industry, promoted intensively by companies such as Intel (followed by others in the subsequent periods). Based on the data available at that time, Gordon Moore predicted the trend for miniaturization that became known as the Moore's Law, i.e., that the number of transistors per integrated chip doubles every 2-3 years (thanks to the significant technology breakthroughs).[3]

The MOSFETs (and other related electronic devices, downscaled based on the same Si technological platform) produced a revolution in terms of performance and scalability, leading to the Information Age that we currently experience. **Figure 1.1**

shows a schematic representation of the Moore's law, illustrating how the transistor's critical feature (gate length) has been reduced over the years; currently, the trend can be extended down to single-digit-nm dimensions, with a recent report from IBM about the development of transistors with 2-nm channel length.[4]

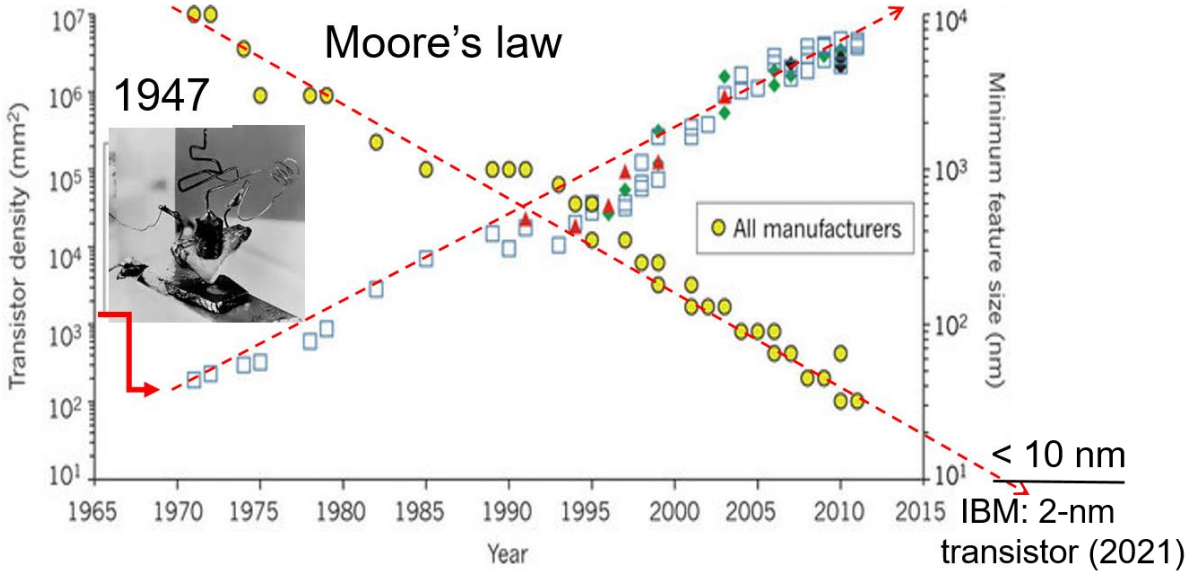

Fig. 1.1. A schematic outline from a common view of the Moore's Law, illustrating how the density of transistors per area increased dramatically by reduction of the minimum feature size (transistor channel). The history of the transistor spans the demonstration (1947, with the schematic shown on left) to the most recent report of a 2-nm transistor by IBM (mentioned on the right).

Despite the progress made in technological controllability, there are many issues that become challenging and even limiting in this regime of dimensionality. Among them, it has been reported for decades by now that dopant-distribution fluctuations and discreteness of dopants in the nanoscale channels induce unacceptable variability of the threshold voltage (V_{th}),[5] one of the key parameters for the suitable and controllable on/off switching of a MOSFET. Although these issues are typically seen as problematic for MOSFETs further downscaled,[6] they also provide insights into electron transport controlled by discrete dopants, an idea that can provide

a completely new approach for future generations of electronics and is typically labeled as “dopant-based electronics”.[7]

This direction of research represents a part of the motivation for the study contained in this thesis, in which we focus on analyzing the role of clustered dopant-atoms (e.g., few-donor clusters), embedded in nanoscale Si channels, without and with counter-dopants (e.g., acceptors) located nearby. Such systems raise the level of complexity and versatility for developing new functionalities, on the background of the “dopant-based electronics”. Since this background is critical for understanding these more advanced systems, the progress achieved in “dopant-based electronics”, mostly over the past decade, will be overviewed in a subsequent section.

Below, a few different alternatives will be described that either circumvent the problem of dopant distribution or take even more advantage of such aspects.

1.1.2. Prospects for next-generation electronics

Different from the fundamental field of “dopant-based electronics”, there are other alternatives for the next generations of electronics, currently under consideration or under various stages of research.

One option is to remove completely the requirement for having junctions in the channel (following the standard designs of *npn* or *pnp* transistors, with *n* indicating a region doped with donors, such as phosphorus (P), and *p* indicating a region doped with acceptors, such as boron (B)). Such devices (junctionless transistors) can only be controlled to work as transistors, switching on/off current flow, if they have a sufficiently high level of doping while also maintaining very low dimensionality, in order

to allow depletion of carriers by a strongly-coupled gate. If the design conditions can be met and the device works indeed as an on/off switch, it is labeled as “junctionless transistor”.[8] There are an increasing number of reports on junctionless transistors, both on experiments taking advantage of the capabilities for lithography patterning into single-digit-nm range, and on simulations aiming at clarifying the transport mechanism and controlling parameters for further optimization. It can be understood, however, that these devices simply remove the need to consider carefully the *pn* junctions existing in the typical MOSFETs and possible dopant-fluctuation effects existing at these boundaries. On the other hand, they do not address the discreteness (or fluctuations) of the dopants present in the transistor channel, which may induce similar issues as for MOSFETs.

Another alternative is related to a solution for improving the limited subthreshold swing (SS) of a MOSFET, known to be 60 mV/decade due to the thermally-activated current being the main driving factor for device operation. If this mechanism can be replaced properly, this limit can be improved and higher switching speed can be expected. One way to do that is by implementing the band-to-band tunneling (BTBT) as a main transport mechanism in devices that fully take advantage of this kind of operation. BTBT has been initially reported in tunnel (Esaki) diodes,[9] which are highly-doped *pn* diodes (i.e., p^+-n^+ diodes). As an extension from these structures, p^+-*i*-n^+ diodes with a gate can allow for gate-control of the potential in the *i*-layer (similarly to the control of the channel of a MOSFET), while the on current can be driven by BTBT mechanism; these devices are known as “tunnel field-effect transistors (TFETs)” and have been demonstrated in a variety of semiconductors.[10] TFETs in Si, however, possess a significant challenge because of the indirect-bandgap nature of Si, which

requires momentum conservation for BTBT mechanism to occur with a sufficiently high rate.[11]

There have been reports indicating that low-dimensionality of Si (such as in nanofilms or nanowires) may relax the condition for momentum conservation because of quantum-confinement effects.[12] However, an even stronger effect may be expected from discrete, localized energy states present in such devices, possibly mediating BTBT transport. Since dopant atoms may induce such states, we consider such effects also as a motivation for another part of the work contained in this thesis, in which tunnel diodes in Si nanowires are studied specifically from the perspective of identifying the role of donors and acceptors (discrete dopants) on the BTBT mechanism. Since several effects of dopants in such Si tunnel diodes have been already reported in some of previous experimental works from our group[13-16] or others, these will be addressed in more detail in a subsequent section.

Finally, it should be mentioned that an alternative that also relies on the tunneling mechanism is the development of Si-based single-electron tunneling (SET) transistors.[17] Such devices contain nanoscale structures (Si islands or dopants with their potential wells), separated from source and drain leads by so-called tunnel barriers; under the framework of the Coulomb blockade theory,[18] electron transport can occur in such devices with electrons flowing one after another (single-electron tunneling). In principle, such devices can provide access to fundamental operation of future electronic devices at the level of elementary charges, with potential for low-power consumption functionalities.[19]

Different from all of the above, other research focuses on identifying different materials that can provide enhanced performance. Among these, III-V

semiconductors, graphene (and other 2D materials) or carbon nanotubes are main candidates, and research on these topics can provide complementary insights into the physics of ultimately downscaled electronic devices. However, since our broader objective is to analyze nanoscale devices based still on the main materials for electronics – silicon (Si) – but at an "atomic" (or "molecular") level, we focus in the following sections on describing more insights about the possible effects of dopants in Si nanoscale devices, such as nanoscale transistors and nanoscale diodes. In that sense, dopant-effects can be analyzed also from our experiments either focused on individual dopants[20] or clustered dopants[21] in Si nanodevices.

1.1.3. Dopant-atoms as transport paths

Dopants are conventionally used to change the conductivity of Si into *n*-type (by doping with donors, such as phosphorus (P)) or *p*-type (by doping with acceptors, such as boron (B)).[22] However, dopants are not only carrier providers for conduction, but they can be hosts for one extra electron (e.g., in the case of P-donors) or one extra hole (e.g., in the case of B-acceptors). Considering this, dopants can work as QDs, usually called "artificial atoms" (although, in this case, the QDs are actually formed by true atoms).

On the platform of "dopant-based electronics", there have been numerous reports on transport mediated by dopant-atoms in Si nano-transistor channels.[20,21,24,25] Typically, donors-atoms can either diffuse randomly from the leads' edges into the channel or be intentionally doped (randomly) into the channel and, thus, mediate transport between source and drain as stepping-stones. Various properties have been

analyzed, depending on the location of the dopants (in typical transistor channels, near the interface, at different depths etc.)[26-28] or depending on the dimensionality of the channel (in nano-films, in nanoscale channels or in specifically-patterned channels).[29,30] Typically, such devices are studied at low temperatures,[31] where single-electron tunneling (SET) via single dopants can be revealed.

In order to raise the SET operation temperature, for more practical applications, a main alternative is to use clusters of a few or several dopants. For instance, a cluster of donors can work as a quantum dot (QD) with enhanced barrier height, if the coupling among neighboring donors leads to a lowering (deepening) of the ground-state energy.[32,33] It was recently reported that such clustering, implemented into a nanoscale-transistor channel with a selective-doping technique, can allow the observation of SET operation at elevated temperatures (~150 K), and Coulomb blockade features can be observed even at room temperature (300 K).[34] This observation may be enhanced by counter-doping (doping with acceptors), which may increase the potential barriers, if (accidentally) located favorably. Considering such idea, one point of interest for this thesis is the analysis of interactions between donors and acceptors in ultra-small nanoscale channels, likely leading to enhanced functionalities.

Another impact of dopants can be observed in nanoscale *pn* diodes. It had been previously reported that the discreteness of dopants in the depletion-layer of low-dimensional *pn* diodes (in particular at low or moderate doping concentrations) can lead to detectable effects, such as random telegraph signals (RTS) or contribution to photon detection.[13,15] More recently, it was also shown that energy states induced by donors and acceptors can assist, under specific conditions, in band-to-band tunneling (BTBT), if doping concentrations are high enough.[16,35] As such, these results are

promising for illustrating the possibility of dopants (atoms or clusters), and in particular pairs of donors and acceptors, to play a key role in BTBT transport. In order to reveal more fundamental insights into the physics involved in such systems, a part of this work will be dedicated to a theoretical study of the impact of donor-acceptor pairs in nanoscale Si *pn* tunnel diodes.

1.1.4. Theoretical treatment approaches

In order to get access to fundamental information about the role of dopants in nanoscale devices, several theoretical approaches can be taken. There are several advantages and disadvantages that must be taken into consideration to choose among available options: (i) the accuracy of the physical modeling; (ii) the time consumption for simulations; (iii) the dimensions of the devices that can be studied; (iv) the implementation methodology and suitability of the treatment, among others. In general, conflicting factors exist, such as a dramatic increase in computational-time consumption when the dimensions of the simulated devices are increased significantly or when higher accuracy is desired. As such, an optimal combination of theoretical approaches must be considered.

Regarding theoretical treatment of Si nanostructures containing individual dopants or donor-acceptor pairs, there are by now a large set of reports, mainly dedicated to Si nanocrystals, using first-principles (*ab initio*) simulations. The main point of study is the improvement of the optoelectronic properties of the Si nanocrystals (absorption, photoluminescence) when co-doping is done with one donor and one acceptor.[36-39] On the other hand, there are only a limited number of *ab initio*

reports on Si nanowires, and mostly focusing on the role of single-type dopants on the electronic or optical properties.[40,41]

On this background, the cases of Si nanowires containing both types of dopants (donors and acceptors) in different configurations and different device structures remain largely unclarified. Therefore, this will become one of the main targets of this thesis. However, in order to access the transport characteristics, a semi-empirical approach is also included in the simulation. The details of the simulations, and the main methodologies, will be described in some detail in **Chapter 2**.

1.2. Purpose of this work

Considering the above background, the broad purpose of this thesis becomes *to study and provide new insights into the active role of dopant-atoms in tunneling transport*. However, this purpose can be split into two main sub-purposes:

(1) to identify the role of dopant-clusters in nanoscale Si transistors, in particular under the presence of counter-dopants (e.g., donor clusters in the presence of a few acceptors) – in other words, how important can be the role of counter-dopants in decoupling the donor cluster from the leads.[42]

(2) to understand the role of front-end dopants (donors near the *n*-lead and acceptors near the *p*-lead) in band-to-band tunneling (BTBT) through nanoscale *pn* diodes – in other words, how critical is coupling to the leads and coupling between the dopants in nanoscale depletion layers in BTBT transport.

An additional purpose, which remains largely for future work, is to generate a parallel between the main theoretical analyses and the results obtained from

experimental studies of Si nanodevices (here, silicon-on-insulator (SOI) nano-transistors and nano-diodes, as possible to fabricate with our capabilities). The objective of this thesis in that regard is to identify suitable examples that can tentatively illustrate the possibility of dopant effects in such nano-devices, and that can later be analyzed in more depth by a more direct correlation with our theoretical findings.

1.3. Outline of the thesis

The thesis is structured into six chapters, covering a number of topics that address the broader purpose described above and, more specifically, the key sub-purposes. A brief outline of each chapter is given below, to provide an overview of the thesis and additional insights for how the main objectives will be addressed.

Chapter 1 presents an introduction, rooted in the conventional Si-based electronics and its recent development towards single-digit-nm scales. It is indicated that Moore's law is reaching some hard walls, and alternative solutions have to be considered. The chapter presents a few such research ideas, including various device designs under consideration, but focuses more on the field of "dopant-based electronics". This field relies on the dopant-atoms (or clusters) as the active units of electronic devices, keeping still the Si-technology as main platform.

Chapter 2 describes the simulation methodology in details, based on the materials provided together with the main software utilized for this study. However, the key focus is on correlating the technical details with the requirements and specifications of the systems of interest in this thesis, i.e., dopant-atoms (donors and acceptors) in Si-nanowire devices (nano-transistors and nano-diodes). Details are

provided on how *ab initio* simulations (based on density functional theory) are combined with semi-empirical simulations to provide a broader picture of the systems under study (through analyses of density of states or current-voltage characteristics).

Chapter 3 presents mainly the simulation results dedicated to understanding electron transport through clusters of a few dopants (e.g., P-donors) in the presence of counter-dopants (e.g., B-acceptors), and vice versa, in nano-transistor structures. Various configurations are analyzed in parallel, mainly for *n*-type devices (that is, devices with *n*-type electrodes), but also for *p*-type devices, as references. The analysis combines insights from density of states (DOS) data and electrical characteristics.

Chapter 4 presents a more in-depth analysis of simulation results dedicated to understanding (mainly) the role of P-B pairs in BTBT transport in Si highly-doped *pn* diodes. The focus is on revealing the role of various configurations of P-B pairs on the BTBT transport, with a particular focus on understanding the importance of coupling to the leads versus inter-dopant coupling.

Chapter 5 presents a few selected experimental examples of measurements carried out on nanoscale silicon-on-insulator (SOI) devices, which exhibit features that can be associated (tentatively) with the theoretical analysis included in this thesis. Although the parallel analysis still needs to be strengthened, these data provide a bridge to consider for next device design and interpretation.

Chapter 6 presents conclusions based on the analysis carried out so far, and their implications, providing also several possible guidelines for future work that needs to be supplemented to this line of research in the future.

References

[1]J. E. Lilienfeld, Method and Apparatus for Controlling Electric Currents, US Patent 1745175

[2]D. Khang and M. Atalla: “Silicon-silicon dioxide field induced surface devices”, IRE Solid-State Device Res. Conf. Pittsburgh (1960).

[3]G. E. Moore, Electronics **38**, 114-117 (1965).

[4]IBM Newsroom, “IBM Unveils World's First 2 Nanometer Chip Technology, Opening a New Frontier for Semiconductors” (May 6th, 2021).

[5]A. Asenov, IEEE Trans. Electron Dev. **45**, 2502-2513 (1998).

[6]T. Shinada, S. Okamoto, T. Kobayashi, and I. Ohdomari, Nature **437**, 1128 (2005).

[7]*Single-Atom Nanoelectronics*, Eds. E. Prati and T. Shinada, Pan Stanford (2013).

[8]J. P. Colinge *et al.*, Nat. Nanotechnol. **5**, 225 (2010)

[9]L. Esaki, Y. Arakawa, and M. Kitamura, Nature **464**, 31 (2010) and references therein.

[10]A. C. Seabaugh and Q. Zhang, Proc. IEEE **98**, 2095 (2010).

[11]A. M. Ionescu and H. Riel, Nature **479**, 329 (2011) and references therein.

[12]S. Saito *et al*., Jpn. J. Appl. Phys. **45**, L679 (2006).

[13]S. Purwiyanti, R. Nowak, D. Moraru, T. Mizuno, D. Hartanto, R. Jablonski, and M. Tabe, Appl. Phys. Lett. **103**, 243102 (2013).

[14]R. Nowak, D. Moraru, T. Mizuno, R. Jablonski, and M. Tabe, Appl. Phys. Lett. **102**, 083109 (2013).

[15]A. Udhiarto, D. Moraru, S. Purwiyanti, Y. Kuzuya, T. Mizuno, H. Mizuta, and M. Tabe, Appl. Phys. Express **5**, 112201 (2012).

[16]M. Tabe, H.N. Tan, T. Mizuno, M. Muruganathan, L.T. Anh, H. Mizuta, R. Nuryadi, and D. Moraru, Appl. Phys. Lett. **108**, 093502 (2016).

[17]*Single Charge Tunneling*, ed. H. Grabert and M. H. Devoret, New York: Plenum (1992).

[18]D. V. Averin and K. K. Likharev, J. Low Temp. Phys. **62**, 345-373 (1986).

[19]K. K. Likharev, "Single-Electron Devices and Their Applications", Proc. IEEE **87**, 606-632 (1999).

[20]D. Moraru *et al*., Nanoscale Res. Lett. **6**, 479-1-9 (2011).

[21]D. Moraru *et al*., Nanoscale Res. Lett. **10**, 372 (2015) and references therein.

[22]S. M. Sze, Physics of Semiconductor Devices, 2nd Ed. (1981).

[23]P. M. Koenraad and M. E. Flatté, Nature Mater. **10**, 91 (2011).

[24]F. Zwanenburg, A. S. Dzurak, A. Morello, M. Y. Simmons, L.C. L. Hollenberg, G. Klimeck, S. Rogge, S. N. Coppersmith, M. A. Eriksson,, Rev. Mod. Phys. **85**, 961 (2013).

[25]H. Sellier, G. P. Lansbergen, J. Caro, S. Rogge, N. Collaert, I. Ferain, M. Jurczak and S. Biesemans, Phys. Rev. Lett. **97**, 206805 (2006).

[26]G. P. Lansbergen, R. Rahman, C. J. Wellard, I. Woo, J. Caro, N. Collaert, S. Biesemans, G. Klimeck, L. C. L. Hollenberg and S. Rogge, Nature Phys. **4**, 656 (2008).

[27]M. Pierre, R. Wacquez, X. Jehl, M. Sanquer, and O. Cueto, Nat. Nanotechnol. **5**, 133 (2010).

[28]M. Tabe, D. Moraru, M. Ligowski, M. Anwar, R. Jablonski, Y. Ono and T. Mizuno, Phys. Rev. Lett. **105**, 016803 (2010).

[29]E. Prati, M. Belli, S. Cocco, G. Petretto, and M. Fanciulli, Appl. Phys. Lett. **98**, 053109 (2011).

[30]M. Fuechsle, J. A. Miwa, S. Mahapatra, H. Ryu, S. Lee, O. Warschkow, L. C. L. Hollenberg, G. Klimeck and M. Y. Simmons, Nature Nanotechnol. **7**, 242 (2012).

[31]E. Hamid *et al*., Phys. Rev. B **87**, 085420 (2013).

[32]B. Weber, Y. H. M. Tan, S. Mahapatra, T. F. Watson, H. Ryu, R. Rahman, L. C. L. Hollenberg, G. Klimeck and M. Y. Simmons, Nature Nanotechnol. **9**, 430-435 (2014).

[33]M. F. Gonzalez-Zalba, A. Saraiva, M. J. Calderon, D. Heiss, B. Koiller and A. J. Ferguson, Nano Lett. **14**, 5672 (2014).

[34]A. Samanta, M. Muruganathan, M. Hori, Y. Ono, H. Mizuta, M. Tabe, and D. Moraru, Appl. Phys. Lett. **110**, 093107 (2017).

[35]G. Prabhudesai, M. Muruganathan, L. T. Anh, H. Mizuta, M. Hori, Y. Ono, M. Tabe, and D. Moraru, Appl. Phys. Lett. **114**, 243502 (2019).

[36]F. Iori *et al*., Phys. Rev. B **76**, 085302 (2007).

[37]I. Marri, E. Degoli and S. Ossicini, Prog. Surf. Sci. **92**, 375 (2017) and references therein

[38]Y. Ma, X. Chen, X. Pi and D. Yang, J. Nanopart. Res. **14**, 802 (2012) and references therein.

[39]R. Rurali, Rev. Mod. Phys. **82**, 427 (2010).

[40]T. Markussen, R. Rurali, A.-P. Jauho and M. Brandbyge, Phys. Rev. Lett. **99**, 076803 (2007).

[41]M. Bescond, M. Lannoo, L. Raymond and F. Michelini, J. Appl. Phys. **107**, 093703 (2010).

[42]Chitra Pandy, G. Prabhudesai, K. Yamaguchi, V N Ramakrishnan, Y. Neo, H. Mimura, and D. Moraru, Appl. Phys. Express **14**, 055002 (2021).

Chapter 2: Simulation methodology for analysis of Si nano-devices

2.1. Basics of first-principles simulations

Atomic-scale modeling has increasing importance for academic research and development in a wide range of technological domains, including semiconductors. Numerical simulations provide greater insights by calculating the electronic and transport properties of various systems of interest. This kind of modeling starts from quantum-chemical calculations, solving many-body Schrödinger equations to empirical force-field methods, including millions of atoms. Due to time and computational-resource constraints, these methods can be broadly described as either computationally more or less accurate. However, an alternative methodology is the density functional theory (DFT), which can deliver approximate and computationally feasible solutions to electronic many-body problems. These methods provide the feasible solutions with relatively reduced computational requirements and better accuracy, eventually offering more consistency with experiments. In this framework, *ab initio* (first-principles) calculations can be performed for electronic structure of semiconductor materials and devices, and their applications.

Modeling nanoscale devices, mainly by electron-transport simulations, also relies on the Non-Equilibrium Green's Function (NEGF) formalism[1]. This method consists of two main steps. First, the electronic structure of the system is calculated using *ab initio* calculation from first principles, mainly utilizing density-functional theory (DFT)[2-5]. Second, by semi-empirical methods, calculating electronic structures using analytical models with adaptable parameters (fitting to experiments) allows even the evaluation of current (and transmission) through the structure of interest.

Semiempirical methods are most commonly based on Slater-Koster tight binding[6,7] or Extended Hückel (EH)[8] methods.

The *ab initio* models are more accurate and give reasonable solutions, but they are also more computationally demanding, while semi-empirical models are less accurate, but provide sufficiently accurate results and some insights into practical, application-oriented aspects, with lower computational time.

In this chapter, the theory and methods used in the analysis presented in subsequent chapters will be described in more detail; as a key monitoring approach of the output, this study takes advantage of the Non-Equilibrium Greens Function (NEGF) method for the calculation of transmission coefficients and currents through a variety of Si nanostructures.

2.1.1. Density Functional Theory (DFT)

The modeling of the electronic properties of quantum systems, within the framework of the density functional theory simulations, are divided into the two main types: (i) DFT:LCAO (Linear Combination of Atomic Orbitals basis set)[9] and DFT:PlaneWave[10]. For open systems (as well as closed systems), QuantumATK (the software used mainly in this work) typically uses the DFT:LCAO calculator. The DFT:Plane Wave calculator is not suitable for open systems, basically because it assumes periodic-boundary conditions when solving the Kohn–Sham equations. At first, these Kohn-Sham equations are solved self-consistently in order to determine the electron-density matrix. For open systems, this is calculated using the NEGF method, while for closed and periodic systems it is calculated by diagonalization of the

Kohn-Sham Hamiltonian. The procedure to obtain the Kohn-Sham Hamiltonian is to first start with a specific electron density, then set up an effective potential (which is given by the Hartree, exchange-correlation, and external potentials). Knowing the effective potential allows us to obtain the Kohn–Sham Hamiltonian.

The Kohn–Sham Hamiltonian can be calculated according to the system of choice, as mentioned above, but varies mainly by the selection of pseudo potentials. DFT:LCAO uses DFT and norm-conserving pseudopotentials, while DFT:PlaneWave uses DFT in combination with norm-conserving pseudopotentials or PAW potentials[10,11]. More details about each approach will be described next.

DFT: LCAO

The main parameter in the self-consistent calculation of the Kohn-Sham equations is the density matrix, which defines the electron density. This is based on the expansion of the single-particle wave functions, based on numerical atomic orbitals.

In DFT, the many-body electronic structure of the system is described by the one-electron Kohn-Sham Hamiltonian:

$$\widehat{H}_{1el} = -\frac{\hbar^2}{2m}\nabla^2 + v^{eff}[n](r) \qquad (1)$$

The first term on the right in Eq. (1) corresponds to the kinetic energy of the electrons, and the second term is the effective potential. The above equation is solved by the expansion of the basis set provided.

One-electron eigenfunctions of the Kohn-Sham Hamiltonian are solved by the one-electron Schrödinger equation:

$$\widehat{H}_{1el}\psi_\alpha(r) = \varepsilon_\alpha\psi_\alpha(r) \qquad (2)$$

This Equation (2) is solved by expanding the eigenfunctions $\psi_\alpha(r)$ in a set of basis functions φ_i. This differential equation is represented into a matrix by expanding into the Hamiltonian matrix and overlap matrix, with respect to the electron coordinates. The Electron Density of the many-electron system is then defined by the occupied eigenstates of the Kohn-Sham Hamiltonian, and, for finite temperatures, these occupations are typically calculated based on the Fermi-Dirac distribution.

The electron density can then be expressed in terms of the density matrix:

$$n(r) = \sum_{ij} D_{ij}\phi_i(r)\phi_j(r) \qquad (3)$$

where the density matrix is given by the basis set expansion coefficients $\mathbf{C}_{\alpha i}$

$$D_{ij} = \sum_{\alpha} f_\alpha C^*_{\alpha i} C_{\alpha j} \qquad (4)$$

where

$$f_\alpha = \frac{1}{1+e^{\frac{(\varepsilon_\alpha - \varepsilon_F)}{kT}}} \qquad (5)$$

Next, the effective potential $V^{eff}[n]$ calculation is explained below. This potential comprises of three components: (1) the Hartree Potential, due to the mean-field electrostatic interaction between electrons; (2) the Exchange-Correlation potential, arising from the quantum-mechanical nature of the electrons; (3) the external potential, representing other electrostatic fields, either induced by the electrostatic potentials of the ions or by the external electrostatic fields (like external sources).

$$V^{eff}(n) = V^{H}(n) + V^{XC}(n) + V^{ext} \qquad (6)$$

First two potentials in Eq. (6) ($V^{H}[n]$, $V^{XC}[n]$) are due to the electron-electron interactions. The external potential (V^{ext}) is induced by the pseudopotentials and external field, as created by the introduction of metallic gates.

The Hartree potentials ($V^{H}[n]$) are calculated from the electrostatic potentials considering the electron-charge density and Poisson equation.

$$\nabla^2 V_H[n](r) = -4\Pi n(r) \qquad (7)$$

The exchange-correlation potential ($V^{XC}[n]$) is defined as the functional derivative of the exchange-correlation energy as a function of the electron density, corresponding to a mean-field quantum-mechanical interaction potential between the electrons in the system:

$$V^{XC}[n](r) = \frac{\delta E^{XC}}{\delta n}(r) \qquad (8)$$

Like different potentials, the total energy (E(n)) of a many-electron system is also calculated by using the electron density, with the use of Hartree potential energy ($E^{H}[n]$), exchange correlation energy ($E^{XC}[n]$) and other external-sources energy ($E^{ext}[n]$). The total energy of the system is thus given by:

$$E(n) = T(n) + E^{XC}(n) + E^{ext}(n) \qquad (9)$$

Here, T[n] is the kinetic energy of a non-interacting electron gas of density (n).

$$T(n) = \sum_{\alpha} f_{\alpha} \left\langle \psi_{\alpha} \left| \frac{-\hbar^2}{2m} \nabla^2 \right| \psi_{\alpha} \right\rangle \qquad (10)$$

The Force can be calculated by differentiating the total energy with respect to the ion coordinates of atom *i*, at position R_i.

$$F_i = -\frac{dE(n)}{dR_i} \qquad (11)$$

For all the above calculations, Pseudopotentials and PAW potentials are defined in the Quantum ATK and can be chosen according to the user requirements. The main basis set used in the DFT: LCAO is the so-called LCAO basis set (Linear Combination of Atomic Orbitals). These set parameters determine the shape of the orbitals. The exchange correlation energy is mainly classified into: Local Density Approximation (LDA), Generalized Gradient Approximation (GGA) and Meta-GGA with four spin variants: (i) non-polarized; (ii) spin-polarized; (iii) non-collinear; (iv) non-collinear with spin-orbit coupling. The choice of spin variant for the exchange correlation functional determines the spin type used in all the DFT-LCAO calculations. Other than this aspect, correction methods, like Hubbard correction, XC+U mean field Hubbard, DFT-1/2 method, DFT-D2, DFT-D3 can be added to all exchange correlation variants. These correction methods are not utilized in our calculation, which mainly uses this approach for the structural-relaxation (geometry optimization) part of the calculations. The self-energy potential is included in the calculation of the total energy, forces, and stress, mainly for calculating the band structures, not for such structural optimizations.

DFT: Plane Wave

The modeling of the electronic-properties of quantum systems, within the framework of density functional theory for periodic systems, follows the DFT: Planewave. As mentioned before, the DFT: Planewave Wave calculator is not suitable

for open systems due to the periodic boundary conditions that must be assumed when solving the Kohn–Sham equations. Kohn-Sham equation is solved for the electron density matrix, which is self-consistently obtained. This is calculated, for closed and periodic systems, by the diagonalization of the Kohn-Sham Hamiltonian.

All the methodologies explained in the DFT: LCAO section are generally applicable for the DFT: Planewave, with different basis set and pseudopotentials. This method is based on an expansion of the single-particle wave functions in a basis of plane-wave functions to solve the Kohn-Sham equations, instead of the LCAO basis set. The Planewave calculators calculate the electronic structure of the system using DFT with norm-conserving pseudopotentials or PAW potentials. This calculator does not support the XC+U mean field Hubbard term and DFT-1/2 methods for corrections.

2.1.2. Extensions from Density Functional Theory (DFT)

In order to understand the DFT method in our work and to obtain the fundamental results for closed systems, simulations are focused on small nanostructures like Silicon Nanocrystals (SNCs) or Nanorods. The main aim of this study is to provide a fundamental theoretical base for understanding the impact of **atomistic (co)-doping** on the electronic properties of nanostructures (nano-channels).

The aim of the *ab initio* calculations is to obtain fundamental properties of materials from simulations, without using any approximations dependent on the experimental data. In our subsequent simulations, all calculations are performed using the density-functional theory (DFT) within the local density approximation (LDA) for the exchange-correlation functional. The present results have been obtained using Generalized Gradient Approximation (GGA) exchange correlation method. A kinetic

energy cut-off of 80 Hartree was used for the undoped, P-doped, B-doped and co-doped Si nanostructures. It should be noted, however, that due to computational-resource limitations, only very small structures can be investigated at present.

Si nanostructures are prepared with the [100] orientation along the Z direction, with radius of 7.5 Å. The Si nanostructures are covered with H atoms in order to passivate the dangling bonds. Thus, nanostructures investigated in this work are effectively $Si_{52}H_{30}$ clusters. In order to investigate the effects of individual dopants and in particular the interaction of opposite-type dopants, different doping configurations are prepared, such as single-dopant doped nanostructures, multiple-dopant doped nanostructures and co-doped nanostructures. A complete geometric optimization is done after the dopants are added. **Figures 2.1(a)-(d)** show these undoped, Single-P doped, Single-B doped, and P-B co-doped atomistic structures in zoom-in views.

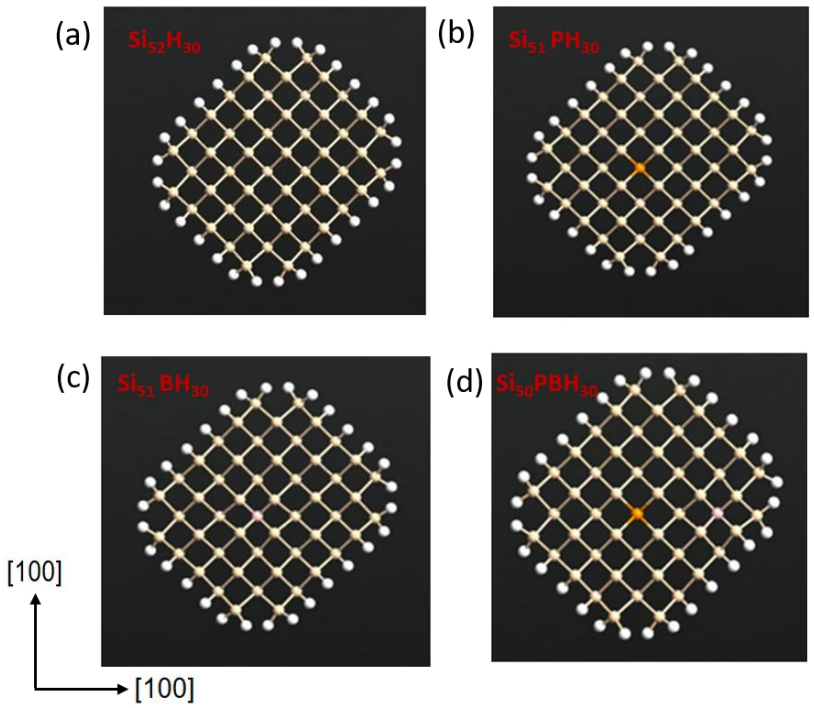

Fig. 2.1 $Si_{52}H_{30}$ nanostructures used in the fundamental study of Si nanocrystals, shown by the atomistic view for structures that are: (a) undoped; (b) Single-P doped; (c) Single-B doped and (d) P-B co-doped.

Figure 2.2 shows the comparative results of the study of the density of states (DOS) spectra for these different nanostructures. Effects of opposite-type dopants can be seen as shifts of the Fermi level, E_F, towards the corresponding band edge (conduction band for P-doping and valence band for B-doping), as seen when comparing the undoped-case [**Fig. 2.2(a)**] with P-doped [**(b)**] or B-doped [**(c)**] cases.

The emergence of localized states in the bandgap region is ascribed to energy states due to the presence of B and P dopants. As seen in **Fig. 2.2(d)**, co-doping (with one P-donor and one B-acceptor) induces also a compensation effect, that can be seen by the fact that Fermi level remains near the midgap. As the number of dopants is unbalanced, the shift is consequently increased in one direction or another, which reveals the impact of increasing doping concentration on the electronic properties.

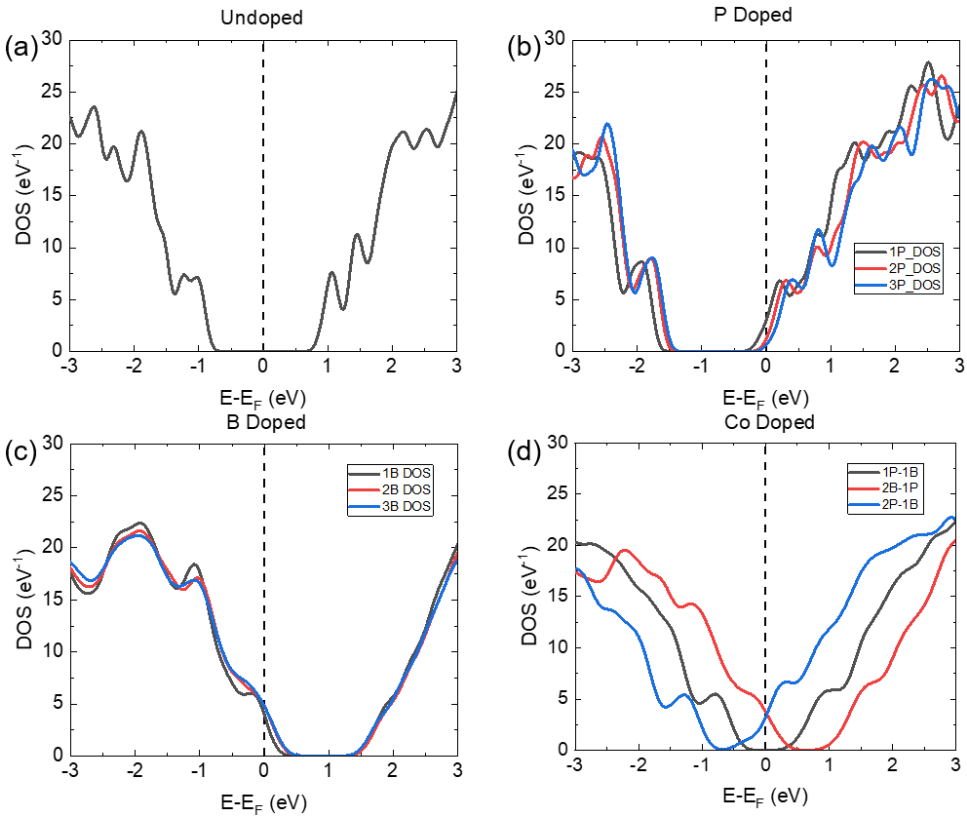

Fig. 2.2 Density of States (DOS) spectra for Si nanostructures that are: (a) Undoped; (b) P-doped; (c) B-doped and (d) Co-doped. On the horizontal axis, E=0 eV corresponds to the Fermi level, E_F (guides are drawn as dashed lines).

An analysis of the molecular energy spectrum and wave function distributions can provide further insights into the electron localization around different dopants. Molecular energy spectra (MES) of different configurations are considered for this study, as shown in **Fig. 2.3**, focusing on the lowest unoccupied molecular orbital (LUMO) and highest occupied molecular orbital (HOMO) levels. It should also be noted that it is expected that the Bohr radius (r_B) for such very small nanostructures is significantly different (lower) from the bulk case.

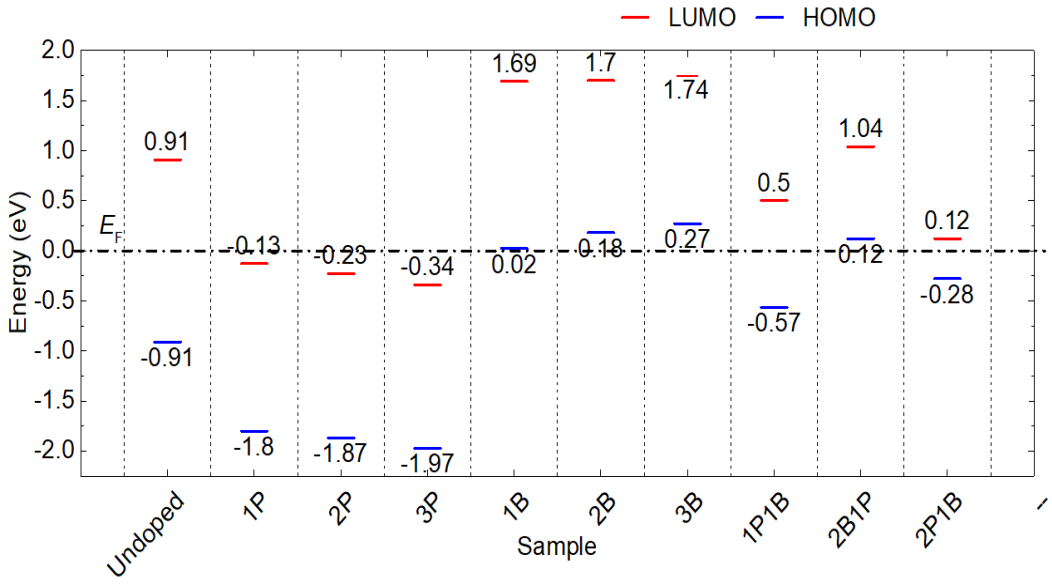

Fig. 2.3 Molecular Energy Spectra of different cases under study. Only the lowest unoccupied molecular orbital (LUMO) and highest occupied molecular orbital (HOMO) are shown. Fermi level is adjusted to 0 eV for all cases.

This initial study provides the foundation for interpreting the roles of individual dopants or dopant pairs (donor-acceptor pairs) on the electronic properties of Si nanostructures. It has been clearly shown that, even in such ultra-small structures, a P-donor and, respectively, a B-acceptor (or multiple dopants) work to shift the Fermi level closer to the conduction band edge or, respectively, to the valence band edge. Furthermore, it was shown that co-doping maintains the Fermi level near midgap, i.e.,

compensation can be considered to occur and the system can be treated basically as an intrinsic (undoped) nanocrystal.

Although this study can be further expanded in order to reveal more insights into the properties of such Si nanocrystals, the main target of this work is to address the transport properties and not the static properties of systems isolated from the external environment. As such, transport properties are the main point of focus and transmission needs to be studied by attaching leads to such nanostructures. This methodology will be described in more detail in the next section.

2.2. Basics of semi-empirical simulation approach

A computationally fast alternative to DFT is the ATK-SE (semi-empirical) engine (embedded in QuantumATK) that allows for semi-empirical tight binding (TB) type of simulations.[12,13] The TB models consist of a non-self-consistent Hamiltonian that can be extended with a self-consistent correction for charge fluctuations and spin polarization. These corrections closely follow the density functional tight-binding (DFTB) approach.[14]

The main advantage of the SE models compared to DFT methods are their computational efficiency. For large systems, the main computational cost of both DFT and TB simulations is related to the diagonalization of the Hamiltonian; this strongly depends on the number of orbitals assigned on each site and their range. This makes TB Hamiltonians attractive for large systems, as long as the SE parametrization is appropriate for the particular simulation. Furthermore, orthogonal Hamiltonians have inherent performance advantages. In Semi-Empirical (SE) package, the non-self-

consistent part of the tight-binding Hamiltonian is parametrized using a two-center approximation, i.e., the matrix elements only depend on the distance between two atoms and are independent on the position of the other atoms. In the extended Hückel model, the matrix elements are described in terms of overlaps between Slater orbitals on each site. In this way, the matrix elements can be defined by very few parameters.

In the Slater–Koster model, the distance-dependence of the matrix elements is given as a numerical function. This approach provides higher flexibility, but also makes the fitting procedure more difficult. The self-consistent part of the calculation is identical for both SE models. The density matrix is then calculated from the Hamiltonian using the non-equilibrium Green's function (NEGF) for device systems, while for molecules and crystals it is calculated by diagonalization. The density matrix defines the real-space electron density and, consequently, the Hartree potential can be obtained by solving the Poisson equation.

2.3. Transport Calculation in the two-probe system

The advantage of Quantum-transport analysis is that it can be utilized to achieve highest accuracy and performance for both bulk and device systems. The two-probe device geometry is implemented by defining a structure with a left electrode, a central region and a right electrode. The three regions have the same boundary conditions (Neumann boundary conditions) in the two lateral directions perpendicular to the left-right electron transport direction.

Assuming that the left and right electrodes are bulk, the first step of device simulation is to perform the bulk calculation for each electrode with periodic boundary

conditions in the transport directions. Using Bloch's theorem, wave functions are defined by transverse k-points which connect all the regions and same k-point sampling is used in the transverse directions for the three regions calculation. The proper periodic boundary conditions need to be defined for all the regions. The central region of the device has the wave functions described by using scattering boundary conditions, while for electrodes, by using periodic boundary conditions. A very dense electrode *k*-point grid is needed in the transport directions. Electrodes are modeled in their ground states with their chemical potentials μ_L and μ_R. The electrostatic potential of the central region should be sufficiently screened. The convergence is possible by the introduction of electrode extension regions, with the potential of this region being almost in coincidence with the electrode.

For the device simulation, all the regions must be properly aligned to common reference which is achieved by applying a potential shift to the electronic structure of the right electrode with the condition that,

$$\mu_L - \mu_R = -eV_{bias}$$

where V_{bias} is the applied bias on the electrodes. At zero bias, $\mu_L = \mu_R$. Thus, the electrostatic potentials of all the regions aligned to the common reference, while the device built-in potentials are properly included.

The calculation of the electron distribution in the central regions is very important, and it can be done in two different ways: (1) as non-equilibrium electron distribution; (2) by the Non-Equilibrium Green's Function (NEGF) approach.

2.3.1. Non-equilibrium electron distribution

In this method, electron density can be calculated by using the scattering states. In this approach, the left and right electrodes are considered in equilibrium, with periodic boundary conditions. Assuming that the system is in a steady state, and that the electron density of the central region is constant in time, the chemical potential of the two electrodes are different, and the contribution of each electrode is calculated by the occupied eigenstates of the system. The total electron density is the summation of scattering states from left and right electrodes:

$$n^L(r) = \sum_{\alpha} |\psi_\alpha(r)|^2 f\left(\frac{\varepsilon_\alpha - \mu_L}{kT}\right) \qquad (12)$$

$$n^R(r) = \sum_{\alpha} |\psi_\alpha(r)|^2 f\left(\frac{\varepsilon_\alpha - \mu_R}{kT}\right) \qquad (13)$$

The scattering states are calculated by the Bloch states in the electrode and by solving the Schrödinger equation of the central region, using those states with proper boundary conditions.

2.3.2. Non-Equilibrium Green's Function (NEGF) approach

Alternative method is to calculate the non-equilibrium electron density by the Non-Equilibrium Green's Function approach instead of using the scattering states[15]. In this method, the electron density is represented in terms of density matrix as left and right contributions:

$$D = D^L + D^R$$

Density matrix contribution is calculated using the spectral density matrix, while there is a non-equilibrium electron distribution in the central region; the distribution is described by Fermi function (f) with an electron temperature T_L. Spectral density is a function of broadening function of electrodes (ΓL, ΓR) which is given in terms self-energy (Σ^L, Σ^R). Expressions below are given as example for the left electrode:

$$D^L = \int \rho^L(\varepsilon) f\left(\frac{\varepsilon-\mu_L}{k_B T_L}\right) d\varepsilon \quad (14)$$

$$\rho^L(\varepsilon) = \frac{1}{2\pi} G(\varepsilon) \Gamma^L(\varepsilon) G^\dagger(\varepsilon) \quad (15)$$

$$\Gamma^L = \frac{1}{i}\left(\Sigma^L - (\Sigma^L)^\dagger\right) \quad (16)$$

The NEGF method allows the calculation of the retarded Green's function matrix for the central region, which is critical for further calculations. This is calculated from the central-region Hamiltonian matrix H and the overlap matrix S, by adding the electrode self-energies:

$$G(\varepsilon) = [(\varepsilon + i\delta_+)S - H - \Sigma^L(\varepsilon) - \Sigma^R(\varepsilon)]^{-1} \quad (17)$$

where δ_+ is an infinitesimal positive number.

Next, a few other important parameters to be considered, in order for this calculation to be stable and converged in the NEGF device algorithm, are explained in this section. The self-energy describes the effect of the electrode states on the electronic structure of the central region. Self-Energy calculation are covered by four different methods: (i) direct; (ii) recursion; (iii) Sparse Recursion; (iv) Krylov. Each has its own advantage and usage according to the system size and computational complexity. The energy integral evaluation is through a complex contour integration including two different parts: integral over equilibrium states and non-equilibrium

states[16]. Two different contour methods are utilized: (i) SingleContour for small bias and fast method; (ii) DoubleContour for high bias and stable method.

2.3.3. Effective Potential

After the calculation of the Non-equilibrium electron density, the next step is to calculate the effective potential. Potential calculation is same as described in the DFT:LCAO section. Mainly, the Hartree potential of the central region is obtained by solving the Poisson equation using appropriate boundary conditions at the interface between the electrodes and the central region. Here, five different methods are available: (i) Fast-Fourier 2D Solver; (ii) Multigrid Solver; (iii) Direct Solver; (iv) Parallel Conjugate Gradient Solver and (v) Fast-Fourier Solver. The default is FastFourier2DSolver option, because it is a fast and accurate method.

For the metallic gates and dielectric spacers, different types of boundary conditions are needed, and MultigridSolver option is preferred.

2.3.4. Transmission coefficient and electrical current

When the self-consistent non-equilibrium density matrix has been obtained, it is possible to calculate various transport properties of the system. One of the most important aspects to monitor is the transmission spectrum; this is also used to calculate the current and differential conductance. The transmission coefficient T (effectively, a measure of transmission probability) at electron energy ε is obtained from the retarded Green's function:

$$T(\varepsilon) = Tr[G(\varepsilon)\Gamma^{L}(\varepsilon)G^{\dagger}(\Sigma)\Gamma^{R}(\varepsilon)] \quad (18)$$

The electrical current is given by the Landauer formula:[17]

$$I = \frac{2e}{h_-} \int_{\infty}^{\infty} d\varepsilon\, T(\varepsilon) \left[f\left(\frac{\varepsilon - \mu_L}{k_B T_L}\right) - f\left(\frac{\varepsilon - \mu_R}{k_B T_R}\right) \right] \quad (19)$$

The DFT method can consider the many-body interaction effects, while the NEGF method can treat the non-equilibrium effects and the non-periodic boundary conditions. The combination of the DFT and the NEGF methods, therefore, allows us to calculate electronic transport properties of open systems more accurately and comprehensively. In this research, all first-principles calculations were performed using the software QuantumATK (by Synopsis), which is implemented on both the DFT and the NEGF methods. In particular, the first-principles calculations were performed using mainly the density functional theories, in particular DFT:LCAO method, and mainly for “bulk” structure (geometry) optimization. For this, all calculations are performed by using generalized gradient approximation (GGA) PBE version of the exchange-correlation potential.[18,19] The convergence threshold for the self-consistent field (SCF) iteration has a mesh density cut-off of 80 Hartree. For numerical accuracy, the Fermi-Dirac occupation method is used.

For the Si nanowire, we use the conventional diagonalization solver method for Eigen solver in the SCF iterations. For the Si nanowire device (two-probe system) with doped-electrode regions, we use the non-equilibrium Green’s function (NEGF) method which is implemented within the QuantumATK.[17] The NEGF method enables us to calculate the Current-Voltage (*I*-*V*) characteristics of the different configurations investigated in this study.

2.4. Density of states and different occurrences

The properties of the system under study can be understood by using various analysis methods. Here, in our work, a main focus falls on the density of states (DOS) spectra. In QuantumATK package, various density spectrum analysis methods are available, such as, for example, (general or total) Density of States (DOS), Local Density of States (LDOS), Device Density of States (DDOS), Projected Local Density of States (PLDOS). In our analysis, we mainly focus on the Local Density of States (LDOS) spectrum, because it provides most revealing insights into the properties of the system locally modified by the presence of discrete dopants.

The density of states in device is spatially invariant, and it defines the proportion of states that are to be occupied as a function of the system energy. Mathematically, DOS is defined as the probability density function that an average of the various states are occupied in the system and it is continuous in nature. In the atomistically-defined devices, due to the quantum nature of such small structures, the DOS spectrum can be solved in Space, which is called Local Density of States and is discrete in nature. To make a correlation with microscopy experimental techniques, this is sometimes described as imaging electron densities with atomic resolution, like employing Scanning Tunneling Microscope (STM). LDOS spectra provide information also about the clear boundary between the electrodes and central region, corresponding to more insights for the analysis of the band edges.

LDOS spectra are calculated by specifying a few parameters first, such as: (i) the range of energy in which the LDOS is calculated; (ii) band indices which will contribute to the partial electron density calculation (by default, all bands are included); (iii) *k*-points used to calculate the partial electron density from the eigenstates at

specified *k*-points; (iv) the method to support the integration of DOS (including the Gaussian Broadening parameters). In our calculation, LDOS spectra for the device structure are computed using the spectral density matrix, within the NEGF method, as explained briefly in Section 2.3.2.

where $\Phi_{i,j}(r)$ are basis set orbitals and ρ(E) is a summation of left and right electrode in the spectral density matrix.

$$D(E,r) = \sum_{ij} \rho_{ij}(E)\phi_i(r)\phi_j(r) \quad (20)$$

Based on the procedures and methodologies described in this chapter, the subsequent chapters will present the results of the simulations for two main device structures of interest: (1) Si nano-transistors containing discrete dopants (in particular, focusing on the role of few-dopant "clusters" in the presence of counter-dopants); (ii) Si nano-diodes containing co-dopants, i.e., both P-donors and B-acceptors (in particular, focusing on the impact of a donor-acceptor pair in band-to-band tunneling transport). Since the basic methodology has been described in detail in this chapter (and is available for further information on the QuantumATK support materials), the description of the approaches and methodologies in the subsequent chapters will be only briefly mentioned, and only specific parameters, relevant to the respective calculations, will be described.

It should also be mentioned that the calculation capabilities are dependent on the computational resources and software upgrades. Although currently there are limitations in terms of dimensionality of the structures that can be simulated, it can be expected that such limitations become less and less critical in the upcoming period.

References

[1]H. Haug and A. P. Jauho, “Quantum Kinetics in Transport and Optics of Semiconductors” (Berlin: Springer, 2009).

[2]N. D. Lang, Phys. Rev. B **52**, 5335 (1995).

[3]Y. Xue, Chem. Phys. **281**, 151 (2002).

[4]M. Brandbyge, J.-L. Mozos, P. Ordejón, J. Taylor, and K. Stokbro, Phys. Rev. B **65**, 165401 (2002).

[5]J. Taylor, H. Guo, and J. Wang, Phys. Rev. B **63**, 245407 (2001).

[6]J. M. Jancu, R. Scholz, F. Beltram and F. Bassani, Phys. Rev. B **57**, 6493 (1998).

[7]M. Elstner, D. Porezag, G. Jungnickel, J. Elsner, M. Haugk, Th. Frauenheim, S. Suhai, and G. Seifert, Phys. Rev. B **58**,7260 (1998).

[8]K. Stokbro, D. E. Petersen, S. Smidstrup, A. Blom, M. Ipsen and K. Kaasbjerg, Phys. Rev. B **82**, 075420 (2010).

[9]J. M. Soler, E. Artacho, J. D. Gale, A. García, J. Junquera, P. Ordejón, and D. Sánchez-Portal, J. Phys.: Condensed Matter **14**, 2745 (2002).

[10]S. Smidstrup, T. Markussen, P. Vancraeyveld, P. Wellendorffi, J. Schneider, T. Gunst, B. Verstichel, D. Stradi, P. A. Khomyakov, U. G. Vej-Hanseni, M.-E. Lee, S. T. Chill, F. Rasmussen, G. Penazzi, F. Corsetti, A. Ojanperä, K. Jensen, M. L. N. Palsgaard, U. Martinez, A. Blom, M. Brandbyge, and K. Stokbro, “QuantumATK: an integrated platform of electronic and atomic-scale modelling tools”, Journal of Physics: Condensed Matter **32**, 015901 (2019).

[11]P. E. Blöchl, Phys. Rev. B **50**,17953 (1994).

[12]P. Vogl, H. P. Hjalmarson and J. D. Dow, J. Phys. Chem. Solids **44**, 365 (1983).

[13]J. M. Jancu, R. Scholz, F. Beltram and F. Bassani, Phys. Rev. B **57**, 6493 (1998).

[14]M. Elstner, D. Porezag, G. Jungnickel, J. Elsner, M. Haugk, T. Frauenheim, S. Suhai and G. Seifert, Phys. Rev. B **58**, 7260 (1998).

[15]M. Brandbyge, J. L. Mozos, P. Ordejón, J. Taylor and K. Stokbro, Phys. Rev. B **65,** 165401 (2002).

[16]T. Ozaki, K. Nishio, and H. Kino, Phys. Rev. B **81**, 035116 (2010).

[17]D. Stradi, U. Martinez, A. Blom, M. Brandbyge, and K. Stokbro, Phys. Rev. B **93**,155302 (2016).

[18]M. Schlipf and F. Gygi, Comp. Phys. Comm. **196**, 36 (2015).

[19]M. J. van Setten, M. Giantomassi, E. Bousquet, M. J. Verstraete, D. R. Hamann, X. Gonze and G. M. Rignanese, Comp. Phys. Comm. **226**, 226 (2018).

Chapter 3: Electron transport through a few-dopant clusters in the presence of counter-dopants in transistors

3.1. Basic approach for analysis of the co-doped nano-transistors

In the past few decades, an increasing number of scientific papers reported transport mediated by dopant-induced QDs, even achieved by single-electron tunneling (SET) based on the Coulomb blockade effect. In most of these reports, however, conventional doping was used for device fabrication, so that the position and number of dopants were not well controlled parameters. Moreover, most of these reports are limited to low temperature (<100 K) because at higher temperature thermal activation of carriers over the tunnel barriers is equivalent to ionization of dopants (with an ionization energy of just several tens of meV).[1,2] More recently, it was shown that "clustering" of a few phosphorus (P) donors can lead to the formation of deeper QDs.[3-5] SET transport can be observed in such cases even at elevated temperatures (~150 K), and some modulation of the current remains observable even at room temperature (300 K).[6] "Clustering" refers here to coupling of two or more P-donors located near each other (within a distance comparable to or smaller than Bohr radius, $r_B \approx 2.5$ nm in bulk Si), with the condition that the P-donors are still separated by one or more Si atoms. Such a "cluster" typically has enhanced tunnel barriers (as a result of the ground-state energy level of the resultant QD becoming deeper than for single-donor QDs). In a previous report, formation of such a "cluster" was partly controlled by a nanoscale selective-doping technique in a silicon-on-insulator (SOI) nano-transistor.[5,6] As a more precise and controllable option, albeit based on a more sophisticated technology, a few-donor "cluster" can also be formed by the scanning tunneling microscope (STM) atomic manipulation of dopants.[7,8,9]

Because such few-donor “clusters” provide important opportunities for new device functionalities, one of the objectives of this work is to reveal their properties in more depth. First-principles (*ab initio*) simulations can be used to provide significant insights and a large number of studies of dopant atoms inside Si nanostructures have already been reported. First-principles simulations have so far been used to analyze Si nanocrystals[10-12] or Si nanowires.[13-15] In such reports, a significant progress has been made in understanding the role of passivation, crystalline orientation, and doping (typically with one type of dopant or another). However, co-doping in Si nanostructures (which means doping of both donors and acceptors in the same nanostructure) could allow tuning of the transport properties of the above nanostructures, but so far such studies mainly focused on revealing mechanisms for enhancing photoluminescence or optical absorption. We suggest in this work that co-doping of Si nanowires with donors and acceptors can also provide enhanced tunability of electron-transport properties. This kind of study can also support, as a fundamental base, new research on realizing SET transport at elevated temperatures.

In this work, we specifically address the basic effects of counter-doping, in particular the role of specific locations and configurations, and analyze electron transport through a few-donor “cluster” embedded in the channel of Si-nanowire transistors, in the presence of boron (B) acceptor-atoms. This analysis is based on first principles and semi-empirical simulations, as explained briefly in this chapter.

For this study, a gate-all-around Si-nanowire transistor is first built using Quantum ATK software, designed as a basic structure to have a <100> orientation along the transport direction (labeled as Z in this study), a central-region length of 5.43 nm and a cross-sectional diameter (dimension) of about 1 nm. The atomistic structure of such a Si nanowire is shown in **Fig. 3.1(a)**, with **Fig. 3.1(b)** showing the cross-

section view of the gated nanowire. This structure is optimized using an in-built optimizer[16] with maximum forces of 0.05 eV/Å. All dangling bonds are passivated by H atoms. A device (transistor) is generated from this structure in the second step. For that, n^+-type source and drain regions of lengths of 1.086 nm, electrostatically doped at a concentration $N_D = 2\times10^{20}$ cm^{-3}, are generated, while discrete P-donors (and B-acceptors) are added substitutionally in the channel. The gated transistor structure is generated at the end by placing a metal gate around the channel (in a gate-all-around design), separated from the channel by a thin vacuum layer.

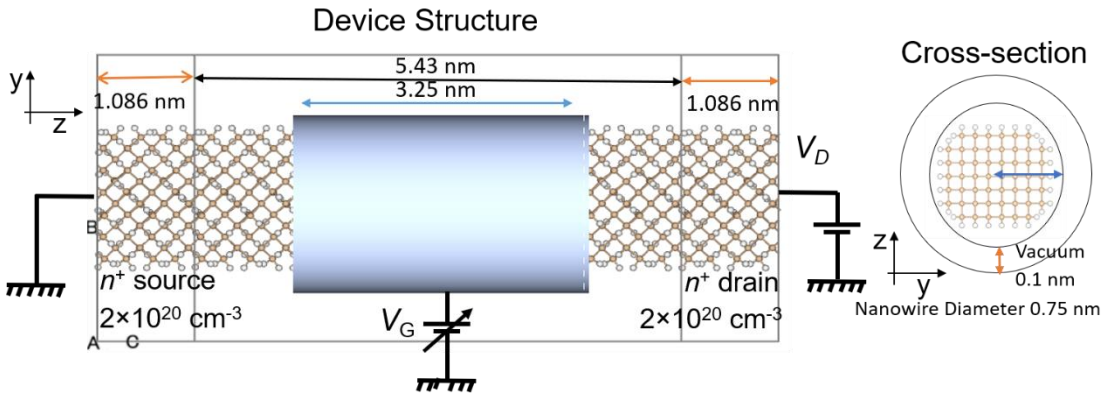

Fig. 3.1 (a) Atomistic view of gate-all-around Si(100)-nanowire transistor with n$^+$ source and drain (all dangling bonds are passivated with H). Bias circuit for *IV* measurements is shown, with V_D being the source-drain bias and V_G being the gate voltage. (b) Cross-sectional view of the gated nanowire, converting the entire structure into a basic field-effect transistor.

It should be mentioned that this structure is different from typical experimental devices, which are mostly based on Si/SiO$_2$ interfaces. However, the choice of vacuum as gate dielectric allows reproducing the gate-effect to some degree, and is sufficient for the purpose of our analysis.

3.2. Single-doping effects

Dopant atoms, embedded in nanowires or other nanostructures, can significantly influence the transport properties in a device structure. First, we

investigate the impact of even a single dopant (in the first part, mainly Phosphorous (P)) added discretely in the substitutional site. This type of dopant (a donor) is positively charged when ionized and generates a potential well that attracts (thanks to the Coulomb attraction) the electrons in its vicinity, keeping the electron inside if the tunnel barriers are high enough (higher than the thermal energy). Thus, it is expected that the presence of such a donor in the channel increases the current with respect to an intrinsic channel. Schematically, the potential profiles of intrinsic and single-doped channel are depicted in **Fig. 3.2**. Donor-induced energy states are illustrated to appear in the channel, below the conduction-band edge. In order to understand the properties of the systems under study, simulations are focused on revealing mainly local density-of-states (LDOS) spectra, simulated based on the well-established density functional theory (DFT). For revealing in even more depth these properties, electrical characteristics are also simulated using a semi-empirical Extended-Hückel method, mainly at T=300 K (defined as room temperature in this study). Current-voltage (I-V) characteristics are thus calculated using the Non-Equilibrium Green's Function (NEGF) method[17].

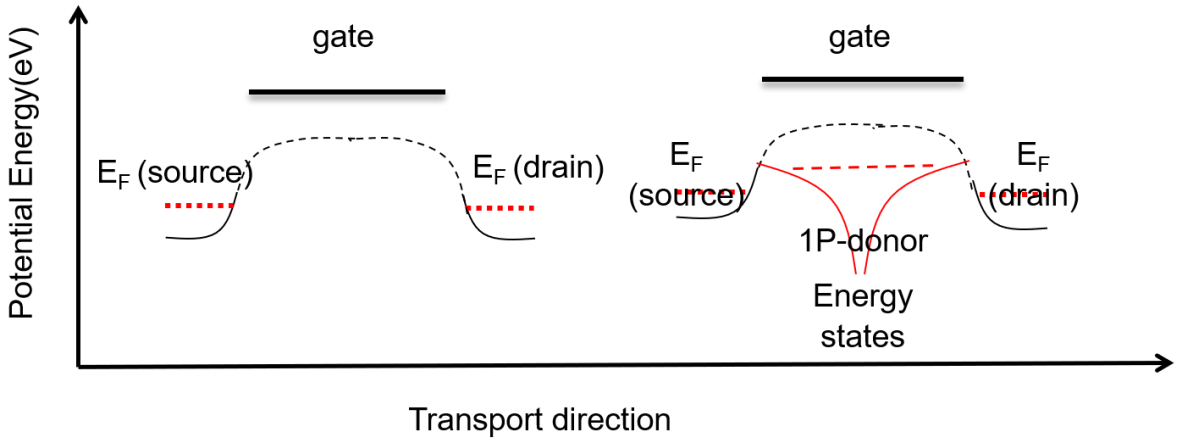

Fig. 3.2 Schematic representations of potential profiles for an intrinsic channel versus a single-doped channel (doped with a single P-donor).

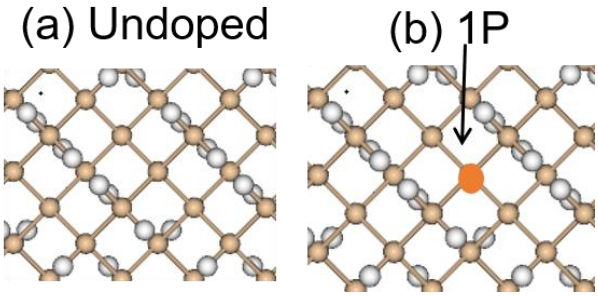

Fig. 3.3 Atomistic zoom-in views of the central regions of channels of transistors for different cases, containing: (a) no dopants; (b) a single P-donor. Dopants are indicated by arrows, while Si atoms are depicted in yellow and H atoms are depicted in white.

Figures 3.3(a)-(b) show the exposed (without a top gate) central part of Si nanowires for two main cases of interest: when no dopants are present, and when a single P-donor is doped.

Figure 3.4(a) shows the simulated I_D-V_G transfer characteristics at small bias (V_D = 5 mV) and T = 300 K for transistors with channels undoped, and single-P-doped at the central region. Both configurations clearly exhibit the *n*-channel field-effect transistor (FET) behavior. Compared to the non-doped-channel case, the onset of the I_D-V_G characteristics appears towards more negative V_G when a single P donor-atom is introduced in the channel. This shift is as expected, as the donor-induced energy states are involved in the transport. Also, current level is significantly increased, at least at lower V_G, which is clearly seen from the I_D-V_G characteristics. Another important point is that a broad peak is observed in the range V_G = 0-1 V and current saturates at higher V_G range. The emergence of this peak can be correlated with energy-states induced by the donor. The energy state correlation can be confirmed using the DOS spectrum.

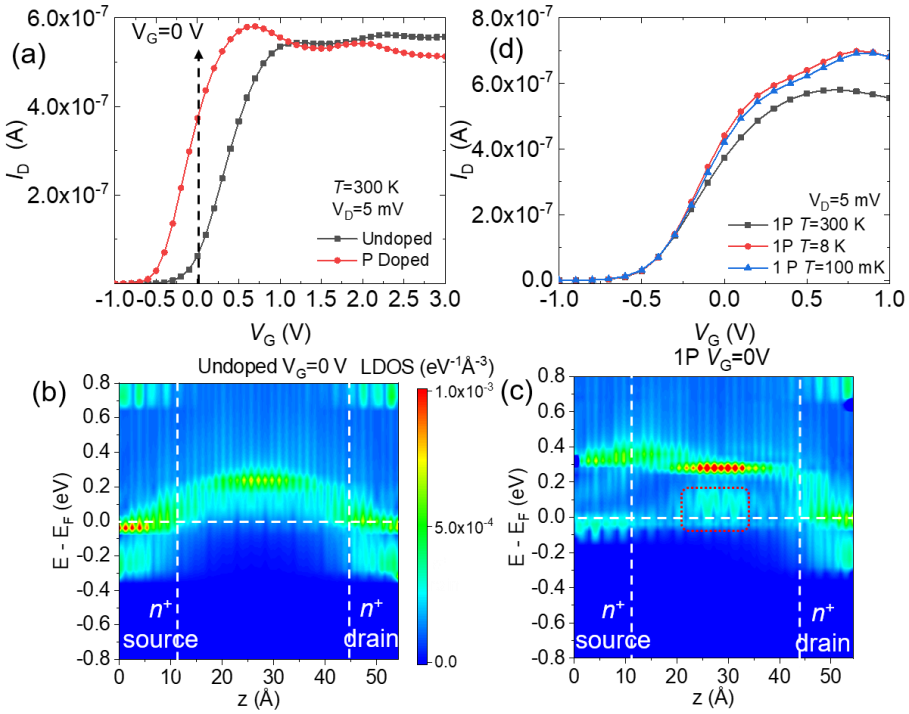

Fig. 3.4 (a) I_D-V_G characteristics for transistors (FETs) having channels that contain no dopants, and a single P-donor at T=300 K and V_D=5 mV. An arrow indicates the position of V_G=0 V. (b)-(c) Local density of states (LDOS) spectra at V_G=0 V for the above cases (Fermi level is set at E=0 eV). Color bar shown in (b) is valid for both LDOS spectra. (d) Temperature dependence of I_D-V_G characteristics (in reduced V_G range) for T=300 K, 8 K, and 100 mK. Finer structures can be observed at lower temperatures.

In order to clarify how dopant states are involved in the transport, local density-of-states (LDOS) spectra are simulated and analyzed in comparison with each other. First, it is important to focus on the basic condition of V_G = 0 V (marked by an arrow in **Fig. 3.4(a)**), which represents the "unbiased situation". The LDOS spectra for all cases under this condition are shown in **Figs. 3.4(b)-(c)**, zoomed-in near the conduction band edge, with the Fermi level (E_F) set as E_F=0 eV. From the comparison of the undoped and single-P-doped cases, it can be expected that the onset V_G shift to more negative values is due to the presence of extra energy states below the conduction band edge when the P-donor is introduced in the channel; it is known, however, that they are strongly hybridized with the Si energy states, but this should not affect the

overall behavior.[18]. At V_G = 0 V, conduction band states are already brought into the transport window while the donor-induced energy states also contribute to transport, as shown by the dashed box in **Fig. 3.4(c)** (in particular at more negative V_G values). Temperature dependence of I_D-V_G characteristics (from room temperature to low temperature, 8 K and – as a test for cryogenic temperatures – 100 mK) is shown for the case of 1P-donor in **Fig. 3.4(d)**, suggesting that finer structures can be observed.

It is important to understand more deeply the impact of the donor levels in the LDOS spectra. In bulk silicon, the conduction band is six-fold degenerate, but the degeneracy is lifted by a valley splitting when silicon is doped with a P-donor, resulting in three sets of states. These states are, in order of increasing energy, a singlet [1s (A1)], a triplet [1s (T2)], and a doublet [1s (E)]. In nano-silicon, which has dimensions below the Bohr radius of donor electron in bulk, the interaction between the donor related states and host Si conduction states becomes significant due to the strong confinement at nanoscale. It is difficult to observe the energy level splitting at higher temperature due to thermal broadening, and also because of the above-mentioned strong hybridization between the donor states and the Si states in such nanostructures. However, qualitatively, our results can be correlated with the previously reported work of electronic structure calculations performed on a single P-donor in silicon with DFT.[19] In our analysis, simulated LDOS spectra are shown in **Fig. 3.4(a)** for undoped case and 1P-donor case at T=300 K and **(d)** for 1P-donor case, at different temperatures. Comparing the undoped with Single-P-doped cases clearly shows that the energy levels are strongly packed and spread around the energy range between 0 to 100 meV. These energy levels, involved in the transport, clearly lead to the peak in I-V characteristics. Further analysis for identifying the energy level spectrum that can be ascribed to donor states should include low-temperature data, as shown in **Fig. 3.4(d)**.

3.3. Multiple-doping with donor “clusters”

A case of more practical interest is that of a “cluster” of several coupled P-donors in the channel of the nano-transistor. We choose here a most-compact case of 3 P-donors arranged in a triangular configuration, with the P-donors being second-nearest neighbors, i.e., separated by a Si-atom sandwiched in between. This is a system similar to those analyzed in other studies as a standard starting-point for the theoretical treatment of a few-donor “molecules”.[9]

Figure 3.5 shows a schematic representation of the potential profile of a 3P-“cluster” in the active region of the device. This illustrates the few discrete energy states induced by the 3P-donor “cluster”, which can be interpreted as acting similarly to a “molecule”. Coupling of the three P-donors so closely to each other is considered as the origin of the triple-splitting of the ground-state energy. It should be noted, however, that the position of some of the P-donors is “near surface”, i.e., away from the core of the nanowire, and such surface effects may contribute to the overall behavior. Further analysis of the radial-position effect will be necessary in the future.

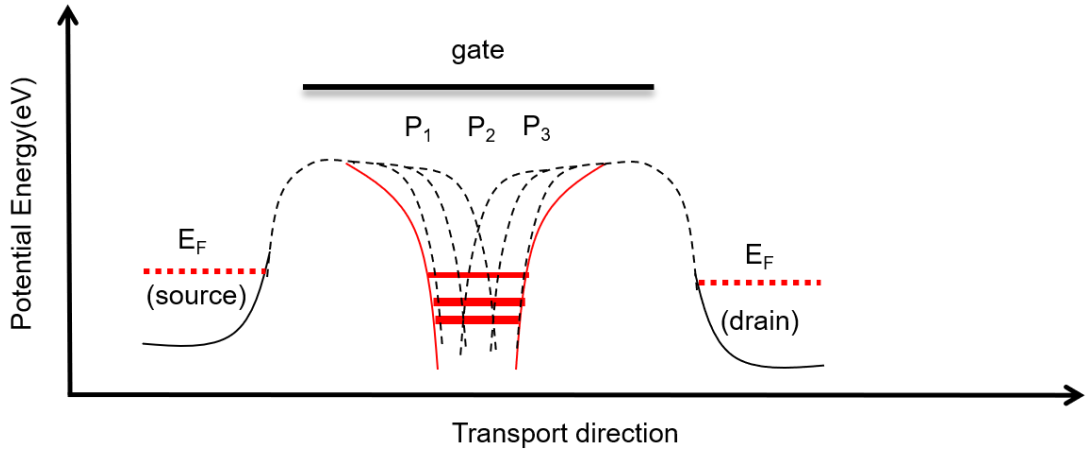

Fig. 3.5 Schematic illustration of the potential profile along the transport direction with a 3P-“cluster” in the active region of a transistor.

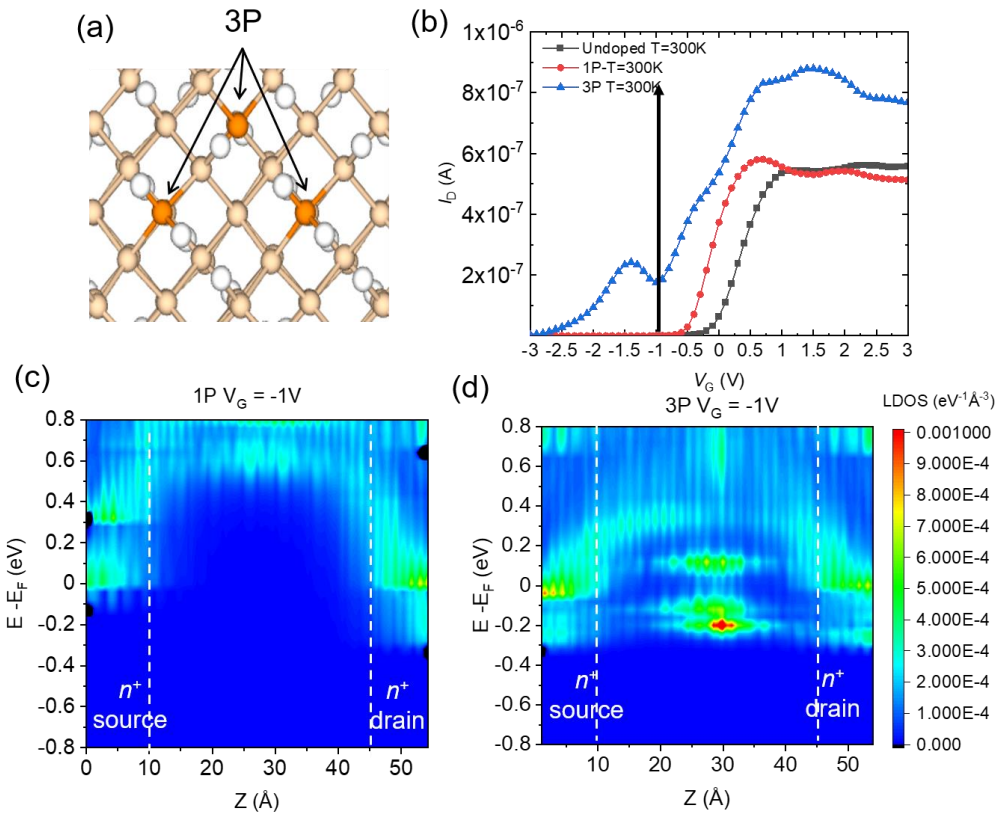

Fig. 3.6 (a) Atomistic zoom-in views of the central region containing a 3P-"cluster". (b) I_D-V_G characteristics for nanowire FETs doped with a 3P-"cluster" at V_D=5 mV and T=300 K, as a comparison with single-P doped and undoped case. Dopants are indicated by arrows, while Si atoms are depicted in yellow and H atoms are depicted in white. (c)-(d) Local density of states (LDOS) spectra at V_G = -1 V for Single-P-doped and 3P-donor cases (Fermi level is set at E=0 eV).

Figure 3.6(a) shows the exposed central part of the Si nanowire doped with a 3P-"cluster". **Figure 3.6(b)** shows the I_D-V_G characteristics for such a "cluster" of 3P-donors (V_D=5 mV and T=300 K), in comparison with single-P-doped and undoped cases, exhibiting clearly an *n*-channel FET behavior, but most importantly exhibiting also clear current inflections (peaks) in addition to the basic characteristics. As expected, current level is also higher and shifted to more negative V_G compared to single-donor (and undoped) configuration. The reason for current enhancement and shift of the onset-V_G towards more negative values is due to the energy-states from 3P-donor cluster, which are visible near conduction band edge which mediating the transport. This can be correlated with LDOS spectra shown in **Figs. 3.6(c)-(d)** at V_G=

-1 V; for the single-P configuration, the donor states are not available for transport at this voltage, while in the 3P-configuration, the donor-induced states are clear and available within the transport window even at such low V_G. At higher V_G, excited states are also involved and eventually current saturates in both cases.

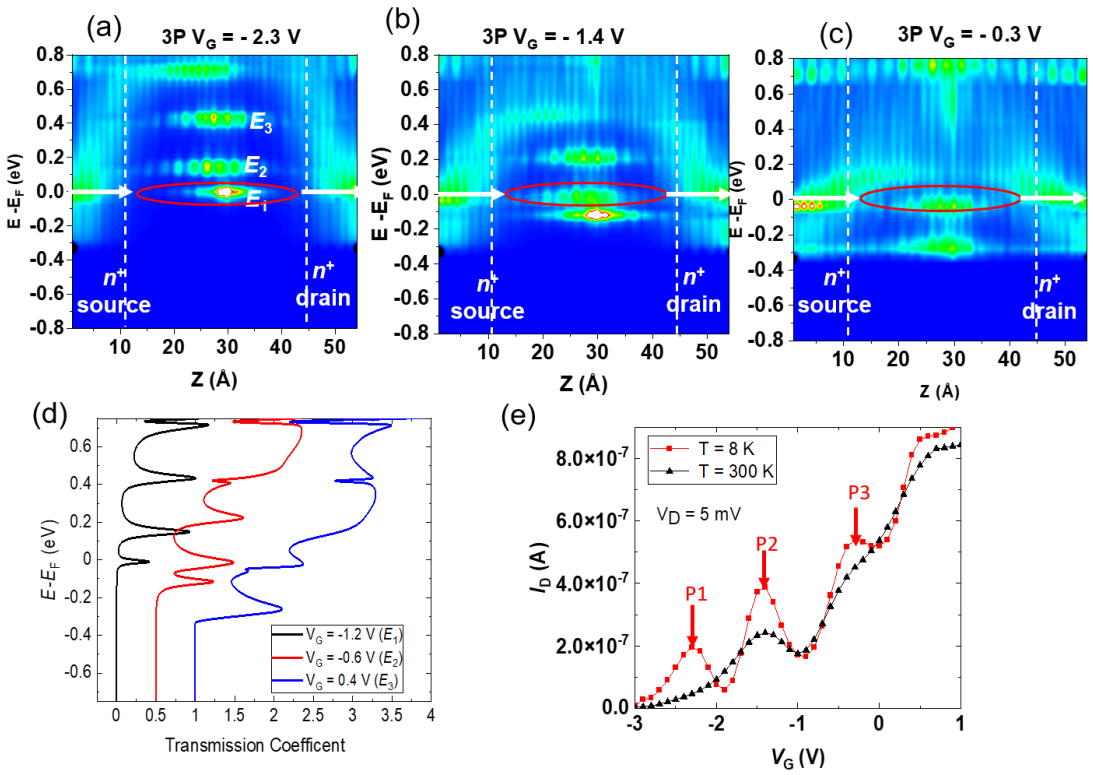

Fig. 3.7 (a)-(c) LDOS spectra for a 3P-"cluster" at V_G=-2.3 V (marked as E_1), V_G=-1.4 V (marked as E_2) V_G=-0.3V (marked as E_3) with the inset showing the discrete energy levels. (d) Transmission coefficient for different V_G values corresponding to each current peak. (e) I_D-V_G characteristics for a "cluster" of 3P donors at V_D=5 mV, but different temperatures: T=300 K and 8 K.

To elucidate the transport through the few-donor "cluster" (3P) embedded in the Si nanowire FET channel, we show in **Fig. 3.7(e)** also the I_D-V_G characteristics at low temperature (T=8 K) for V_D=5 mV. From this low-temperature analysis, it can be clearly seen that three current peaks appear at V_G=-2.3 V, -1.4 V, and -0.3 V in the I_D-V_G characteristics, with the lowest two broadening into a current envelope at room

temperature. It is not yet fully clarified why the current level is higher at low temperature than at room temperature, but this is likely related to the Fermi-Dirac distribution of the leads, which provides a narrower distribution of carriers that can be transported through the discrete energy states in the channel. As an extension, this interpretation can be aligned eventually with the theory of quantum Coulomb blockade[20], although further consideration is needed for this interpretation.

By correlation with the transmission spectra specifically selected for these peaks' V_G values, shown in **Fig. 3.7(d)**, it becomes clear that the current peaks are correlated to the transmission peaks. Furthermore, for the V_G values corresponding to each peak, LDOS analysis allows us to clarify that they arise due to the alignment of successive discrete energy states of the few-donor "cluster" with the source Fermi level (E_F), as observable from **Figs. 3.7(a)-(c)**. As the lower-index levels move below the Fermi level, a minor modification of the energy spectrum can be noticed.

It is also important to note that, due to the small dimensions of the structures studied in this work, the energy states are extended throughout the structure and transport takes place coherently between source and drain. This measurement confirms the current enhancement whenever a discrete energy level of the few-donor "cluster" is introduced, by changing the gate voltage, into the transport window.

3.4. Impacts of counter-doping on transport through a few-donor cluster

The scope of this study is to understand the role of counter-doping in such devices. In particular, the aim is to reveal the effect of B-acceptor(s) on transport through the few-donor "cluster". Therefore, we consider next the effect of introducing two (or several) B-acceptors in different configurations. We initially expected that

introduction of the Boron (B) acceptors in each “barrier” region induces the potential barrier to locally increase, which shifts the 3P-donor cluster’s energy spectrum up (as schematically illustrated in **Fig. 3.8**); however, the real situation in such ultra-small structures is that the effect of the B-acceptors is extended over the entire active region (not depicted in **Fig. 3.8**). A main configuration of interest has one B-acceptor located in each “barrier” region, i.e., in the region between the few-donor “cluster” and the leads, which is considered in the next section.

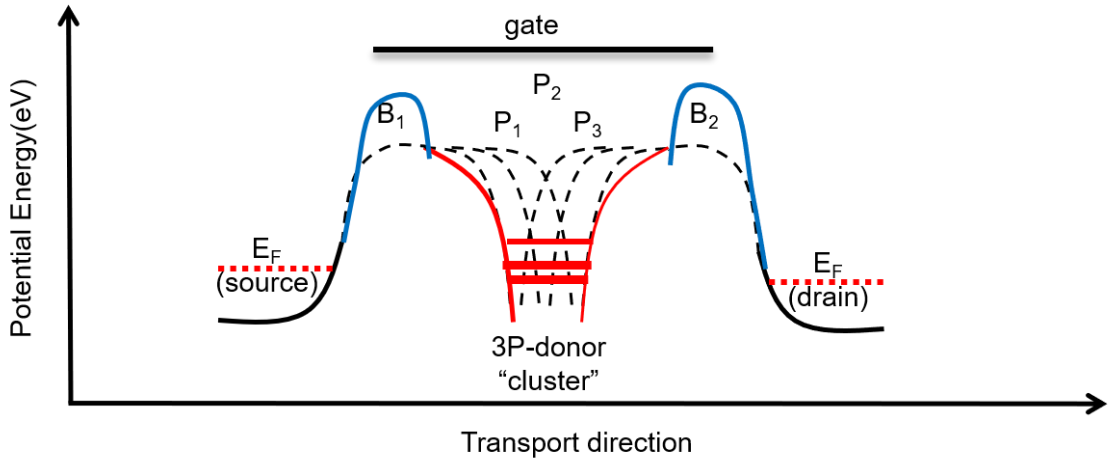

Fig. 3.8 Potential profile along the transport direction with the discrete energy states likely induced by a 3P-“cluster” flanked by B acceptors on each side in the active region. Local potential modulation is just a schematic representation, while the actual effect is more delocalized at such small scales.

3.4.1. One acceptor in each “barrier” and effect of radial position

Figure 3.9(a) shows the exposed central part of the Si nanowire doped with a 3P-“cluster” flanked by a B-acceptor on each side. **Figure 3.9(b)** shows the LDOS spectrum near the conduction band edge, at the basic condition of V_G=0 V. It can be observed that the discrete-energy spectrum, likely induced by the 3P-“cluster”, is maintained with only a minor distortion. I_D-V_G characteristics for such a 3P-2B

configuration (V_D=5 mV and T=300 K) are shown in **Fig. 3.9(c)**. The device exhibits also clearly an *n*-channel FET behavior, similarly to other cases treated so far, and also with visible current inflections (peaks).

To elucidate the transport in such Si-nanowire FETs through the few-donor "cluster" (3P) flanked by B-acceptors on each side, we show in **Fig. 3.10(e)** also the I_D-V_G characteristics at low temperature (T=8 K) for V_D=5 mV. **Figures 3.10(a)-(c)** illustrate the LDOS spectra for different V_G values (-1.2, -0.6, and 0.4 V). In particular, it should be noted that the discrete-energy spectrum induced by the 3P-"cluster" is maintained with only a minor distortion, although an extra shift in V_G is necessary to align the energy levels with the Fermi level (as compared to the 3P-"cluster" case).

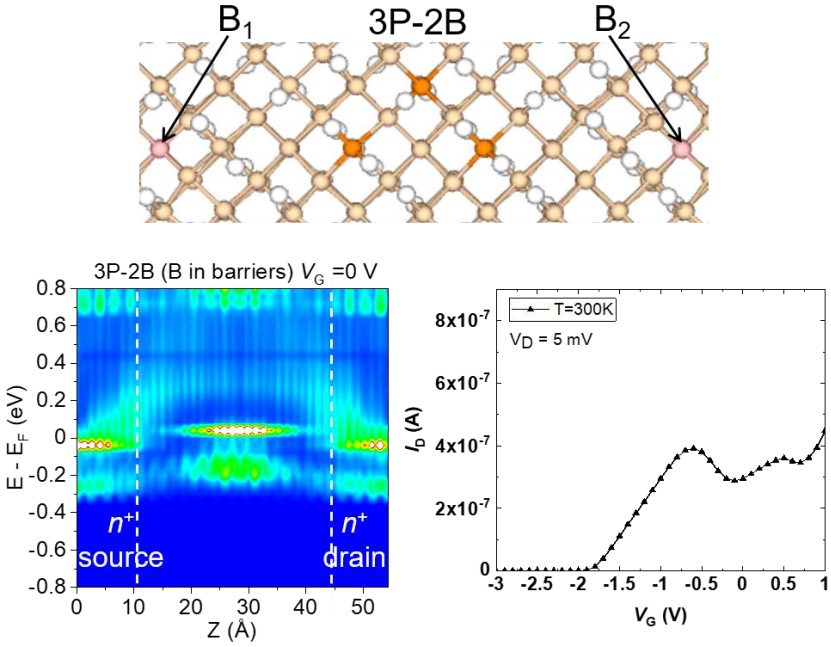

Fig. 3.9 (a) Atomistic zoom-in views of the central region containing 3P-"cluster" flanked by a B-acceptor on each side. (b) Local density of states (LDOS) spectra at V_G=0 V for the above cases (Fermi level is set at E=0 eV). (c) I_D-V_G characteristics for nanowire FETs doped with 3P cluster at V_D=5 mV and at T=300 K. Dopants are indicated by arrows, while Si atoms are depicted in yellow and H atoms are depicted in white.

From the low-temperature data, the current peaks are more clearly identified and labeled as P_1`, $P_2$`, and P_3`. The V_G values corresponding to the current peaks

are V_G = -1.2 V, -0.6 V, and 0.4 V, shown in correlation with the V_G values for the LDOS spectra in **Figs. 3.10(a)-(c)**. The transport mechanism can be clarified by observing that transmission peaks appear whenever an energy level of the few-donor "cluster" aligns with the source Fermi level. Alignment is illustrated by displaying the LDOS spectra corresponding to each current peak in **Fig. 3.10(a)-(c)**.

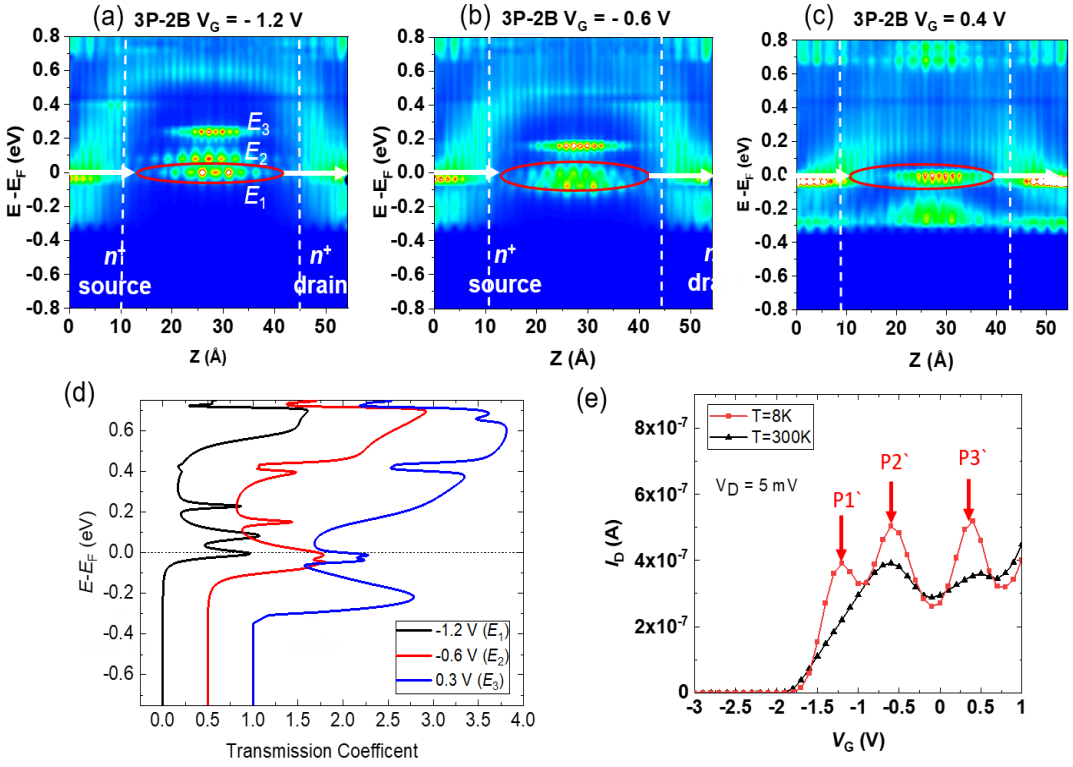

Fig. 3.10 (a)-(c) Local density of states (LDOS) spectra at different V_G values, corresponding to alignment of the 3 discrete energy levels (E_1, E_2, and E_3) to the source Fermi level for a 3P-"cluster" flanked by one B-acceptor on each side. (d) Transmission coefficient (effectively, a measure of transmission probability) for different V_G values corresponding to each current peak. (e) I_D-V_G characteristics at T=300 K (and T=8 K for reference) and at V_D=5 mV for a nanowire FET doped with a 3P-2B system; distinct current peaks at V_G values correlated with (a)-(c) are labeled as P_1', P_2', P_3'.

There are fine differences in the shape and features observed in the I_D-V_G characteristics by comparing the 3P and 3P-2B cases: a higher current level for the broad lower current envelope for the 3P-2B case, and a lower level for the higher-V_G

peak. These differences can be ascribed to the changes in the energy distribution and spatial expansion of the energy states when B-acceptors are introduced in the “barrier” regions. The presence of the B-acceptors makes the lower two energy states closer to each other, which then implicitly gives rise to a higher-current envelope at room temperature considering thermal broadening. It is not yet fully understood what is the origin of this spatial modification induced by the presence of the B-acceptors and additional study is necessary to clarify this issue.

In such co-doped Si nanowires, an important effect is the stability of the dopants at different positions near the surface, related to the segregation[21-24] trend, and relative to the 3P-“cluster”. Although both types of dopants, P-donors and B-acceptors, have a tendency to occupy sites close to the surface, there is a stronger segregation trend for B-acceptors, while P-donors prefer positions closer to the core. Due to this consideration, it is chosen here to focus more on the effect of the position of the B-acceptors, while the few-donor “cluster” is specifically arranged slightly off-axis towards the surface (not symmetrically distributed around the nanowire axis). In the following, we analyze the I_D-V_G characteristics of several 3P-2B cases, while the two B-acceptors are simultaneously shifted from on-axis sites, relative to the 3P-“cluster” location (labeled as 1) to near-surface sites (labeled as 5).

The I_D-V_G characteristics for these different 3P-2B cases (with B-atoms shifted from position 1 to position 5), simulated for T=300 K and V_D=5 mV, are shown in **Fig. 3.11(b)** as a function of B-acceptors’ positions (correlated with the notations in **Fig. 3.11(a)**). Overall, it can be seen that the characteristics are similar, suggesting the robustness of the results against changing positions of B-acceptors. It should be noted, however, that the small dimensionality of the nanowire in this case must be taken into consideration. At a closer look, it can be noticed that I_D-V_G characteristics

exhibit small shifts when the B-atoms are in different atomic planes (occupying positions 1 and 3, as compared to positions 2 and 4), with a more significant change occurring when the B-acceptors are both at positions 5. We can expect that the B-position effect is significant for position 5, but these results show that the atomistic-position effect is also distinguishable even when the B-acceptors are closer to central positions. These observations indicate that the effect of the atomistic position is noticeable, although the change of B-acceptor positions does not produce a dramatic change of the I_D-V_G characteristics. Further analysis can show how to leverage this effect for new functionalities. It is also necessary to extend the analysis to study the preferable positions of the B-acceptors, clarifying whether or not such symmetric positions of the B-acceptors in the "barriers", around a few-donor "cluster", can be obtained as a result of the natural trend of segregation and aggregation of the dopants (donors and acceptors) in Si nanowires. This study is, however, beyond the scope of this work.

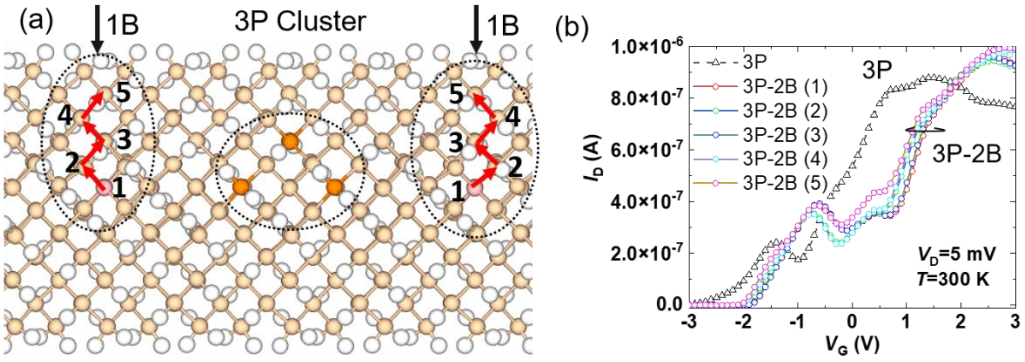

Fig. 3.11 (a) Illustration of changes in B-atoms' positions (simultaneously shifting both B-atoms) around a 3P-"cluster" (encircled in the center, slightly off-axis). (b) I_D-V_G characteristics (T=300 K and V_D=5 mV) for the 3P-2B case (with B-atoms shifted from position 1 to position 5). For clarity, different positions are indicated by arrows on the curves.

3.4.2. Multiple acceptors in each “barrier”

Finally, in order to clarify further the impact of B-acceptors in transport, we also analyze the effect of increasing the number of B-acceptors. For that, we introduce one and two more pairs of flanking B-acceptors in the regions between the 3P-“cluster” and the leads, as shown in **Fig. 3.12(a)**. Some of the B-acceptors are located “near surface” due to the small cross-section of the nanowires. By monitoring the I_D-V_G characteristics, as shown in **Fig. 3.12(b)**, it can be seen that the specific structure of the several peaks is reproduced, but continuously shifted to more positive V_G as the number of B-acceptors is increased. At the same time, the intensity of the current is also modulated, which suggests that introducing an increasing number of B-acceptors leads not only to an overall shift of the potential, but also likely to a modification of the electron wave function expansion.

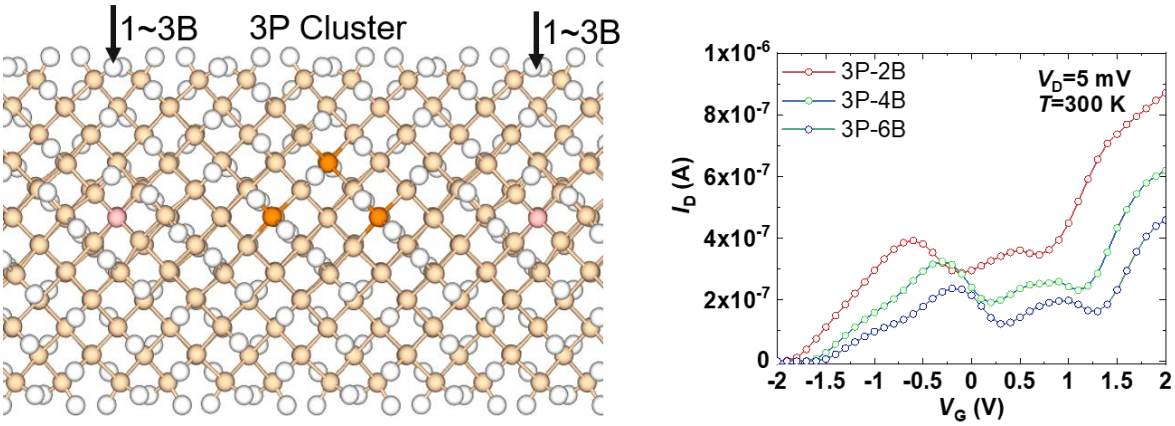

Fig. 3.12 (a) Illustration of increasing number of B-acceptors in the “barrier” regions between the 3P-“cluster” and the leads. (b) I_D-V_G characteristics (T=300 K and V_D=5 mV) for the systems with increasing number of B-acceptors flanking the 3P-“cluster”.

3.5. Few-acceptor clusters in the presence of donors

To confirm the validity of the proposed interpretation, the counterpart cases of 3B-acceptor “clusters” are also evaluated in transport, including also the effect of the

presence of P-donors in the “barrier” regions. For that, the study considers *p*-type Si-nanowire FETs. For this study, the atomistic structure of the gate-all-around Si-nanowire transistor is the same as for the *n*-type FETs (same dimensions and parameters), as shown in **Fig. 3.13**, except for the fact that the electrodes are now p^+-type source and drain regions of lengths of 1.086 nm, electrostatically doped at a concentration $N_A = 2\times10^{20}$ cm^{-3}, while in the channel B-acceptors (and P-donors) are added substitutionally. The gated transistor structure is generated by placing a metal gate around the channel (gate-all-around), separated with a thin vacuum layer; as explained for the *n*-type FET case, this allows the gate effect to be analyzed with sufficient similarity to typical FETs, although for such experimental devices Si/SiO_2 layers are utilized. **Figures 3.13(a)-(c)** show the atomistic zoom-in views of the central regions for different cases, containing: (a) no dopants (i.e., undoped); (b) a single B-acceptor (1B); (c) a single donor-acceptor (1P-1B) pair.

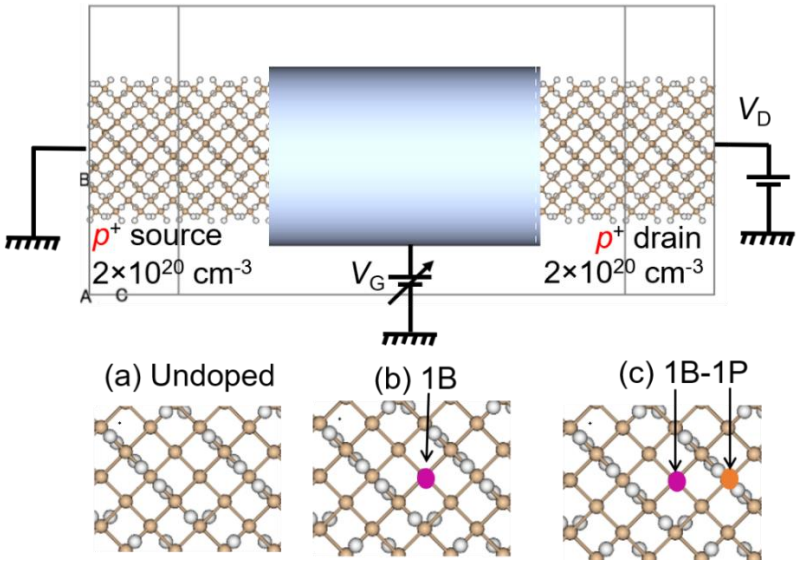

Fig. 3.13 Atomistic view of gate-all-around Si (100)-nanowire transistor with p^+-type source and drain (all dangling bonds are passivated with H). Bias circuit for *IV* measurements is also shown. Atomistic zoom-in views of the exposed central regions for different cases, containing: (a) no dopants (undoped); (b) a single B acceptor (1B); (c) a single donor-acceptor (1P-1B) pair. Dopants are indicated by arrows, while Si atoms are depicted in yellow and H atoms are depicted in white.

Figure 3.14(d) shows the simulated I_D-V_G transfer characteristics at small bias (V_D = 5 mV) and T = 300 K for transistors with channels containing no dopants, single-B-doped, and B-P co-doped, i.e., doped with a 1B-1P Acceptor-Donor pair. All the configurations clearly exhibit the *p*-channel field-effect transistor (FET) behavior, opposite to the cases shown in the previous sections. This confirms the validity of this structure and basic interpretation.

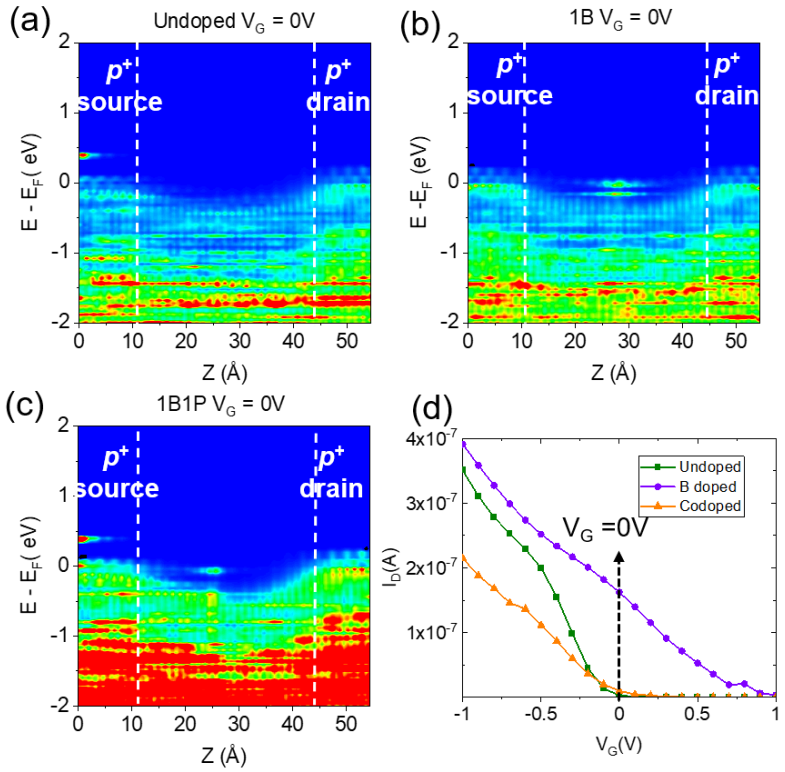

Fig. 3.14 (a)-(c) Local density of states (LDOS) spectra at V_G=0 V for the above cases (Fermi level is set at E=0 eV). (d) I_D-V_G characteristics for transistors with channels containing: no dopants (undoped), single-B-acceptor, and co-doped (1B-1P), at T=300 K and V_D=5 mV; V_G=0 V is indicated by an arrow.

Compared to the undoped-channel case, the onset of the I_D-V_G characteristics shifts towards more positive V_G when a single B acceptor-atom is introduced in the channel, while it shifts significantly towards more negative V_G when a P-donor is also added near the acceptor atom (with a Si atom in between). This result shows that

even such atomistic co-doping, with a closely located P-B pair, produces a result significantly different from the initial case of an undoped Si nanowire which is consistent with the behavior of the *n*-FET nanowire transistor, as well. The presence of acceptor states and donor induced potentials can be clearly seen from the LDOS, simulated this time near the valence band edge, as reported in **Fig. 3.14(a)-(c)**.

The main objective is to elucidate the effect of the 3B-acceptor “cluster”, considering also the presence of donors flanked on each side (as schematically indicated), focusing on the transport properties. **Figure 3.15(a)** shows the exposed central part of the Si nanowire doped with a 3B-“cluster” flanked by a P-donor on each side. **Figure 3.15(b)** shows the LDOS spectrum at the basic condition of V_G=0 V, with clear signatures of energy states induced by the 3B-acceptor “cluster” near the valence band. These energy levels are expected to contribute to the enhancement of the current. **Figure 3.15(c)** shows the LDOS spectrum for 3B-2P at V_G =0 V, including also the signatures of the energy states possibly introduced by the 3B-acceptor “cluster”, with enhanced potential due to the presence of the P-donor(s).

Figure 3.15(d) shows I_D-V_G characteristics for 3B and 3B-2P cases, all exhibiting typical *p*-FET characteristics, shown here in linear scale. For more clarity, semi-log plots are also presented in **Fig. 3.15(e)**, and, as such, fine peaks (current modulations) are observed over the positive V_G range. Clearly, overall current enhancement is observed with small inflections and shifted towards more negative V_G for 3B-2P case, likely due to the enhanced potential created by the P-donors. The origin of the small peaks or features is not yet clarified, and further study is necessary.

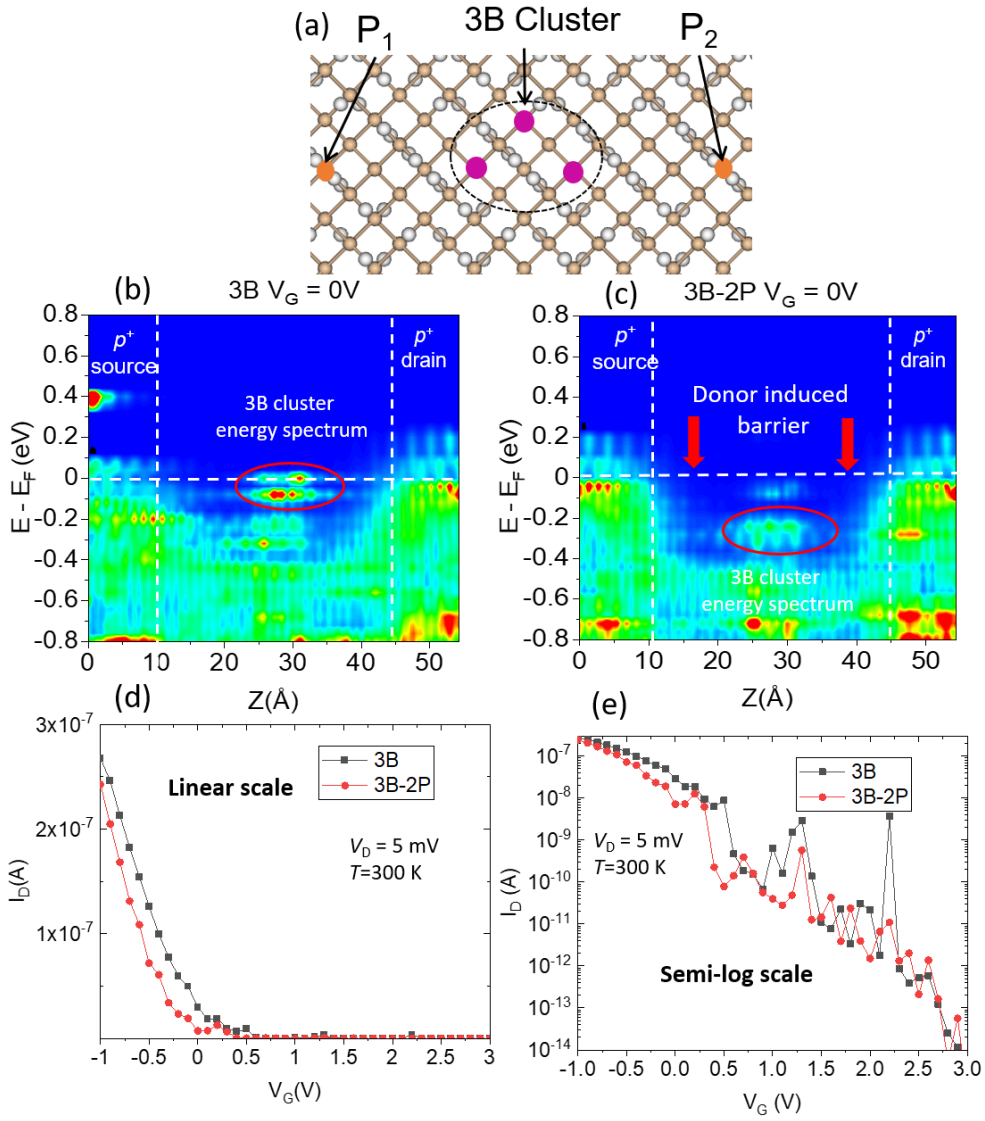

Fig. 3.15 (a) Atomistic zoom-in views of the central region containing a 3B-acceptor "cluster" flanked by a P-donor on each side. (b) Local density of states (LDOS) spectra at V_G=0 V for the above cases (Fermi level is set at E=0 eV). (c) I_D-V_G characteristics for nanowire FETs doped with a 3B-"cluster" and a 3B-"cluster" flanked by a P-donor on each side, at V_D=5 mV and at T=300 K. Dopants are indicated by arrows, while Si atoms are depicted in yellow and H atoms are depicted in white.

3.6. Conclusions

In this chapter, we have shown that the energy spectrum of a few-donor "cluster", embedded in a gate-all-around device structure within a H-passivated

Si(100) nanowire as channel, contains distinguishable discrete energy levels below the conduction band edge, corresponding to current peaks in the I_D-V_G characteristics, observed even at room temperature. Most importantly, we found that B acceptor-atoms can induce a shift of the energy spectrum of the few-donor “cluster”, and implicitly affect its transport properties, depending on the location and number of the acceptors. The B-acceptors contribute basically to raising the overall potential, with only a small distortion to the energy spectrum of the “cluster”. Moreover, the results are basically robust against a change of positions of the B-acceptors towards the surface (away from axis of the 3P-“cluster”), with only small, albeit detectable changes depending on the atomistic positions of the acceptors. On the other hand, transport characteristics depend systematically on the number of B-acceptors introduced in the system. This finding can suggest the possibility of controlling transport through the donor states, with significant modulation from the acceptors nearby.

We have also shown a complementary analysis of devices working as *p*-type transistors, with 3B-“cluster” and 3B-“cluster” flanked by a P-donor on each side. This counterpart system also shows the energy spectrum induced most likely by the 3B “cluster” and the potential modifications due to P-donors, all changes being visible near the valence band edge. These energy states, modified by the different configuration of dopants, contribute to the current enhancement.

These findings suggest a pathway for utilizing counter-doping of Si nanowires, either by precise-doping techniques, or by controlling the fundamental mechanisms of segregation and aggregation that could be affected by the interaction between donor- and acceptor-atoms in such nanostructures. This study can also open new perspectives for using counter-doping in Si-nanowire transistors as a platform for developing applications for the next generation of *dopant-based electronics*.

References

[1]D. Moraru, A. Udhiarto, M. Anwar, R. Nowak, R. Jablonski, E. Hamid, J. C. Tarido, T. Mizuno, and M. Tabe, Nanoscale Res. Lett. **6**, 479 (2011).

[2]E. Hamid, D. Moraru, Y. Kuzuya, T. Mizuno, L. T. Anh, H. Mizuta, and M. Tabe, Phys. Rev. B **87**, 085420 (2013).

[3]B. Weber, Y. H. Matthias Tan, S. Mahapatra, T. S. Watson, H. Ryu, R. Rahman, L. C. L. Hollenberg, G. Klimeck, and M. Y. Simmons, Nat. Nanotechnol. **9**, 430 (2014).

[4]M. F. Gonzalez-Zalba, A. A. Saraiva, M. J. Calderón, D. Heiss, B. Koiller, and A. J. Ferguson, Nano Lett. **14**, 5672 (2014).

[5]D. Moraru, A. Samanta, L. T. Anh, T. Mizuno, H. Mizuta, and M. Tabe, Sci. Rep. **4**, 6219 (2014).

[6]A. Samanta, M. Muruganathan, M. Hori, Y. Ono, H. Mizuta, M. Tabe, and D. Moraru, Appl. Phys. Lett. **110**, 093107 (2017).

[7]M. Fuechsle, J. A. Miwa, S. Mahapatra, H. Ryu, S. Lee, O. Warschkow, L. C. L. Hollenberg, G. Klimeck, and M. Y. Simmons, Nat. Nanotechnol. **7**, 242-246 (2012).

[8]H. Büch, S. Mahapatra, R. Rahman, A. Morello, and M. Y. Simmons, Nat. Commun. **4**, 2017 (2013).

[9]M. V. Klymenko, S. Rogge, and F. Remacle, Phys. Rev. B **95**, 205301 (2017).

[10]F. Iori, E. Degoli, R. Magri, I. Marri, G. Cantele, D. Ninno, F. Trani, O. Pulci, and S. Ossicini, Phys. Rev. B **76**, 085302 (2007).

[11]I. Marri, E. Degoli, and S. Ossicini, Prog. Surf. Sci. **92**, 375 (2017), and references therein.

[12]Y. Ma, X. Chen, X. Pi, and D. Yang, J. Nanopart. Res. **14**, 802 (2012), and references therein.

[13]R. Rurali, Rev. Mod. Phys. **82**, 427 (2010).

[14]T. Markussen, R. Rurali, A.-P. Jauho, and M. Brandbyge, Phys. Rev. Lett. **99**, 076803 (2007).

[15]M. Bescond, M. Lannoo, L. Raymond, and F. Michelini, J. Appl. Phys. **107**, 093703 (2010).

[16]D. C. Liu and J. Nocedal, Math. Program. **45**, 503 (1989).

[17]K. Stokbro, D. E. Peterson, S. Smidstrup, A. Blom, M. Ipsen, and K. Kaasbjerg, Phys. Rev. B **82**, 075420 (2010).

[18]L. T. Anh, D. Moraru, M. Manoharan, M. Tabe, and H. Mizuta, J. Appl. Phys. **116**, 063705 (2014).

[19]J. S. Smith, A. Budi, M. C. Per *et al. Sci Rep* **7,** 6010 (2017).

[20]Y. Meir, N. S. Wingreen, and P. A. Lee, Phys. Rev. Lett. **66**, 3048 (1991).

[21]M. V. Fernandez-Serra, C. Adessi, and X. Blasé, Phys. Rev. Lett. **96**, 166805 (2006).

[22]N. Fukata, S. Ishida, S. Yokono, R. Takiguchi, J. Chen, T. Sekiguchi, and K. Murakami, Nano Lett. **11**, 651 (2011).

[23]B. Schoeters, O. Leenaerts, G. Pourtois, and B. Partoens, J. Appl. Phys. **118**, 104306 (2015).

[24]M. Amato, S. Ossicini, E. Canadell, and R. Rurali, Nano Lett. **19**, 866 (2019).

Chapter 4: Impacts of donor-acceptor systems on band-to-band tunneling transport in Si nano-diodes

4.1. Importance of donors and acceptors in nanoscale depletion layers

Tunnel diodes, widely known as Esaki diodes,[1,2] are semiconductor devices working based on a band-to-band tunneling (BTBT) transport mechanism, demonstrated in highly-doped p^+-n^+ junctions initially in Ge and then in Si.[3–10] This transport mechanism is based on the tunneling of electrons between the heavily-doped (degenerately-doped) p^+ and n^+ regions. This critical transport takes place through the depletion-layer of the highly-doped p^+-n^+ junction (with depletion-layer width on the order of ~10 nm or less); it should also be noted that, when the device is downscaled towards the atomic-scale, the indirect bandgap nature of Si has been reported to also change into quasi-direct bandgap nature, which may also benefit BTBT transport.[11,12] However, BTBT transport mechanisms reported so far generally include the assistance of phonons (required for momentum conservation) and such behavior remains valid even in nanoscale Esaki diodes (with dimensions on the order of 100 nm), as reported by Schmid *et al*.[8]

Tunnel diodes are formed from p^+-n^+ junctions, where both the *p*- and *n*-type regions are degenerately doped, so that the Fermi energies of both sides lie inside the bands[2] (valence band of the *p*-type region and conduction band of the *n*-type region), as schematically shown in **Fig. 4.1**.

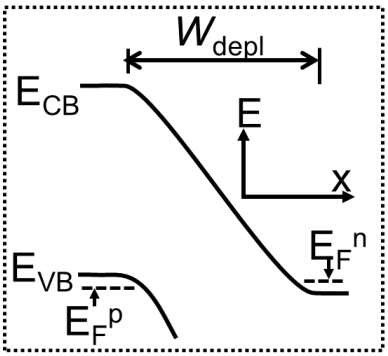

Fig. 4.1. Schematic of the energy band diagram of an Esaki diode in equilibrium, showing degenerately-doped p^+- and n^+-regions around the depletion-layer of width W_{depl}.

The charge-transport mechanisms in Esaki diodes[2] can be analyzed from typical current-voltage (*I*-*V*) characteristics, as shown in **Fig. 4.2(a).** In the reverse-bias regime (V<0 V), the current monotonically increases and is relatively high (in contrast to practically zero current in regular *p*-*n* diodes). In the forward-bias regime (V>0 V), the current increases to a maximum value (indicated as the peak current I_P at $V=V_P$), then decreases to a minimum value (marked by the valley current I_V at $V=V_V$), forming a so-called negative differential conductance (NDC) region. Beyond the $V=V_V$ point, the current exponentially increases with the applied bias. The overall characteristics in the forward-bias regime can be divided, thus, into three main parts,[13] depending on the dominant transport mechanism: (i) band-to-band tunneling,[2,3,8-10] (ii) excess current;[4] and (iii) thermally-activated current, similar to regular *p*-*n* diodes. These components are schematically illustrated (decomposed) in the characteristics shown in **Fig. 4.2(b)**.

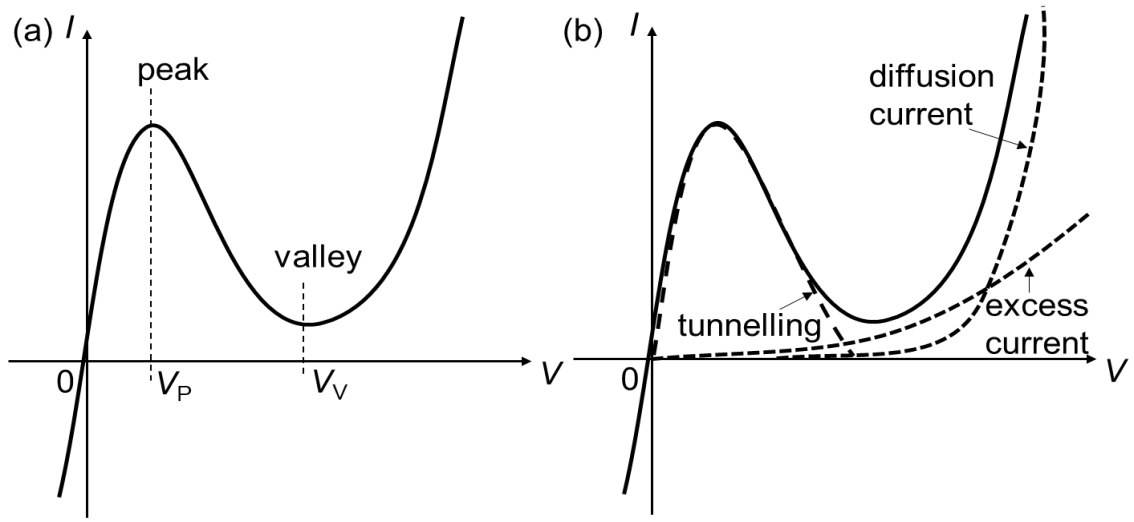

Fig. 4.2. Current-voltage (*I*-*V*) characteristics of an Esaki diode showing: (a) peak voltage V_P and valley voltage V_V. (b) Different current components decomposed schematically in the forward-bias regime (V>0 V): BTBT (tunneling), excess current, and diffusion current.

In the past several years, however, BTBT transport mediated by dopant states has been reported in low-dimensional Esaki diodes,[9,10] while the effects of discrete dopants in transport in *pn* diodes with lower doping concentration had been known from previous studies.[14,15]

In Si p^+-i-n^+ diodes or tunnel field-effect transistors (TFETs,[16] if a gate is available), transport mediated by deep states, induced by Al-N iso-electronic traps (IETs), has also been recently reported.[17,18] In these devices, the authors reported current enhancement[17] and even signatures of single-electron tunnelling[18] when such IETs are doped in an intrinsic (*i*) region. These results suggest the importance of bandgap energy states in potentially enhancing the BTBT current in Si devices. From a different perspective, it is also important to understand the effect of the high electric field in such highly-doped p^+-n^+ diodes and the induced modifications in the energy spectrum near the band edges, including the effects introduced by conventional dopants; these effects are not fully understood yet.[19] On this background, the main purpose of this work is to analyze and clarify the effects of front-side dopants present

in nanoscale depletion-layers, in particular in terms of their impact on the BTBT transport mechanism.

4.2. The case of undoped central region

In this Chapter, the focus is on the analysis and clarification of the key factors that quantify the impact of phosphorus (P) donor interacting with boron (B) acceptor in modulating the BTBT transport. For that purpose, an analysis based on first-principles (*ab initio*) and semi-empirical simulations is used, as briefly explained in **Chapter 2**.

For this study, the atomistic structure of the Si-nanowire p^+-n^+ diode is built using Quantum ATK software, with a <100> orientation along the transport direction (labeled as Z in this study), a central region of 5.43 nm in length (along Z direction) and a cross-sectional dimension of about 1 nm; a simulated atomistic structure is shown in **Fig. 4.3**. This structure is optimized using an in-built optimizer[20] with maximum forces of 0.05 eV/Å. All dangling bonds are passivated by H atoms. The p^+-n^+ diode is generated from this structure with p^+ and n^+ leads of lengths of 1.086 nm, electrostatically-doped at a concentration $N_{D,A} = 2\times10^{20}$ cm^{-3} (with similar extensions mirrored inside the central region, for the same distance of 1.086 nm).

Several cases are investigated in parallel for clarifying the physics of these devices: (i) p^+-n^+ diodes with undoped central region; (ii) p^+-n^+ diodes containing discrete P-donor and B-acceptor in the central region. The radial positions of the P- and B-atoms are also critical and should be treated carefully in the analysis. In most of this chapter, however, extreme cases are analyzed with the P- and B-atoms placed on the surface (or sub-surface) of the nanowire; such position does not always correspond exactly to a typical definition of “dopant”, which assumes that the P- and

B-atoms are bonded to 4 surrounding Si atoms, but it allows nevertheless the analysis of results for one limit system. It is also important to note that there are reports regarding the tendency of dopant-atoms to occupy sub-surface positions in Si nanostructures, as the formation energy can be minimized in such cases.[21] Different from this, several examples are also shown for systems more consistent with the conventional interpretation of dopants, with P- and B-atoms incorporated substitutionally within the core of the Si nanowire. Further analyses are still desired to complete the entire picture, including systems with intermediate radial positions of the dopants. However, the preliminary results presented here, through several examples, illustrate the basic properties of these systems and provide a platform for these additional analyses, to be carried out later.

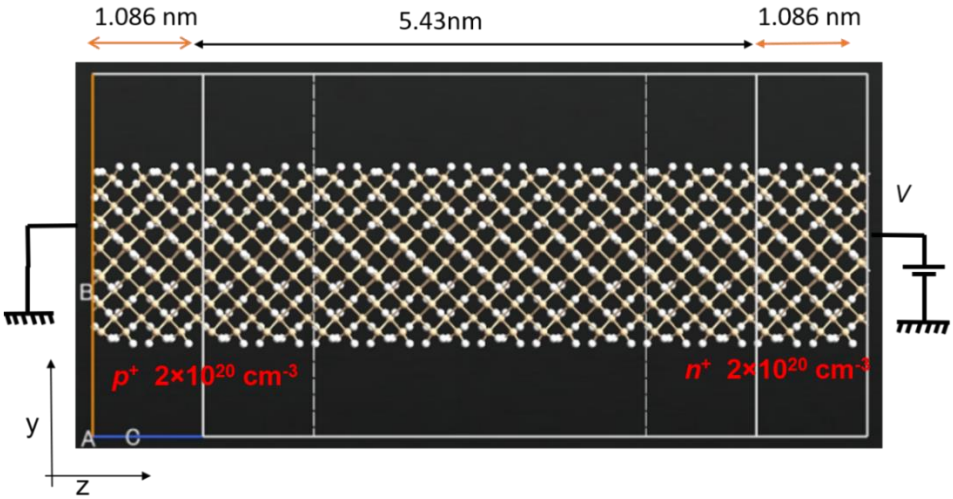

Fig. 4.3 Atomistic view of p^+-n^+ diode with electrostatically-doped leads of doping concentration $N_{D,A}$ = 2×10^{20} cm^{-3} (all dangling bonds are passivated with H in the entire structure). The bias circuit for the *IV* simulations is also shown, with *V* being the bias voltage. (Solid lines delineate the boundaries between "external" leads and central region, while the dashed lines delineate the edge of the leads, as electrostatically expanded inside the central region.)

First, in order to confirm the typical behavior of the simulated diode, *I*-*V* characteristics are simulated at *T*=300 K for the no-dopant case, illustrated in **Fig. 4.3**,

which is used as a reference case in this study. **Figure 4.4(a)** shows the simulated *I-V* characteristics, which clearly show the main signatures of the Esaki-diode characteristics. In the forward-bias region, the negative differential conductance (NDC) peak is observed, while, in the reverse-bias region, high current is observed, likely due to BTBT transport, as explained in the tunnel-diode behavior shown in **Fig. 4.2**. It should be noted, however, that excess current is not included in the simulations and also phonon-assistance in the BTBT transport is not considered at this stage. In addition, the typical diffusion current of *p-n* diodes also appears at much higher *V* values in forward-bias region due to larger bandgap, expected for such nanostructures as considered in these simulations.

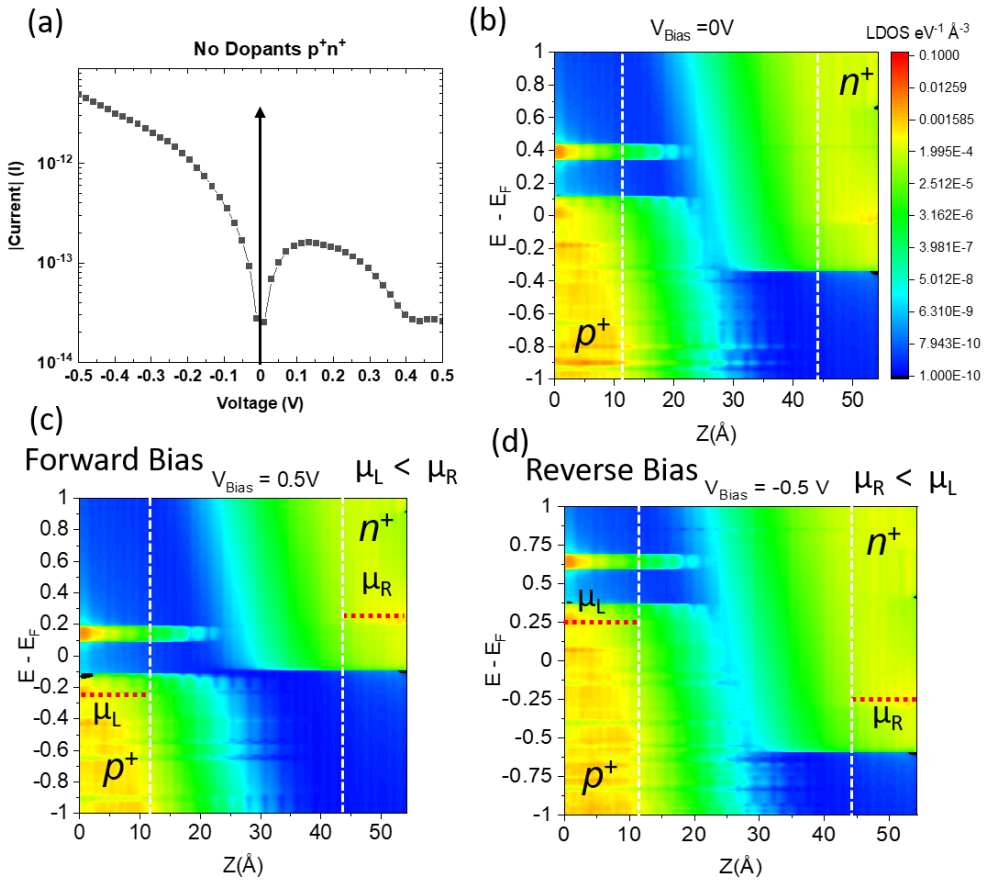

Fig. 4.4 (a) *I-V* characteristics for p^+-n^+ diode that contains no dopants in the central region, at *T*=300 K. An arrow indicates the position of V_{bias}=0 V. (b)-(d) Local density of states (LDOS) spectra at V_{bias}=0 V, 0.5 V, -0.5 V, corresponding to the cases considered as Zero-bias, Forward-Bias and Reverse-Bias (Fermi level is set at *E*=0 eV). The color bar shown in (b) is valid for all LDOS spectra.

In order to confirm the BTBT mechanism, we simulate the Local Density of States (LDOS) spectra, which also helps visualize the boundary between the electrodes and the central region and the situation near the band edges. From this visualization, it is easier to understand the energy ranges corresponding to the transport window between the p^+ and n^+ leads. **Figure 4.4** shows the LDOS spectra for different regions, starting with V_{bias}=0 V, from which the Fermi levels for the left and right leads (μ_L and μ_R) can be identified, including the effects due to the degeneracy, as illustrated in **Fig. 4.1**. At zero bias, the Fermi levels of the (degenerately doped) p^+- and n^+- quasi-neutral regions are aligned. Naturally, at this instance, zero current flows through the diode.

In the bias regime defined by $0 < V < V_P$, a larger number of unoccupied states in the valence band of the p^+-region become available as bias is increased, leading to an increase in the current, as can be observed in the range 0 V < V < 0.2 V in **Fig. 4.4(a)**. At $V = V_P$, the Fermi level of the p^+-region is basically aligned in energy with the conduction band edge of the n^+-region. In this case, a maximum BTBT-current can be expected, thereby giving a peak which can be observed at V=0.12 V in this case (see **Fig. 4.4(a)**). As the forward-bias voltage is further increased, the number of unoccupied states decreases again, as fewer unoccupied states are available in the transport window, leading to a decrease in BTBT current, as can be clearly seen between 0.4 V to 0.5 V. This situation, with the bandgap entering in the transport window, is visible in **Fig. 4.4(c)** from the LDOS spectra at V_{bias} = 0.5 V; it should be noted here that the chemical potential of the right electrode (μ_R) is higher than the chemical potential of the left electrode (μ_L). In the reverse-bias regime (V < 0 V), the electrons tunnel from the valence band of the p^+-region to the conduction band of the n^+-region, as can be confirmed from **Fig. 4.4(d)**, based on the LDOS spectra at V_{bias}

= -0.5 V; here, it should be noted that the chemical potential of the left electrode (μ_L) is higher than the chemical potential of right electrode (μ_R).

4.3. The case of electrostatically-doped p^+-n^+ diodes

Figure 4.5(a) shows the atomistic view of p^+-n^+ diode with electrostatic doping extending inside the central region, thus reducing the effective central-region length considered for this study. This analysis aims to reveal the dependence of the BTBT current on the width of the tunnel-barrier, here considered as undoped central region.

By introducing electrostatic doping (at concentration N=2×10^{20} cm^{-3}) systematically increasing the volume towards the center of the structure, the central region length changes from 32.5 Å (initial case) to 0 Å (face-to-face electrostatic doping). A total number of six cases are considered in this study and the corresponding *I*-*V* characteristics are simulated at T=300 K. [In some analyses, we restrict ourselves within forward-bias regime due to the computational-time limitations and due to an increased complexity of analysis in a wider range of bias.]

Figure 4.5(b) shows the *I*-*V* characteristics for all the cases considered for this analysis. It is evident that the current level is increasing systematically by decreasing the central-region length. It is expected that an exponential increase of the tunneling rate (**Γ**) and, implicitly, an exponential increase of the BTBT current, would be observed with the systematic decrease of the central-region length. The dependence on the central-region length of the BTBT current is given in **Fig. 4.5(c)** for an example of bias voltage, V=0.2 V and the systematic current reduction is evident. The actual current could be validated by calculating the tunneling rate using the Wentzel-Kramers-Brillouin (WKB) approximation. However, it is also observed from **Fig. 4.5(c)**

that a small deviation (Δ*I*) appears between the actual current and the ideal current (expected trend of tunneling rate), increasing as the distance between the leads decreases. This may be ascribed to the formation of a natural depletion layer as the p^+ and n^+ regions approach each other (further study is necessary to fully explain this mechanism and clarify the behavior quantitatively).

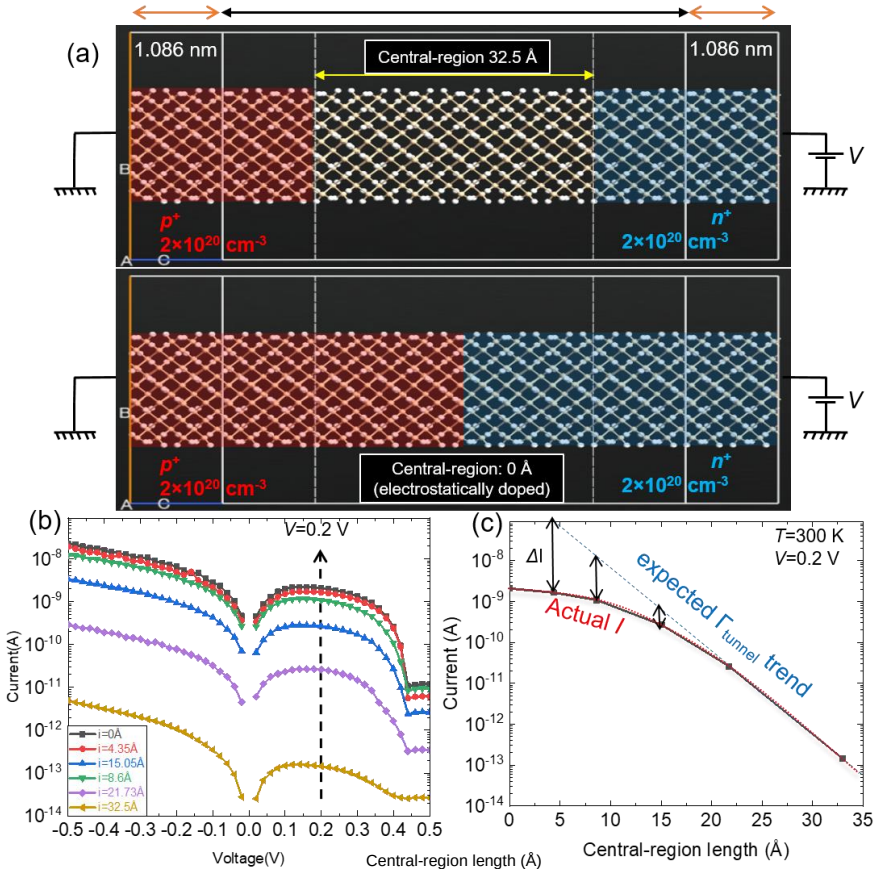

Fig. 4.5 (a) Atomistic view of p^+-n^+ diode with electrostatic doping extending inside the central region. (b) *I*-*V* characteristics by varying the undoped-region length, simulated at *T*=300 K. (c) Effect of the undoped-region length (here, labeled as "intrinsic" region, i.e., *i* with different values, estimated based on atomistic distances, as given in the inset) on current levels at *V* = 0.2 V. The difference in current level (Δ*I*) between the expected trend and actual current is also schematically illustrated.

This analysis reveals that expanding the electrostatic doping for reducing the effective central-region length leads to the incremental change in the BTBT current level. As this central-region length decreases, the tunnel-barrier width decreases as

well, in turn increasing the tunneling rate (**Γ**), which is basically the reason for the observed BTBT-current level increase.

4.4. Impacts of donor-acceptor pairs

4.4.1. Basic methodology for discrete doping and analysis

This section is aiming mainly to elucidate the effects of dopants (donor and acceptor) in the depletion-layer for enhancing the electron transport in the p^+-n^+ diode. Conventional impurity atoms, namely Phosphorus (P) as a donor and Boron (B) as an acceptor, are added substitutionally in the central region, as shown in **Fig. 4.6**. The structure is optimized after the introduction of dopants due to the differences in sizes of P- and B-atoms as compared to the Si atoms. Inter-dopant distance is defined with the counter-dopants placed practically symmetrically around the center of the structure, being shifted towards their respective leads, with different inter-dopant distances of: 27.15 Å, 21.72 Å, 16.29 Å, 10.86 Å, 5.43 Å, and marked as #0 to #4 in **Fig. 4.6(a)**. However, the position closest to the leads (which should be labeled, effectively, as #0) is ignored in the analysis, since geometry optimization process when the dopants are so close to the leads raised some challenges that need further study. It should also be mentioned that these first cases have the dopants actually placed on the surface (or sub-surface) of the Si nanowire ("surface-doped"). Therefore, the interpretation of the following results should take into account the fact that the P- and B-atoms are, in some cases, not corresponding to the conventional understanding of dopants in Si (assumed to be surrounded by Si atoms). This implicitly means that the results presented in this first-stage analysis may also be significantly affected by edge effects and hydrogen passivation; further analysis would be necessary to fully clarify the impact of these effects, but for now these results simply allow the monitoring of the trend due to changing of the lateral positions of dopants (i.e., distances to the leads and inter-

dopant distances), even for such extreme cases. A few examples of cases in which P- and B-atoms are introduced closer to the core of the Si nanowire will also be discussed.

I-V characteristics are simulated for all the above cases, first for *T*=300 K. **Figure 4.6(b)** shows *I-V* characteristics compared with no-dopant case as reference.

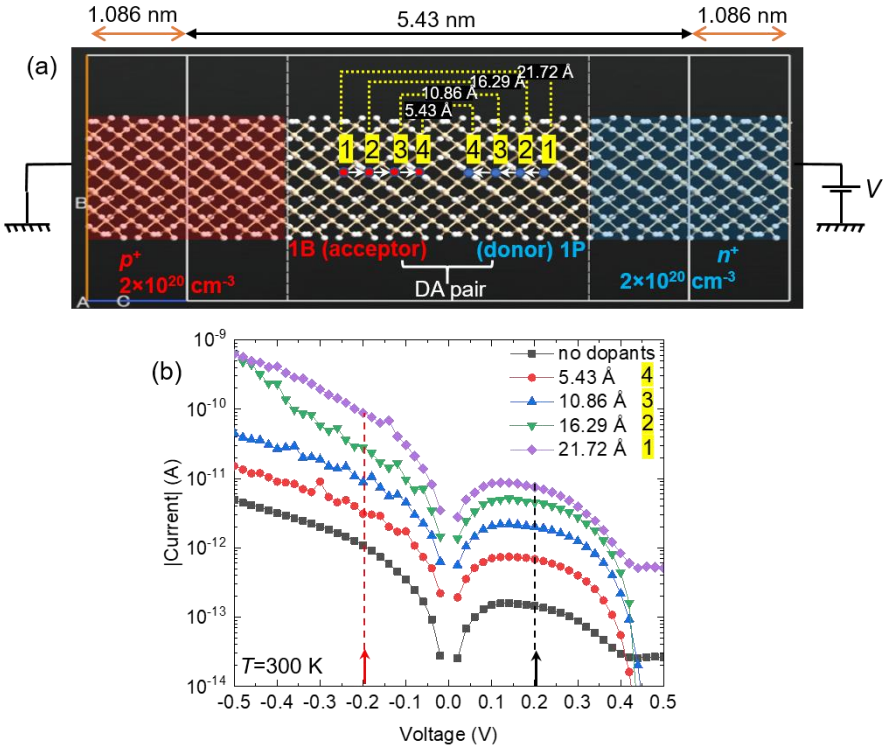

Fig. 4.6 (a) Atomistic view of p^+-n^+ diode with one P-atom and one B-atom added substitutionally as discrete dopants, at different inter-dopant distances (all dangling bonds are passivated with H). In these cases, the P- and B-atoms are placed on the surface (or sub-surface) of the nanowire, as an extreme case. Bias circuit for *I-V* simulations is also shown, with *V* being the bias voltage. (b) *I-V* characteristics with D-A at different positions in reference with no-dopant case, in both forward-bias and reverse-bias regimes, obtained at *T*=300 K.

The main observation from this comparison is that, overall, two orders of magnitude of current enhancement can be observed after the introduction of dopants in the central region, as compared with the no-dopant case. **Figure 4.7(a)** shows the dependence on the distance to the leads, i.e., dopant-lead distance ($d_{\text{D-lead}}$) of the BTBT current measured at V_{bias} = +0.2 V (forward bias) and V_{bias} = -0.2 V (reverse

bias). The absolute value of the current increases with inter-dopant distance ($d_{D\text{-lead}}$) in both regimes (trend indicated by arrow). The factors that may determine this current enhancement can be still quantified by two key parameters, reflecting the physical distances: (i) distance from impurity (dopant) atom to the corresponding lead, termed generally as $d_{D\text{-lead}}$; (ii) inter-dopant distance, that is distance between the P-atom and the B-atom, termed generally as $d_{D\text{-A}}$.

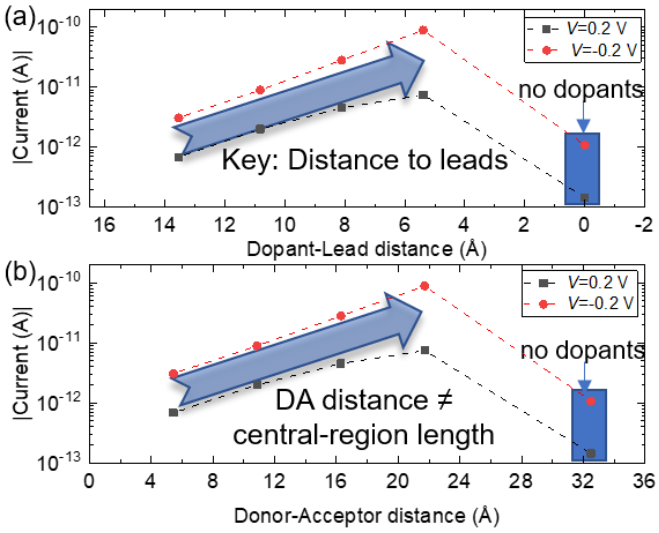

Fig. 4.7 Current evaluated at V_{bias}=0.2 V (forward bias) and V_{bias}=-0.2 V (reverse bias) as a function of: (a) distance to leads, i.e., dopant-lead distance ($d_{D\text{-lead}}$), estimated based on atomistic distances; (b) donor-acceptor distance, i.e., inter-dopant distance (d_{DA}). Arrows indicate the trends as a function of the physical distances.

Figure 4.7(b) shows, thus, the current dependence on the second physical-distance parameter, namely d_{DA}. A systematic current increase is observed also for increasing the D-A distance (and decreasing the distance to leads, simultaneously), revealing the importance of both factors. Further analysis is needed to identify which is the dominant physical-distance factor affecting the current, and this will be explained in the next section.

In order to give a preliminary view into the role of the radial position of the dopants, we provide next, in **Fig. 4.8**, examples of *I-V* characteristics for d_{DA}=16.29 Å, but for two different radial positions: (i) "surface-doping", i.e., a case as treated in most of this chapter, when the P-atom and B-atom are placed on the surface; (ii) "core-doping", i.e., a case which is closer to the conventional image of dopants, with the P- and B-atoms located well within the core of the Si nanowire.

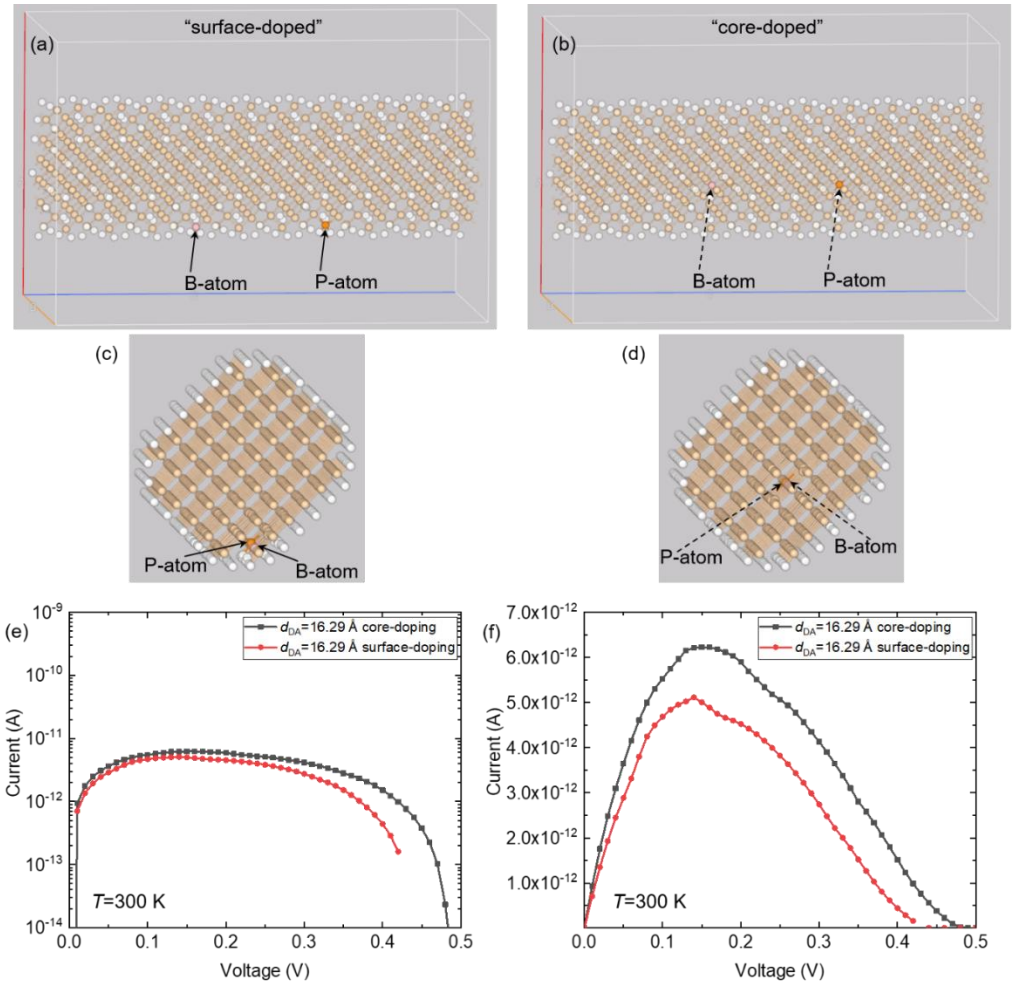

Fig. 4.8 Comparison between extreme cases of Si nanowires built as p^+-n^+ diodes, with different radial placement of the P- and B-atoms, labeled as "surface-doped" (when located on the surface) or "core-doped" (when located in the core of the Si nanowire). (a)-(b) Top views showing the Z-direction of transport for the two cases, with the P- and B-atoms indicated by arrows. (c)-(d) Cross-sectional views, slightly tilted to allow the observation of the atomistic positions of the P- and B-atoms, indicated by arrows. (e)-(f) *I-V* characteristics (at *T*=300 K) are shown in forward-bias regime for comparison, in two different ways for the Current axis: (e) logarithmic scale; (f) linear scale.

These differences are illustrated by comparing the atomistic structures in **Figs. 4.8(a)** and **(b)** for a view along the transport direction (Z), as well as by comparing **Figs. 4.8(c)** and **(d)** for a cross-sectional view of the structure. These structures are slightly rotated to allow the identification of the radial positions of the P-atom and B-atom in the two cases described here, as indicated by arrows. Finally, **Figs. 4.8(e)-(f)** show the *I-V* characteristics simulated at *T*=300 K for these two different cases, with the Current axis shown in logarithmic scale [**(e)**] for easy comparison with **Fig. 4.6(b)** and, respectively, in linear scale [**(f)**] for easy comparison of the current peak shapes between the two cases.

Although only forward-bias regime is simulated here, for simplicity, it is clear that there is only a small difference between the current levels in the two cases, while the current-peak shape is generally preserved. This suggests that, although caution is necessary in interpretation of the physics (especially when the dopants are exactly on the surface of the Si nanowire), it is still reasonable to consider such extreme cases as a baseline for the overall analysis. Future work should, however, focus on two main extended research directions: (i) revising the interpretation based on new results obtained mainly for “core-doped” cases; (ii) analysis of the stability of dopants’ radial positions, since it is well known for Si nanocrystals that near-surface positions are energetically more stable[21] (such study should be extended to the Si nanowires contained in the devices of interest here).

4.4.2. Analysis of physical distances: competitive effects of Donor-Acceptor distance and Donor-Lead distance

So far, it is clear that the dopant positions can greatly influence the BTBT transport, but it is still unclear which is the dominant factor. Due to this reason, the

above analysis is extended further by considering separately the physical-distance parameters: first, the distance to the leads ($d_{D\text{-lead}}$) and, second, the distance between the dopants (d_{DA}).

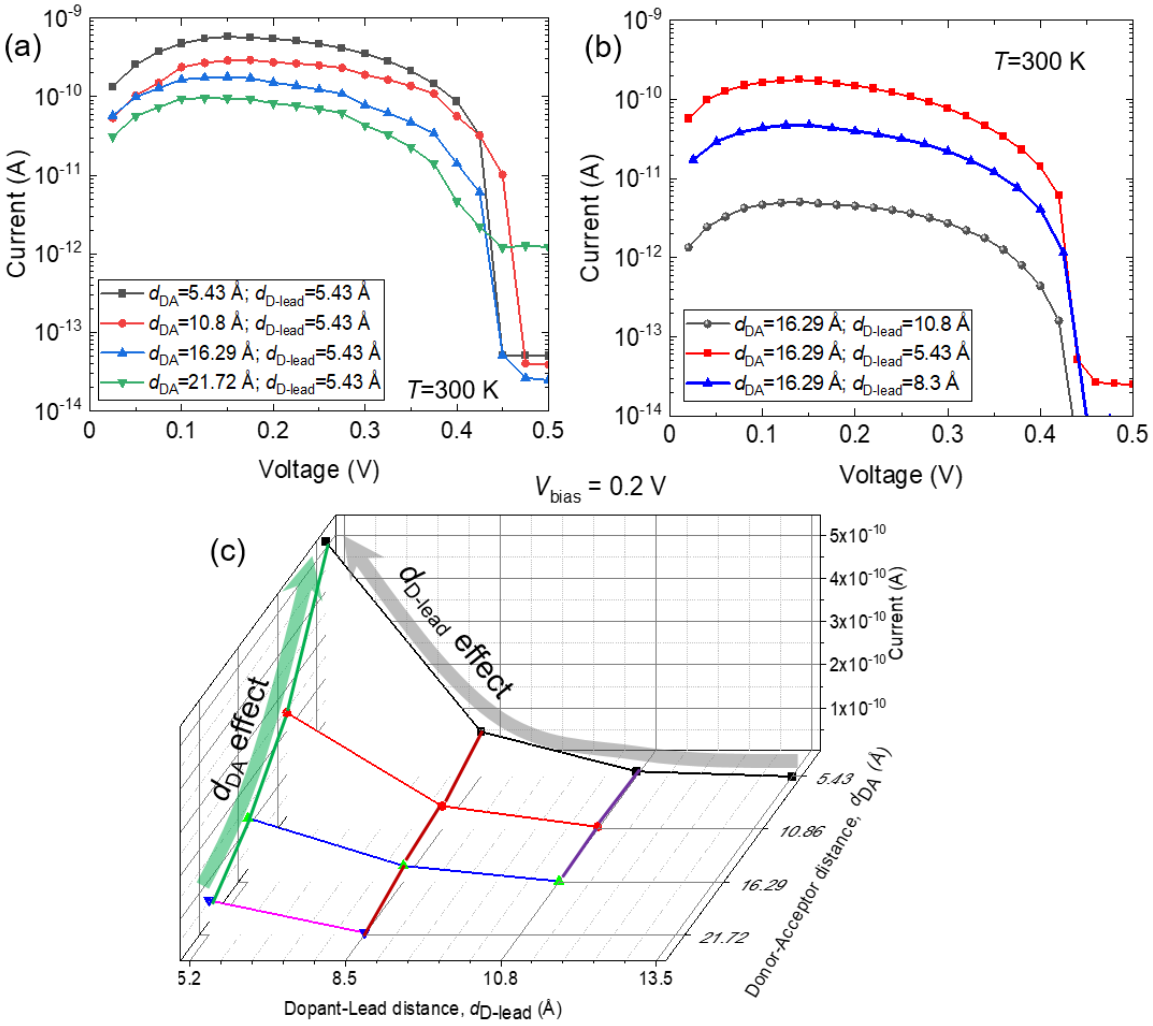

Fig. 4.9 *I-V* characteristics simulated for *T*=300 K, only for the forward-bias region, for two different situations: (a) with distance to lead ($d_{D\text{-lead}}$) kept constant (here, 5.43 Å) while inter-dopant distance (d_{DA}) is varied as a parameter; (b) with inter-dopant distance (d_{DA}) kept constant (here, 16.29 Å) while distance to the lead ($d_{D\text{-lead}}$) is varied as a parameter. (c) Overall representation of the current level at V_{bias}=0.2 V for different cases, showing simultaneously the d_{DA} effect and the $d_{D\text{-lead}}$ effect (with dimensions estimated based on atomistic distances). For all the cases shown here, the distances were changed by expanding the electrostatically-doped region inside the central region and changing also the positions of the discrete P- and B-atoms, according to a specific approach.

To understand these aspects in more detail independently, we created various configurations utilizing both electrostatic doping and discrete dopant positioning in

pairs, by varying one or the other of the parameters (or both together). In this section, the P-atom and B-atom are still positioned on the surface of the Si nanowire (as described earlier and labeled “surface-doped”), remaining that a similar analysis will be applied also for the cases when the P-atom and B-atom are positioned closer to the core of the Si nanowire (as comparatively explained in the previous section and labeled as “core-doped”).

First, we consider dopant-to-lead distance ($d_{\text{D-lead}}$) fixed (here, at 5.43 Å), and the donor-acceptor distance (d_{DA}) as a varying parameter, which means that leads together with the front-side P-atom and, respectively, B-atom were moved towards each other. The results of several cases are shown by the *I-V* characteristics simulated at *T*=300 K in forward-bias regime in **Fig. 4.9(a)**. It can be clearly seen that, as the inter-dopant distance (d_{DA}) (and, at the same time, as distance between leads) decreases, the current increases. This is consistent with the expectation that the tunnel barrier decreases, as well. It should be noted that, by changing the distance to leads ($d_{\text{D-lead}}$), as well, the current can be further modulated (results not shown here).

Second, we consider the donor-acceptor distance (d_{DA}) fixed (here, at 16.29 Å), and the dopant-to-lead distance ($d_{\text{D-lead}}$) as varying. The coupling to the leads is increased by extending the volume of the electrostatically-doped region toward the discrete dopants. *I-V* characteristics simulated at *T*=300 K for several such cases are shown in **Fig. 4.9(b)**. As $d_{\text{D-lead}}$ is reduced, a significant increase of the current level can be observed, with almost two orders of magnitude between the extreme cases. This suggests that d_{D}-lead is a critical parameter in defining the BTBT-current level.

Figure 4.9(c) shows the comparison of current levels (at V_{bias}=0.2 V, *T*=300 K) extracted from the simulated *I-V* characteristics for different cases with a single P-B

pair (here, with the P-atom and B-atom still placed on the surface of the nanowire). This overall view shows distinctly the effects of $d_{D\text{-lead}}$ and d_{DA} on the BTBT current, starting with low currents when both inter-dopant distance and distance to the leads are large, i.e., when coupling is relatively weak, and increasing significantly when either inter-dopant distance or distance to the leads are reduced, i.e., when coupling becomes stronger. As schematically illustrated in **Fig. 4.9(c)**, however, one can predict a stronger relative effect due to the physical-distance between the P-atom/B-atom and their respective leads ($d_{D\text{-lead}}$).

In order to confirm this trend for "core-doped" Si nanowires, several cases were simulated for configurations in which the P-donor and B-acceptor are placed closer to the core. **Figure 4.10** shows two such cases simulated at T=300 K, when the inter-dopant distance is d_{DA}=5.43 Å and, respectively, 16.29 Å, with the regular lead edges and also with the lead-edges extended (on average) 5 Å, towards the dopants in the central region.

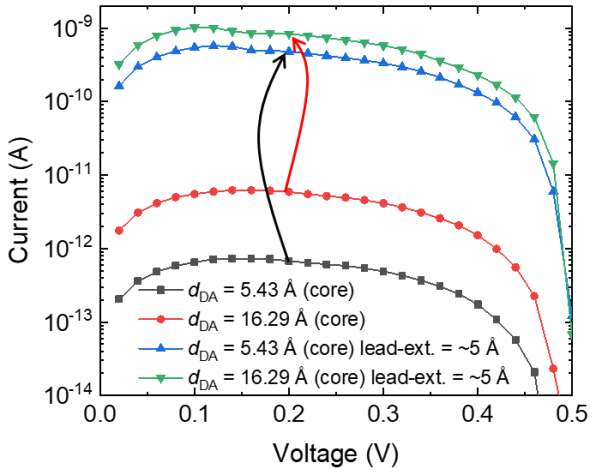

Fig. 4.10 *I-V* characteristics simulated for T=300 K, only for the forward-bias region, for two different configurations for a DA pair with dopants placed near the core of the Si nanowire ("core-doped") at different inter-dopant distances (d_{DA}) of 5.43 Å and 16.29 Å, with regular lead edges (bottom two curves) and with lead edges extended by (on average) 5 Å towards the dopants (equivalent with reducing $d_{D\text{-lead}}$ values. Current increases significantly, as indicated by the arrows.

This result shows the current level is still higher when the dopants are more distanced from each other (and, implicitly, closer to the leads). Furthermore, by extending the (electrostatically-doped) leads towards the DA pair, the current is increased significantly (by several orders of magnitude), as indicated by the arrows. This extension is equivalent to decreasing the $d_{\text{D-lead}}$ for each case, thus supporting the conclusions obtained from the "surface-doped" configurations. More analysis is needed, however, to complete the picture of the behavior of "core-doped" nanowires and it remains as future work.

This suggests that coupling to the leads can be considered as the most critical factor in enhancing the BTBT, while inter-dopant coupling can be treated as a secondary critical factor. This interpretation will be further illustrated in a later section.

4.4.3. Coupling through discrete dopants

The main purpose of this study is to understand the role and importance of front-side dopants in the central region. In that sense, it is an important topic to evaluate the effect of the back-coupling to the leads through an additional dopant (one B-atom toward the p^+ lead and one P-atom toward the n^+ lead). This analysis should be further extended for full clarification of the equivalence between the so-called "electrostatic doping" and "discrete-dopant doping"; however, at this stage, we only show one example (for the "surface-doped" structures), in which one more B-atom (respectively, P-atom) is interpolated between the existing one and its corresponding lead, midway. In this case, we consider the initial D-A pair with the smallest inter-dopant distance (d_{DA}=5.43 Å), and effectively another D-A pair at larger inter-dopant distance (d_{DA}=16.29 Å). **Figure 4.11** shows how the combined structure (containing

both D-A pairs) compares with the individual structures (containing one or the other of the D-A pairs), by comparing the forward-bias *I-V* characteristics simulated at *T*=300 K. Intuitively, it would be expected that the current level is close to that of the structure with a D-A pair distanced at d_{DA}=16.29 Å, since the D-A pair distanced at d_{DA}=5.43 Å could be expected to be strongly compensated. However, the current level of the structure containing both D-A pairs is significantly higher (by approximately one order of magnitude) than each of the individual-pair cases. This reinforces the importance of coupling to the leads, realized in this situation by adding one more D-A pair in the system (i.e., by back-coupling through discrete dopants).

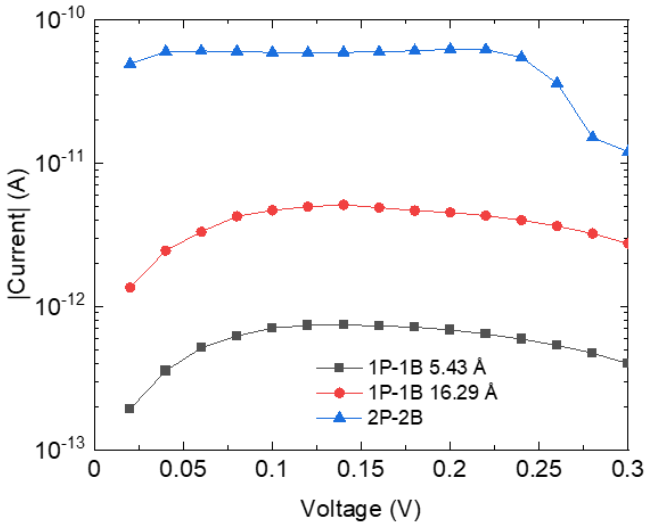

Fig. 4.11 *I-V* characteristics at forward bias for a system with a 2B-2P configuration (containing two D-A pairs), in comparison with single-dopant-pair (individual) cases with different inter-dopant distances (d_{DA}), 5.43 Å and 16.29 Å, simulated at *T*=300 K.

Following this preliminary analysis, this study should be continued more systematically in order to reveal the actual impact of the discrete-dopant coupling as compared to the electrostatic-doping extension and, thus, provide additional points of consideration for our overall analysis.

4.4.4. Low-temperature analysis of *I-V* characteristics

For a deeper understanding of the role of discrete energy states in BTBT transport, it is useful to simulate the low-temperature *I-V* characteristics. Here, low temperature is typically considered as T=8.0 K, consistent with typical temperatures of *I-V* measurements for several experimental devices (to be shown by several examples in **Chapter 5**). Low temperature has the role of making the Fermi-Dirac distribution of carriers (especially in the leads) narrower. As preliminary results, we present the forward-bias *I-V* characteristics under such conditions in **Fig. 4.12**, for structures containing "no dopants" or for "surface-doped" structures containing a D-A pair with P-atom and B-atom located on the surface (or sub-surface) of the Si nanowire. This study should be extended to cases of "core-doped" Si nanowire for full confirmation, and further tuning of the simulation parameters remains as a topic of additional investigation. It should also be mentioned that simulations at even lower temperatures are possible and could reveal finer structures in the *I-V* characteristics, especially when first- and second-derivatives would also be applied to the analysis.

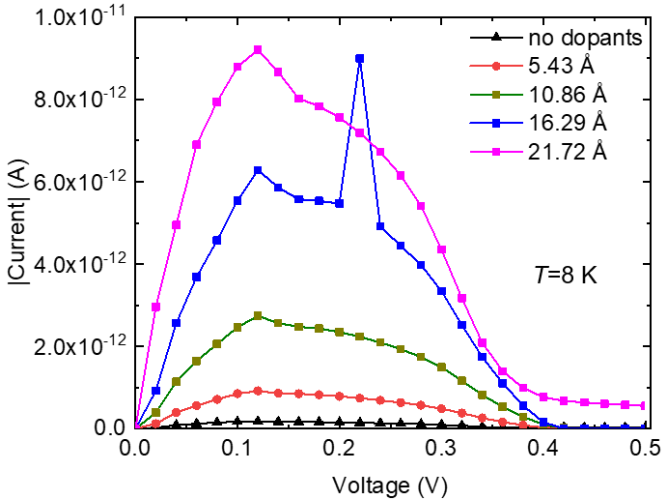

Fig. 4.12 *I-V* characteristics with D-A at different positions, in reference with no-dopant case, for the forward-bias regime. Temperature for the simulations is considered: T=8.0 K.

From these *I-V* characteristics simulated at *T*=8 K, it can be observed that the general trend seen at *T*=300 K (**Fig. 4.6**) is maintained, with the no-dopant case giving the lowest current level in these forward-bias simulations. Oppositely, the highest current level is obtained for the D-A pair distanced at d_{DA}=21.72 Å (largest distance analyzed here). On the other hand, the overall current level is different and fine feature can be identified more readily at such low temperatures.

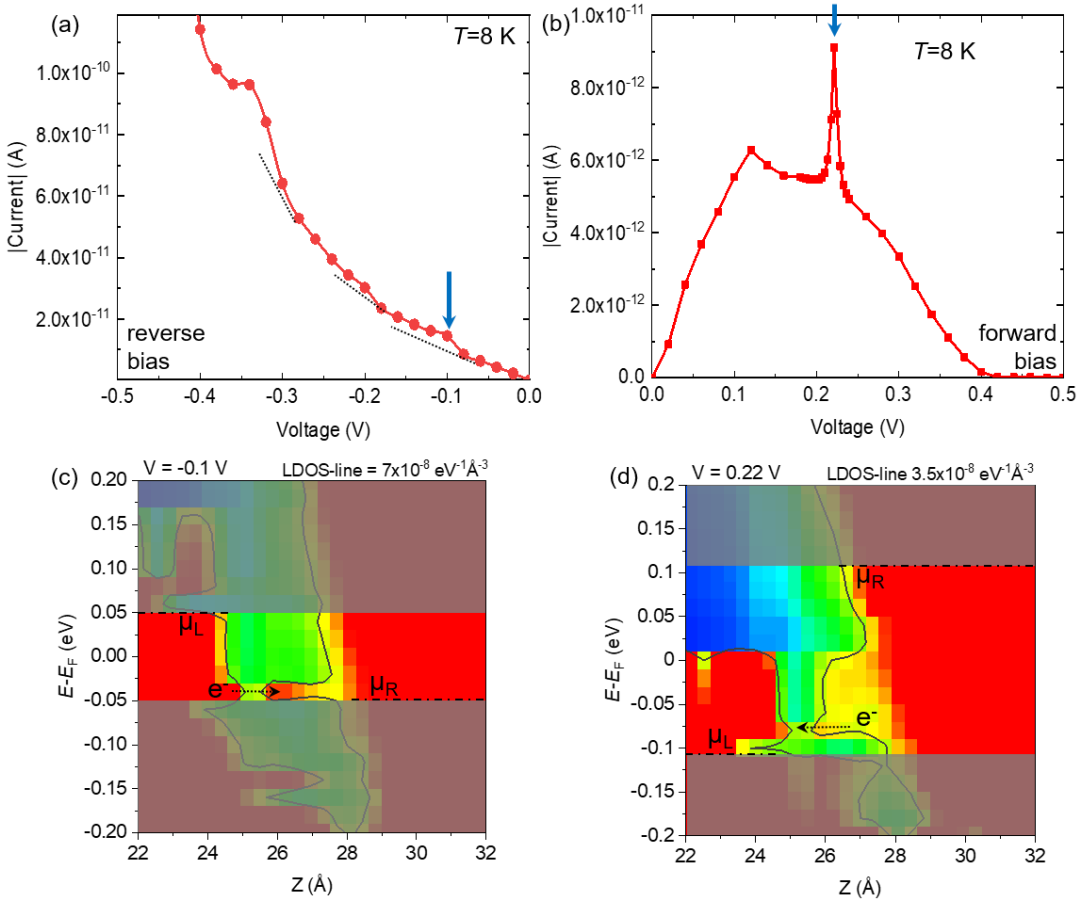

Fig. 4.13 (a)-(b) *I-V* characteristics simulated for a case with a 1P-1B pair at a inter-dopant distance of 16.29 Å, in reverse-bias regime (a) and forward-bias regime (b). Peaks and steps of current are indicated by arrows. (c)-(d) Local Density of States (LDOS) spectra for V_{bias}=-0.1 V (near the first step) in (c) and, respectively, for V_{bias}=0.22 V (at the position of the sharply-enhanced peak) in (d). Energy sampling for the LDOS spectra is 20 meV in these graphs, while finer resolution is used for the *I-V* characteristics.

One most impressive feature, which still requires further detailed analysis for confirmation, is the sharply-enhanced current peak observed for the D-A pair distanced at d_{DA}=16.29 Å, as seen around V_{bias}=0.22 V. In order to further understand the origin of this peak, for 16.29 Å and T=8 K, additional simulations are carried out for more data point and fine current inflections are observed, as marked by arrows for both reverse- and forward-bias conditions, as shown in **Figs. 4.13(a)** and **(b)**.

In the forward-bias regime, two peaks (to be called P_1 and P_2) are observed. Peak P_1 is observed in all the D-A cases, and can likely be interpreted as V_P (peak of NDC), while Peak P_2 may have a different origin; especially around the peak, finer steps are simulated, as shown in **Fig. 4.13(b)** (limited only by the restrictions on the computational time). The occurrence of the fine current features and mainly this peak (P_2) at this particular position can be interpreted further by monitoring the corresponding Local Density of States (LDOS) spectra, as shown in **Fig. 4.13(c)** at V_{bias}=-0.1 V and **Fig. 4.13(d)** at V_{bias}=0.22 V.

The main reason for the observation of the current features seems to be that tunneling is occurring via energy states (gap states), but not necessarily through “true” dopant states. As a speculation at present, the origin of the band-edge tail extending into the bandgap (reminding of the Franz-Keldysh effect)[22,23] may be likely enhanced by the electric field induced by the dopants themselves. These states are tuned by applied bias between 0.18 V and 0.23 V. In the forward-bias regime, at V_{bias}=0.22 V, the energy-state tail is extending inside band gap at the energy $E-E_F$=-0.08 eV. The band-edge tail is within the transport window, marked as shown in **Fig. 4.13(d)**, illustrating how the expansion inside the bandgap may be responsible for the observation of the sharply-enhanced current peak. In the reverse-bias regime, at V_{bias}=-0.1 V, the expansion inside the bandgap occurs at the energy $E-E_F$=-0.04 eV.

Band edge tail seen within the transport window is marked as shown in **Fig. 4.13(d)**, illustrating how the spatial expansion inside the bandgap may be responsible for the fine current step (feature).

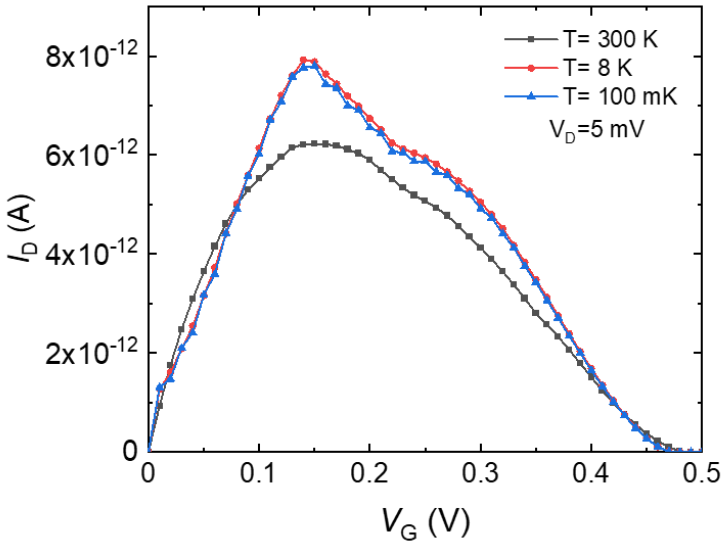

Fig. 4.14 *I-V* characteristics simulated for a case with a 1P-1B pair at a inter-dopant distance of 16.29 Å for core doped configuration in the forward-bias regime. Temperature for the simulation is at *T*= 300 K, 8 K and 100 mK with energy spacing ΔE = 2meV. Finer structures can be observed at lower temperatures.

Temperature dependence of I_D- V_G characteristics (from room temperature to low temperature, 8 K and as a test for cryogenic temperatures – 100 mK) is shown for 1B-1P pair at an inter- dopant distance of 16.29 Å for core doped configuration in **Fig. 4.14**, with the fine energy resolution of ΔE = 2 meV, suggesting finer structures can be observed.

The above results require more in-depth analysis and confirmation of the parameter settings before allowing a conclusive interpretation. This work is currently

under way and will be developed into a part of future analysis for understanding the physics responsible fundamentally for the BTBT-current enhancement.

4.4.5 Interpretation of the key factors for BTBT current enhancement

The results presented in the previous sub-sections suggest the impact of the key physical-distance factors ($d_{\text{D-lead}}$ and d_{DA}), despite the fact that most of the data comes from so-called “surface-doped” structures. As mentioned earlier, this study should be systematically expanded to focus on sub-surface positions of the dopants (reported in the literature to be more stable in terms of formation energy[21]). Another extreme case corresponds to “core-doped” structures, in which the D-A pair is positioned, as much as possible, closest to the central axis of the Si nanowire. In such situation, it is more reasonable to expect that the electron (and hole) wave functions expand around the dopant, with the spatial extension roughly defined by the Bohr radius, r_{B} (known to be approximately 2.5 nm in bulk Si, but strongly downscaled when the dopants are incorporated into nanostructures, even to values <1.0 nm).[24] It should be noted, however, that the precise spatial extension has a specific distribution, enhanced along the <110> directions as compared to the <100> direction, as described in details in Ref. [19]. This should be considered in future analyses for an accurate description of inter-dopant coupling and dopant-lead coupling. Nevertheless, for the simplicity of explanation here, a circular extension around the dopant is chosen.

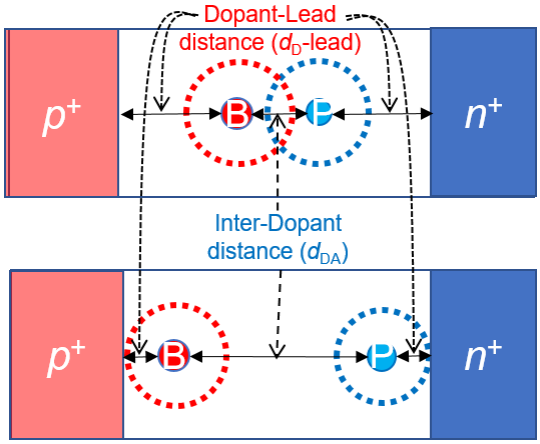

Fig. 4.15 Schematic illustrations of leads and dopants (with dashed circles indicating roughly the ground-state expansion of the wave function for a downscaled Bohr radius, r_B), as a function of two physical distances: dopant-lead distance ($d_{D\text{-lead}}$) and inter-dopant distance (d_{DA}) for two different cases: (a) when dopants are close to each other, but farther from the leads; (b) when dopants are closer to the leads, but farther from each other. It should be noted that the ground-state expansion is not circular, but enhanced along the <110> directions as compared to <100> direction (as reported in ref. [19]), which is an important point to consider in future analysis. Here, circular representation is chosen for simplicity.

Considering the descriptions given above, and the preliminary data obtained so far, we present a tentative model (schematics) that can help to gain a deeper understanding (interpretation) of the meaning of the factors involved and their impact.

First of all, we provide the schematic interpretation of the physical distances of interest in **Fig. 4.15**, in which two different cases are shown for a D-A pair placed between p^+ and n^+ leads (close to each other, on top, and farther from each other, on bottom). The above description is given in terms of inter-dopant distance (d_{DA}), as marked between the dopants. However, it should be noted that the dopant-lead distance ($d_{D\text{-lead}}$) changes also and has a most critical effect on the BTBT current. This is likely because of the wave function coupling between the front-side dopants and the leads, as illustrated in the bottom case, which would allow the enhanced penetration

of the carrier wave functions towards the center of the structure, effectively enhancing the BTBT probability.

If the D-A pair is placed as “core-doped”, we can extend the results preliminarily obtained for “surface-doped” structures and shown in **Figs. 4.9(a)** and **(b)**. In such a case, the interpretation of the separate effects of “inter-dopant coupling” and, respectively, “dopant-lead coupling” can be illustrated as shown in **Figs. 4.16(a)** and **(b)**, respectively.

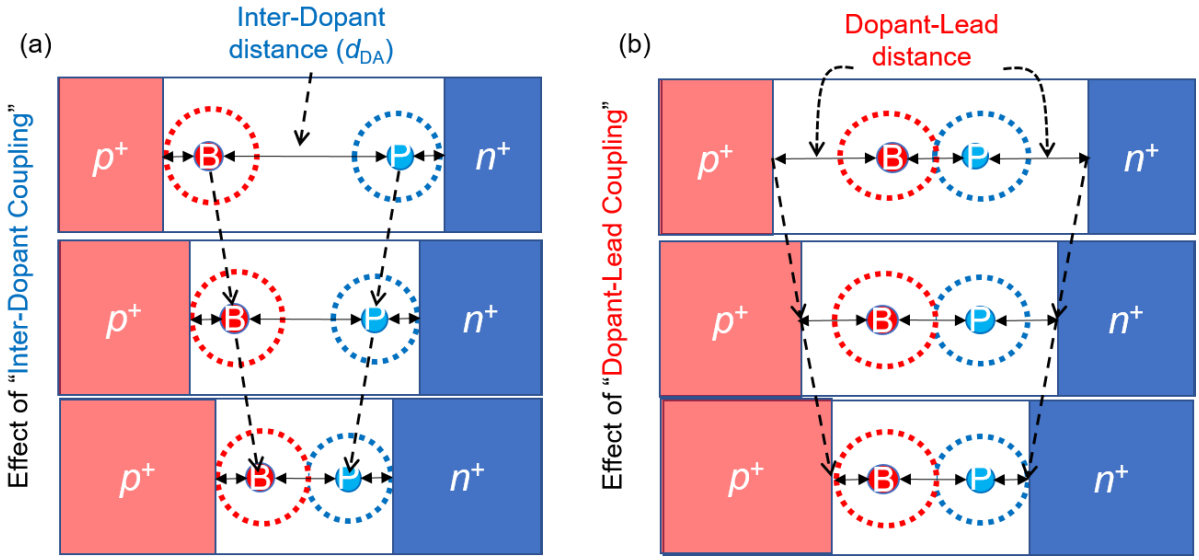

Fig. 4.16 Schematic illustrations of the separate effects of: (a) “inter-dopant coupling”, represented basically by the inter-dopant distance (d_{DA}) – the electrostatically-doped leads can be shifted together with the front-side dopants toward each other, as indicated by arrows; (b) “dopant-lead coupling”, represented by the dopant-lead distance ($d_{D\text{-}lead}$) – the D-A pair is fixed around the center of the structure and the electrostatically-doped leads are gradually shifted towards it in this case. Dashed circles indicate roughly the ground-state expansion of the wave function for a downscaled Bohr radius, r_B (to be noted that the actual spatial expansion is not circular, in reality).

From **Fig. 4.16(a)**, it can be understood how the reduction of the inter-dopant distance (while keeping the front-side dopants pinned to their corresponding lead) can effectively reduce the tunnel-barrier width. This would be valid, however, only if the

"dopant-lead coupling" is sufficiently strong (i.e., when a large overlap of carrier wave functions exists). Otherwise, the front-side dopants would be significantly affected by the built-in electric field present in the device. Similarly, from **Fig. 4.16(b)**, it can be understood that, once the D-A pair is fixed at a certain inter-dopant distance, the "dopant-lead coupling" can be enhanced by expanding the electrostatically-doped leads towards this D-A pair gradually. These schematics illustrate, in short, the competitive effects of "inter-dopant coupling" and "dopant-lead coupling", which represent the two most critical physical-distance factors in the enhancement of the BTBT current.

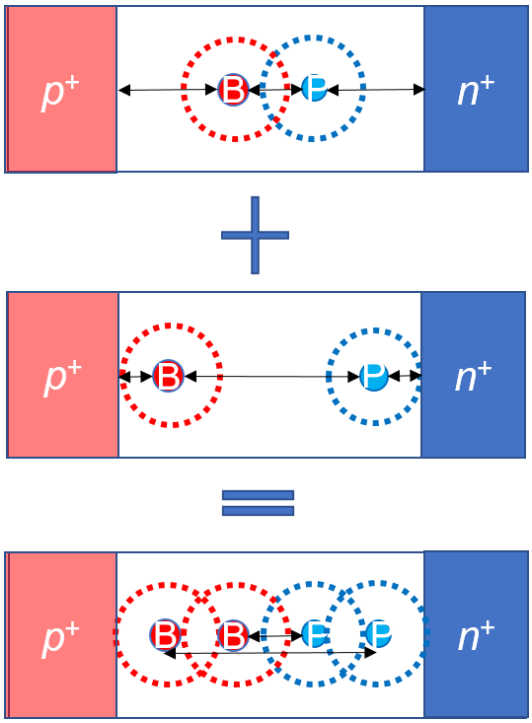

Fig. 4.17 Conceptual illustration of the introduction of two D-A pairs (with individual cases shown in the top two panels) into a resultant double-pair structure (lower panel). These schematics reflect the enhanced coupling of the front-side dopants to the leads by interpolation of a back-side D-A pair. Circular spatial expansions of the wave functions are chosen here only for simplicity of the explanation, but they do not accurately reflect the reality.

Finally, this interpretation should be further supported by "core-doped" results obtained by comparing single-D-A-pair cases with double-D-A-pair cases, in which the

front-side D-A pair is coupled more strongly to the leads by the incorporation of another D-A pair, midway between the front-side dopants and the leads. This is conceptually illustrated in **Fig. 4.17** (and can be applied to "core-doped" cases following the preliminary results obtained for "surface-doped" cases, as shown in **Fig. 4.11**).

It should be noted, however, that the physical distances do not precisely and completely reflect the couplings in such systems, unless energy-alignment considerations are also included in the interpretation of the transport mechanisms. For a conceptual illustration of this point, **Fig. 4.18** shows schematically the energy band diagrams for p^+-n^+ diodes with a D-A pair at different positions in the depletion layer.

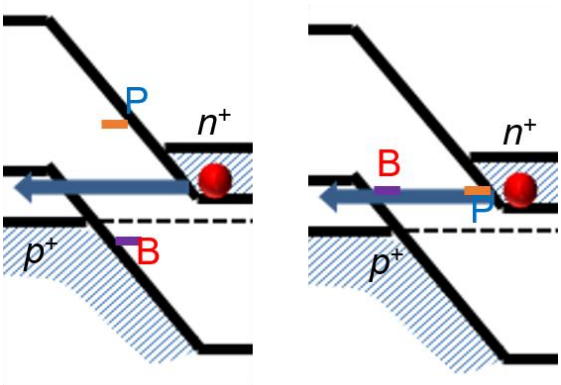

Fig. 4.18 Conceptual illustration of energy band diagrams for two cases of p^+-n^+ diode containing D-A pairs with different physical-distance configurations. This shows the difference in energy between the states and the different bias regimes needed to access such energy states in alignment within the transport window.

Ignoring tentatively the coupling to the leads, simply drawing the donor- and acceptor-induced energy states on the depletion-layer band diagrams suggests that, for D-A pair with small inter-dopant distance (left), the energy gap between the states is large, while this is opposite for the D-A pair with larger inter-dopant distance (right). As such, different bias regimes will be needed to align these energy states inside the transport window. Further consideration of this point is necessary in order to provide

a more complete picture of the factors influencing the BTBT transport in such atomistically-doped devices. At present, it can be stated that the overall BTBT current enhancement can be ascribed to the wave function spread (expansion) towards the leads, between the dopants, as well as to energy-state alignment, resulting in a (still) complex combination of inter-related factors.

4.5. Crystalline orientation effect

An important aspect of Si nanowires for practical applications is their crystalline orientation (as well as the D-A pair orientation within the nanowire). In all the results shown in this chapter, the orientation of the Si nanowire was <100>, which allows a simple first-stage interpretation of the key factors. However, a more practical crystalline orientation for comparison with experimental devices is the <110> orientation. It can be expected that the key factors identified for the <100> orientation can also be identified for the <110> orientation, at least regarding the BTBT current enhancement. Nevertheless, it is also expected that the wave function expansions are different for the two orientations (in fact, likely enhanced for <110> orientation).[19]

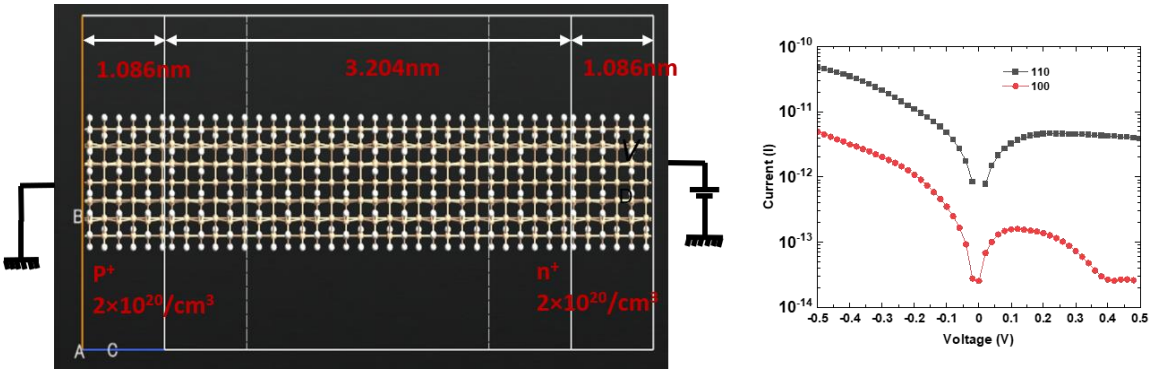

Fig. 4.19 Left: Atomistic view of the Si-nanowire with <110> orientation embedded in a p^+-n^+ diodes (with electrostatically doped leads, as analyzed so far for <100> cases). Right: Simulated *I*-*V* characteristics at *T*=300 K for both orientations of interest. An increase of at least one order of magnitude is observed for the case of <110> orientation.

Figure 4.19 shows first (left) the atomistic structure for a <110>-oriented Si nanowire p^+-n^+ diode, with doping concentrations and dimensions consistent with the <100>-oriented cases described so far. As a preliminary analysis, these cases (without discrete dopants) are compared in terms of *I*-*V* characteristics simulated at *T*=300 K.

Overall, in both reverse-bias and forward-bias regimes, current enhancement by one order of magnitude or more can be observed for the <110>-oriented Si nanowire device. This preliminary result clearly suggests the importance of crystalline orientation for future analyses, which remains as future work based on the background results described in this chapter. In addition, the specific orientation of the D-A pairs relative to the axis of the Si nanowires (not shown here) can also provide information about the wave function coupling and remains as another future work to extend the present analysis.

4.6. Conclusion

In this Chapter, nanoscale p^+-n^+ diodes with highly-doped leads have been investigated as a function of distance between the (electrostatically-doped) leads, but most importantly as a function of the configurations of donor-acceptor pairs (D-A pairs), discretely doped in the central region of the device. The radial positions of the P- and B-atoms are also important and should be further systematically analyzed; a large part of the results presented in this chapter are from structures in which P- and B-atoms are positioned on the surface of the Si nanowire as an extreme case. Even under such conditions, however, from a comparative analysis, the role of D-A pairs in band-to-band tunneling (BTBT) current could be systematically observed. The analysis is

mainly based on results obtained at room temperature (T=300 K), only including preliminary results at lower temperature (T=8 K) for now, to be extended as future work.

It should be noted that this analysis had the purpose of revealing the role of the front-side dopants (corresponding to the most advanced dopants inside the depletion-layer of nanoscale p^+-n^+ diodes, in experimental devices).It was found that there are three main factors that dictate the BTBT current level in such devices.

First and most dominantly, the current level is controlled by the coupling between the front-side dopant and the corresponding lead edge; this is likely realized by an extension of the carrier wave function (on the order of a reduced Bohr radius in such downscaled devices) resulting in enhanced coupling as the dopants are shifted closer to the leads. Such coupling can be realized also by placing another dopant behind the front-side dopant, but the effect of this coupling has to take into account the extra expansion of the carrier wavefunctions in such quasi-“molecular” states.

Second, it was demonstrated that inter-dopant distance also plays a key role, representing the coupling between the front-side donor and the front-side acceptor (likely involving the electron-hole wave function extension). When this is considered also within the high electric field and possible alignment of donor and acceptor states by forward (or reverse) bias, such inter-dopant coupling can lead to prominent enhancement of the BTBT current. Third, such D-A pairs can contribute to BTBT current if energy-state alignment can be achieved, in different bias regimes depending on the D-A pair configuration.

Finally, an important role may be ascribed to the crystalline orientation of the Si nanowire. Further study is needed, however, to clarify this effect by a more systematic

analysis. It should be noted that this study is important in order to bridge the gap to the experimental devices, for which crystalline orientation is critical. Several such experimental examples will be presented in the next Chapter.

References

[1]L. Esaki, Phys. Rev. **109**, 603 (1958).

[2]L. Esaki and Y. Miyahara, Solid State Electron. **1**, 13 (1960).

[3]A. G. Chynoweth, R.A. Logan, and D.E. Thomas, Phys. Rev. **125**, 877 (1962).

[4]A. G. Chynoweth, W.L. Feldmann, and R.A. Logan, Phys. Rev. **121**, 684 (1961).

[5]N. Holonyak, I. A. Lesk, R. N. Hall, J. J. Tiemann, and H. Ehrenreich, Phys. Rev. **3**, 167 (1959).

[6]M. Oehme, D. Hähnel, J. Werner, M. Kaschel, O. Kirfel, E. Kasper, and J. Schulze, Appl. Phys. Lett. **95**, 242109 (2009).

[7]M. Oehme, O. Kirfel, J. Werner, M. Kaschel, E. Kasper, and J. Schulze, Thin Solid Films **518**, S65 (2010).

[8]H. Schmid, C. Bessire, M.T. Björk, A. Schenk, and H. Riel, Nano Lett. **12**, 699 (2012).

[9]M. Tabe, H.N. Tan, T. Mizuno, M. Muruganathan, L.T. Anh, H. Mizuta, R. Nuryadi, and D. Moraru, Appl. Phys. Lett. **108**, 093502 (2016).

[10]G. Prabhudesai, M. Muruganathan, L. T. Anh, H. Mizuta, M. Hori, Y. Ono, M. Tabe, and D. Moraru, Appl. Phys. Lett. **114**, 243502 (2019).

[11]J.-B. Xia and K. W. Cheah, Phys. Rev. B **56**, 14925 (1997).

[12]S. Saito, D. Hisamoto, H. Shimizu, H. Hamamura, R. Tsuchiya, Y. Matsui, T. Mine, T. Arai, N. Sugii, K. Torii, S. Kimura, and T. Onai, Jpn. J. Appl. Phys., **45**, L679 (2006).

[13]N. Moulin, M. Amara, F. Mandorlo, and M. Lemiti, J. Appl. Phys. **126**, 033105 (2019).

[14]R. Nowak, D. Moraru, T. Mizuno, R. Jablonski, and M. Tabe, Appl. Phys. Lett. **102**, 083109 (2013).

[15]S. Purwiyanti, R. Nowak, D. Moraru, T. Mizuno, D. Hartanto, R. Jablonski, and M. Tabe, Appl. Phys. Lett. **103**, 243102 (2013).

[16]A. C. Seabaugh and Q. Zhiang, Proc. IEEE **98**, 2095 (2010).

[17]T. Mori, Y. Morita, N. Miyata, S. Migita, K. Fukuda, W. Mizubayashi, M. Masahara, T. Yasuda, and H. Ota, Appl. Phys. Lett. **106**, 083501 (2015).

[18]K. Ono, T. Mori, and S. Moriyama, Sci. Rep. **9**, 32309 (2019).

[19]L. T. Anh, PhD Thesis (Japan Advanced Institute of Science and Technology), 2014: https://dspace.jaist.ac.jp/dspace/handle/10119/12621

[20]D. C. Liu and J. Nocedal, Math. Program. **45**, 503 (1989).

[21]F. Iori, E. Degoli, R. Magri, I. Marri, G. Cantele, D. Ninno, F. Trani, O. Pulci, and S. Ossicini, Phys. Rev. B **76**, 085302 (2007).

[22]Y. Yacoby, Phys. Rev. **142**, 445 (1966).

[23]Y. Hamakawa, T. Nishio, and J. Yamaguchi, J. Phys. Soc. Japan **20**, 1958 (1965).

[24]T.L. Chan, M.L. Tiago, E. Kaxiras, and J.R. Chelikowsky, Nano Lett. **8**, 596 (2008).

Chapter 5: Experimental illustrations of transport via dopants in Si nano-devices

In this Chapter, a few examples of experimental results obtained for silicon-on-insulator (SOI) nanoscale devices will be presented. Such examples illustrate a possible impact of donor- and acceptor-atoms on tunneling transport, either in the case of counter-doped nanoscale transistors, or in the case of highly-doped tunnel diodes with donors and acceptors present in the nanoscale depletion layer.

Such illustrative examples can provide an image of what kind of results can be obtained and utilized from the experimental side, so that some parallel can be drawn with the fundamental results obtained from the theoretical approach, for significantly smaller structures. Considering, however, the differences in dimensions, passivation conditions, gating, and treatment of the leads, it should be emphasized from the beginning that these examples are not supposed to be one-to-one counterparts for the theoretical cases, but rather provide complementary insights that can actually broaden further the field of physics that can be addressed by the main type of structure investigated in this thesis: the counter-doped nanoscale silicon structure embedded as the active part in various electronic devices.

In this Chapter, the first part will be dedicated to describing counter-doped SOI transistors, with a dominant doping with donors. Signatures of tunneling (even single-electron tunneling[1]) via dopant clusters can be identified, in particular at low temperatures. In addition, there are other signatures of charging and discharging that are speculated to be reasonably assigned to the acceptors present in the nanoscale channels of such devices.

The second part will be dedicated to describing basic examples of band-to-band tunneling (BTBT) in nanoscale SOI tunnel (Esaki) diodes,[2] i.e., lateral p^+-n^+ diodes with doping concentrations high enough to shift the Fermi levels on both sides into the respective bands (conduction band for the *n*-side and valence band for the *p*-side). This situation allows not only the formation of a very narrow depletion layer, but implicitly allows the observation of BTBT both in forward and reverse bias conditions. From our experiments on a number of nanoscale tunnel diodes, it was also possible to identify signatures of BTBT mediated by dopant clusters[3] or potentially by donor-acceptor pairs,[4] although further analysis of the experimental results is still necessary.

5.1. Single-electron tunneling via dopant-clusters in high-concentration co-doped Si nano-transistors

5.1.1. Device structure and parameters

In order to investigate the possibilities of counter-doping in nanoscale Si transistors, devices had been fabricated by CMOS-compatible processes (as described in other theses works in details[5,6]). Schematically, the device structure and some details are provided in **Fig. 5.1**.

The basic device structure is that of an SOI-FET (silicon-on-insulator field-effect transistor), as shown in **Fig. 5.1(a)**. The devices were fabricated[5] starting from an SOI wafer, thinned down to a starting thickness of the top-Si layer of about 50 nm. After defining the alignment marks within the substrate Si, these marks are used to align consecutive CAD patterns for the electron-beam lithography stages later on. First, the larger Si pads are defined, with lateral dimensions of 60×60 μm^2, with a narrower region in between the pads that will become source and drain extensions. Second,

doping processes are performed one after another: (i) phosphorus (P) n-type doping (using OCD P-59230), with pre-deposition at 600℃ for 30 min in N_2 atmosphere (1.5 L/min), followed by drive-in at 950℃ for 10 min in N_2 atmosphere (1.5 L/min)); (ii) boron (B) p-type doping (using PBF 6M-10), with pre-deposition at 600℃ for 30 min in O_2 atmosphere (1.5 L/min), followed by drive-in at 900℃ for 5 min in N_2 atmosphere (1.5 L/min). Based on these thermal-diffusion processes, it was estimated from four-point probe measurements that the doping concentrations are: $N_D \approx 2.2\times10^{20}$ cm^{-3} and, respectively, $N_A \approx 6.5\times10^{19}$ cm^{-3}.[5] These concentrations are high enough to make Si degenerately-doped, i.e., to shift the Fermi levels (E_F) inside the respective bands.[7,8]

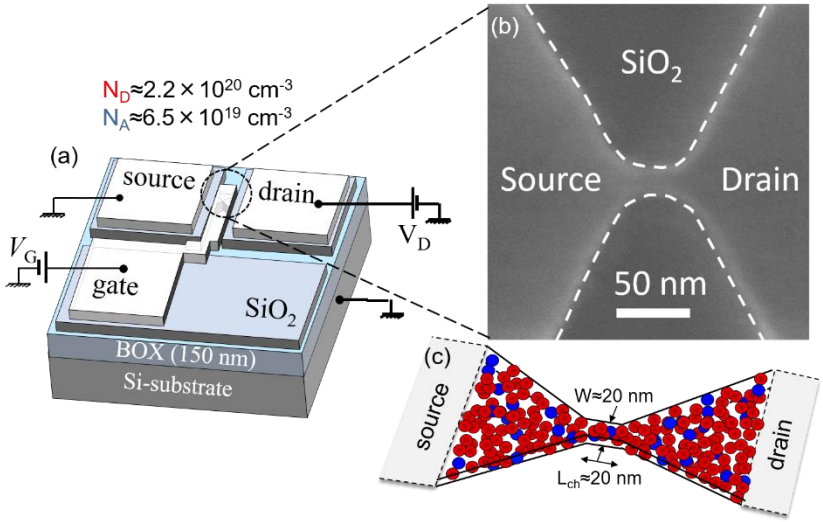

Fig. 5.1 (a) Single SOI-FET structure, showing also the biasing circuit schematically. (b) SEM image of a SOI-channel area for one of the "point-contact" transistors. (c) Illustration of a counter-doped channel (only a fraction of P-donors (red spheres) and B-acceptors (blue spheres) are shown for simplicity).

More importantly for this design, N_D is about 3 times larger than N_A; if we assume a relatively uniform distribution of dopants, this means that there will be one B-acceptor nearby a region containing 3 P-donors. As such, it is a reasonable image to consider that, in extremely low-dimensional channels, the active unit in transport

might be a 3-donor “cluster” flanked by one B-acceptor on each side, as we discussed in the theoretical part. It has to be stressed that such configuration is strongly affected by randomness of dopant positions and numbers, so such a case can only be expected to be formed accidentally and not with a high statistical yield.

As a third main fabrication process, after doping was completed, nanoscale-channel patterning was done by reactive ion etching (RIE). A number of patterns were created and analyzed previously, but here the focus will be on the so-called “point-contact” SOI-FETs. This is followed by a fourth main step of gate oxidation; in this case, thermal oxidation was carried out to create a SiO_2 layer with a thickness of approximately 9±1 nm. A scanning electron microscope (SEM) image of such a transistor at this stage is shown in **Fig. 5.1(b)**;[6] it can be seen that the “point-contact” channel becomes a short nanowire with width and length on the order of ~20 nm, connected to fan-shaped regions that act as source and drain extension-leads. This structure, with a fraction of the dopants also illustrated schematically, is shown **in Fig. 5.1(c)**; it should be noted that the number of dopants is much higher than shown.

The fifth and final step of the fabrication process is the formation of the contact holes (for direct contact between Al electrodes and Si in the source/drain areas) and lift-off process to create the Al electrodes (with a thickness of about 250 nm). These are the structures shown in **Fig. 5.1(a)** schematically.

In order to probe the effects of the dopants in such nanoscale channels, current-voltage (*I*-*V*) characteristics were measured for a large number of devices, with a biasing circuit shown schematically also in **Fig. 5.1(a)**. Typically, measurements were carried out in a high-vacuum chamber of an IV prober system (Nagase Co.) connected to a semiconductor precision parameter analyzer (Keysight); the system is

highly stable mechanically and can access currents with a noise level on the order of 10-100 fA, depending on the conditions. Most importantly, the key measurements were taken at low temperatures (indicated to be ~8 K at the level of the sample stage). Low temperature allows the suppression of thermally activated processes and observation of tunneling events more clearly. Temperature dependence can also be measured for specific purposes.

5.1.2. Observation of single-electron tunneling at low temperature

We pick up for the next discussion several examples of devices that exhibit single-electron tunneling (SET) features at low temperatures (8~15 K). We indicate the design dimensions also, although the final (real) dimensions should be considered based on SEM images as shown in **Fig. 5.1(b)**. It should be noted first that all the devices that were designed to have a channel width of >40 nm exhibit relatively large currents that cannot be controlled by the gate voltage (V_G), which indicates that "metallic" paths are formed in such channels, connecting the highly-doped source and drain directly.[5,6] Nevertheless, among the devices with channel width <~30 nm, we can find examples of SET behavior and we will show these examples below as proof-of-concept data.

Figure 5.2 shows the low-temperature (T=15 K) data obtained for a SOI-FET with a designed width of 30 nm.[9] The range of V_G is extended from slightly positive values to –8 V, being limited by the onset of a small gate leakage current (~100 fA). The measurements were stopped at this limit in order to avoid oxide breakdown. It can be seen that current oscillations (peaks) appear on a decreasing overall current as V_G is made more negative. Such features indicate the possibility of SET transport,

likely through a multiple-donor quantum dot (QD), left uncompensated by the surrounding acceptors. We could also find reproducible sudden jumps of I_D (shown in the inset of **Fig. 5.1(a)**), which can be correlated with charging (and discharging) in some traps near the conduction path. Such traps can be reasonably ascribed to the remaining B-acceptors that can capture electrons from the transport path and consequently modify the electrostatic potential (and implicitly the I_D-V_G characteristics). It cannot be excluded, however, that such traps are P-donors in some more isolated locations in the channel, as reported in other works of the group,[10,11] or even interface traps. Therefore, a conclusive argument on this issue requires further investigation of devices with different ratios of doping concentrations, as well as with different processing by hydrogen annealing (to remove the possibility of interface traps). This remains as a task for future work.

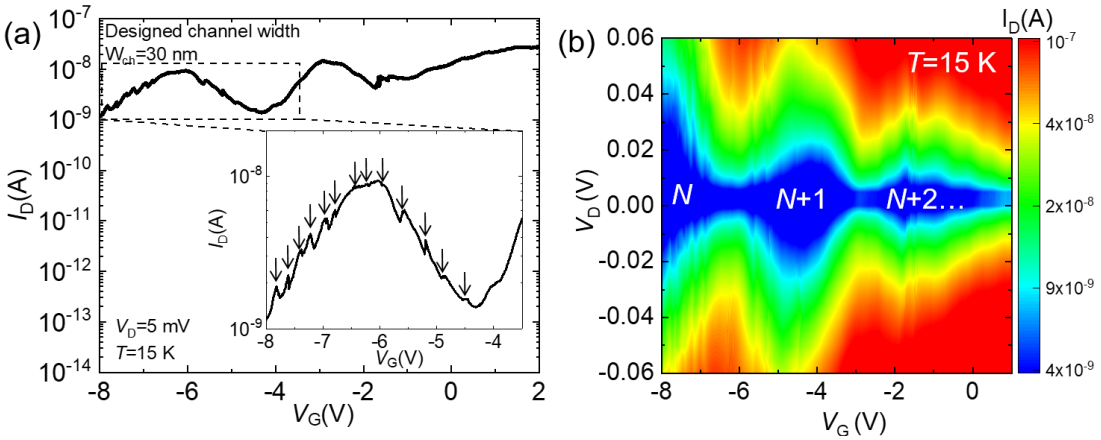

Fig. 5.2 (a) I_D-V_G characteristics measured at T=15 K and V_D=5 mV for a SOI-FET (Device A) with channel designed to be 30 nm in width (point contact). Current oscillations (peaks) are observed, along with sudden jumps of the current (indicated by arrows in the inset). (b) Stability diagram (contour plot of $|I_D|$ in the V_G-V_D space) at T=15 K, showing typical signatures of SET (Coulomb blockade) as "Coulomb diamonds"; these indicate that the number of electrons in a quantum dot increases one by one as V_G is increased.

Another way to observe and analyze further the SET behavior, confirming that it is related to the Coulomb blockade effect, is by measuring the stability diagrams,[1] as shown in **Fig. 5.2(b)**. When $|I_D|$ is plotted in the V_G-V_D space,

diamond-shaped regions of lower current (blue areas) can be noticed, reminding of Coulomb diamonds. In such areas, it is expected that the number of electrons changes one by one by changing V_G across a current-flowing region ($N \rightarrow N+1 \rightarrow \ldots$, with N being the integer indicating the number of electrons existing in the quantum dot (QD) for the most negative V_G that we were able to monitor).[12]

From the period (ΔV_G) between the current peaks (~2.5-3.5 V), and assuming a simple circular cross-section of a QD in a parallel-plate capacitor model (with SiO_2 as an insulator coupling the QD to the gate), one can evaluate the gate capacitance (C_G)[1,12] to be on the order of 0.55±0.1 aF, corresponding to a QD radius of ~1.5-3.0 nm. This value is reasonable considering a model of a "cluster" of several P-donors, strongly coupled at distances on the order of the Bohr radius (r_B≈2.5 nm),[9] and embedded in the nanoscale channel of the transistor.

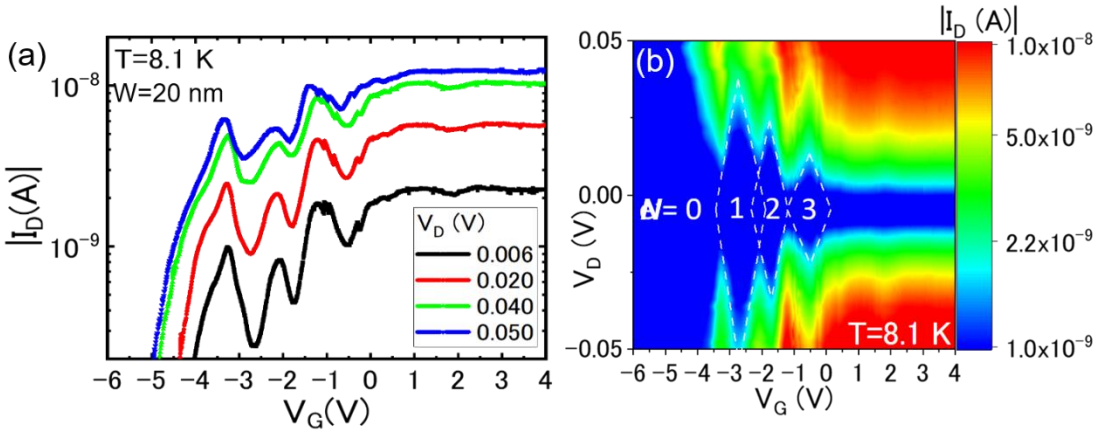

Fig. 5.3 (a) I_D-V_G characteristics measured at T=8.1 K and V_D=6~50 mV for a different SOI-FET (Device B) with channel designed to be 20 nm in width (point contact). Current oscillations (peaks) are observed, with clear reproducibility and increasing levels as V_D is increased. (Some charging features are observed – similar to device A – but in the range of V_G around -1 V ~ +1 V. (b) Stability diagram (contour plot of $|I_D|$ in the V_G-V_D space) at T=8.1 K, with clearer Coulomb diamonds and even an open-region for V_G<~-3.5 V (indicating that we observe a QD likely fully depleted of electrons, i.e., N=0), and addition of electrons one by one as V_G is increased.

Figure 5.3 shows another example for a device with a designed width of 20 nm (labeled as device B),[6] at a low temperature T=8.1 K (as indicated at the sample-stage level). For this device, current peaks are even more clearly observed in **Fig. 5.3(a)** (in particular, three consecutive peaks are easier to notice, with good reproducibility and a dependence on V_D). Although there are some differences between the consecutive peaks, we can tentatively ascribe this kind of behavior to SET via one QD, assuming also that such a QD may accommodate 3 electrons. With such a simple model, it is again reasonable to ascribe such a QD to a few-donor "cluster" remaining in the nanoscale channel of the SOI-FET. (It is worth mentioning that some charging/discharging features can also be observed for this device as current jumps at somewhat higher V_G range, similarly to the case of Device A presented in **Fig. 5.2**.)

In order to confirm the Coulomb blockade effect in such device also, measurements of the stability diagram (also at 8.1 K) are shown in **Fig. 5.3(b)**. This time, one can observe an open region for V_G<~-3.5 V, which may correspond to the situation when all electrons could be depleted from the QD (N=0). This region is followed by regions resembling Coulomb diamonds, which suggests that Coulomb blockade contributes significantly to current, at least at such low temperatures.

Similarly to the analysis for Device A, in this case we can also evaluate the spacing between consecutive peaks, or the period (ΔV_G), to be 1.0±0.1 V. Under a similar model, this corresponds to a radius of the QD of approximately 3.5±0.1 nm. Although slightly larger than the estimation for Device A, the QD identified in Device B can also be reasonably associated with a cluster of several P-donors coupled at distances on the order of r_B.

From the above cases, it can be seen that low-temperature characterization of such nanoscale counter-doped SOI-FETs can reveal, in certain devices, signatures of the presence of QDs: current peaks in I_D-V_G characteristics and Coulomb diamonds in stability diagrams. Considering the extremely high doping concentration of donors ($N_D \approx 2.2\times10^{20}$ cm^{-3}), such formation of an isolated QD by donors is difficult to be expected.[13,14] However, once counter-dopants (B-acceptors) are introduced in the channel, the likelihood of such QD formation increases significantly.[15] Although further evidence is needed to understand clearly the role of the B-acceptors, we obtain also promising features of charging that could be another signature of their active role in transport. The additional analysis, including fabrication of devices with different doping conditions, should be able to reveal more precisely and reliably the role of B-acceptors.

5.1.3. Temperature dependence (room temperature data)

One key remaining question, before even attempting to make a correlation with the theoretical analysis of co-doped nano-transistors, is how these devices behave at room temperature (T=300 K). This is especially important since the mechanism described so far for the experimental cases taken as examples, i.e., single-electron tunneling based on the Coulomb blockade effect,[1,12] is drastically different from the mechanism assigned in the theoretical analysis, i.e., coherent transport through the donor-cluster energy states, modified partly by the presence of B-acceptors.[16]

In order to understand better the situation of the experimental devices, we show in **Fig. 5.4** the I_D-V_G characteristics in a wide V_G range for many devices within one chip, as a function of the designed channel width (shown in the legend).

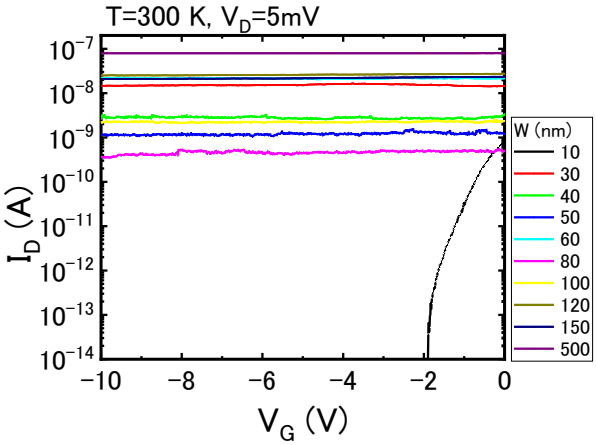

Fig. 5.4 I_D-V_G characteristics measured at T=300 K (room temperature) and V_D=5 mV for different SOI-FETs from a same chip, as a function of designed channel width. Most devices exhibit a “metallic” behavior, except the one with the narrowest channel, which exhibits an FET-like behavior (but with no current peaks or other noticeable features).

Figure 5.4 shows a set of I_D-V_G characteristics measured at T=300 K (denoted as room temperature) and V_D=5 mV.[17] It can be seen that for most devices (smaller or larger designed widths) the behavior is generally “metallic”, i.e., current is high and cannot be controlled significantly by V_G even up to very negative values. This suggests that source and drain are strongly connected by conductive paths that are only sensitive to V_D. Only the narrowest device, in this case, exhibits an FET-like behavior, but without any prominent features, such as current peaks or inflections. This kind of observation was commonly seen in several other chips, with only the narrowest devices exhibiting the FET-like behavior (in most of the cases).

Although the room-temperature behavior does not allow yet a one-to-one comparison with the theoretical analysis, we were able to illustrate that the low dimensionality plays a critical role in the device operation. This is motivating for

pursuing further downscaling and setting the channel width, length and thickness as more critical parameters to tune in the next fabrication processes, in order to achieve devices with all channel dimensions <10 nm.

In addition, it is also important to note that the SET behavior clearly observed at low temperatures changed into a simple FET (or “metallic”) behavior at room temperature, but a transition of transport mechanisms is expected to have occurred at some intermediate temperature.[18] As such, it is also important to evaluate the temperature dependence of the I_D-V_G characteristics in the future in order to identify the transition temperature. At this transition temperature, a more direct correlation between experiments and simulations of such counter-doped nano-transistors can be pursued with better likelihood of gaining further insights.

5.1.4. Guidelines for device design

From the above measurements and preliminary analysis, it can be understood that a single combination of N_D and N_A values cannot provide a clear picture and convincing evidence of the roles of donors and acceptors in transport through such counter-doped nanoscale transistors. Although we observed signatures of SET transport through QDs, governed likely by the Coulomb blockade scheme,[1,12] the origin of the QDs as few-donor “clusters” can only be clarified by changing N_D more systematically.[19,20] Therefore, a first device design guideline is to maintain N_A constant while changing N_D as a parameter, fabricating several samples with different N_D values. If we can identify statistically changes in the nature of the QD, consistently with the changes in N_D, then donor coupling can be considered as an origin of the

QDs. This will also help clarify the role of acceptors, in particular in the compensation of the donors introduced in the channel.

On a different aspect, we noticed the importance of dimensionality on the general transport characteristics. The wider-channel devices invariably exhibit “metallic” behavior even at low temperatures. On the other hand, the narrow-channel devices exhibit (occasionally) FET-like behavior at room temperature and SET behavior at low temperatures. This is a strong hint of the fact that suppression of parallel transport paths is a critical effort for future devices. For that, it is recommended, as another device design guideline, to aim for finer pitch of the channel width in the channel definition lithography step. One can propose a design width between 5-50 nm, with a pitch of 2-5 nm; a part of these devices will eventually end up with the channel completely consumed by the final oxidation step, while another part of these devices will end up with a channel having only several nm in width (channel thickness must also be precisely controlled in the same range). Such device may eventually come closer to the small dimensions that we use in simulations due to computational constraints, and will allow us to close the gap for a more in-depth analysis.

Finally, another device design guideline is to implement selective doping in such nanoscale-channel devices. In the past, selective doping was shown to allow the observation of SET transport via few-donor QDs even at elevated temperatures ($T \approx 150$ K), with some current oscillations preserved even at room temperature.[18] If such selective doping can be complemented by counter-doping, we can attain not only higher SET operation temperature, but we can also reveal the role of acceptors in the definition of the potential landscape in such counter-doped devices more clearly.

5.2. Band-to-band tunneling mediated by dopant atoms in Si nano-diodes

5.2.1. Device structure and parameters

In order to investigate the properties of BTBT transport through co-doped nanostructures, it is most reasonable to choose devices that are designed as tunnel (Esaki) diodes,[2] i.e., highly-doped p^+-n^+ diodes in which the Fermi levels appear into the respective bands (into the conduction band in the *n*-region and into the valence band in the *p*-region).[7] Under these conditions, a narrow depletion layer[8] can be formed which would allow BTBT transport with measurably-high current, both in forward-bias regime (at low voltages) and in reverse-bias regime.

Among the devices available, we selected such p^+-n^+ diodes with a lateral design fabricated in nanoscale structures within SOI wafers. The design and fabrication processes for such SOI p^+-n^+ diodes is described in more details in the respective theses,[21,22] so only a brief outline of the main processes will be described here for completeness.

First, device fabrication starts by preparing SOI wafers with a starting thickness of 50-70 nm (depending on the batch, this is obtained by thinning down the top Si layer by consecutive oxidation and etching processes). This is followed by the formation of alignment marks in the substrate Si (similarly to the case of transistors). These alignment marks will be used for consecutive alignments of various CAD patterns in the subsequent fabrication steps. Second, the Si pads are defined by electron-beam lithography (with the electrode pads having dimensions of 60×60 μm^2), bridged by narrower structures (which will be later used to define the *pn* junction). Third, doping processes are performed as follows: (i) phosphorus (P) n-type doping (using OCD P-59230), with pre-deposition at 600℃ for 30 min in N_2 atmosphere (1.5

L/min), followed by drive-in at 950℃ for 10 min in N_2 atmosphere (1.5 L/min)); (ii) boron (B) p-type doping (using PBF 6M-10), with pre-deposition at 600℃ for 30 min in O_2 atmosphere (1.5 L/min), followed by drive-in at 900℃ for 7 min in N_2 atmosphere (1.5 L/min). Based on these thermal-diffusion processes, it was estimated from four-point probe measurements that the doping concentrations are: $N_D \approx 2.2\times10^{20}$ cm^{-3} and, respectively, $N_A \approx 8.4\times10^{19}$ cm^{-3}. Similarly to the case of counter-doped transistors, $N_D > N_A$, but both concentrations are estimated to be high enough to be considered as degenerate doping. The *pn* junction is expected to be formed at the point where $N_D = N_A$, i.e., at the point where the P-donors diffused underneath the doping mask form regions with an effective concentration equal to N_A. [It should be noted that doping was done with a relatively large overlap between the *p*- and *n*-doped regions in order to ensure that the junction can be properly formed within the desired location.]

Fourth, a nanostructure "bridge" is defined between *p*- and *n*-leads using electron-beam lithography and reactive ion etching (RIE), while confirming that the overlapped region is formed within the nanostructure (with a designed length of 1 μm). As a final main step, contact holes are defined and a lift-off process is used to prepare Al electrodes (of ~250 nm in thickness) for the *p*- and *n*-leads. For other purposes (aimed at analyzing tunnel field-effect transistors (TFETs)), some devices also have either a side gate (made in Si), or a top gate (made of Al), while the substrate Si can also be used as a gate, in principle; however, for the purposes of this thesis, these structures are not considered and only non-gated devices will be discussed.

Figure 5.5(a) shows schematically the SOI p^+-n^+ diode structure (for one device), including also the biasing circuit typically utilized for electrical characterization. **Figure 5.5(b)** shows only the top Si layer (around the nanostructured "bridge" between the *p*- and the *n*-lead), along with a simple illustration of the nanoscale depletion layer

containing discrete dopants (Boron (B) acceptors as blue spheres and Phosphorus (P) donors as red spheres); as described in our previous work, inside the depletion layer, ionized B^- acceptors can "compensate" ionized P^+ donors if they are located near each other (within a distance of less than $r_B \approx 2.5$ nm); as such, the dominant type of dopants (in this case, P-donors) are left in larger amounts in the depletion layer, together with some B-acceptors.[22]

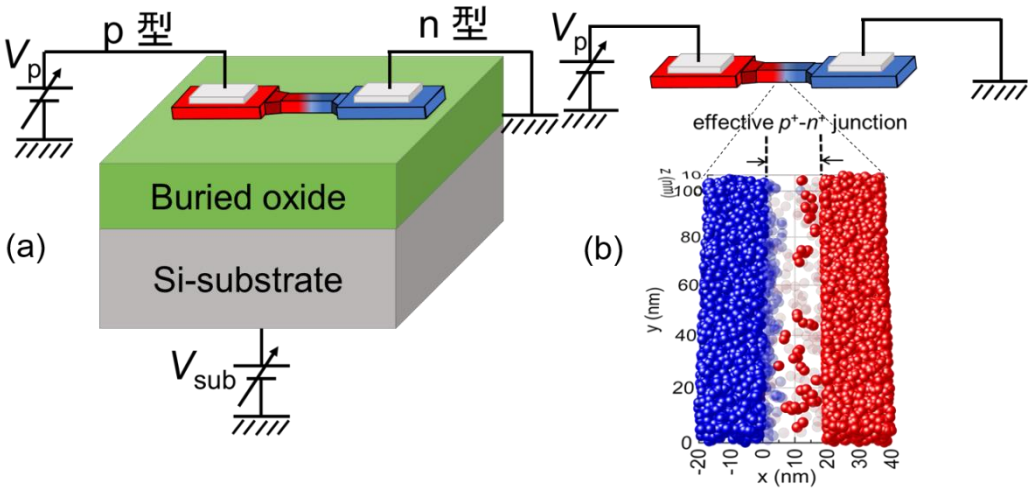

Fig. 5.5 (a) Schematic representation of the device structure for an SOI lateral p^+-n^+ diode, together with typical biasing circuit for electrical characteristics. (b) Zoom-in for the nanostructured "bridge" region between the *p*- and *n*-leads, showing also an illustration of dopant distributions in the leads and in the depletion layer (after "compensation" of closely-located P-B pairs has been taken into account and such pairs have been removed, leaving an "effective" p^+-n^+ junction behind).

A more complete analysis of the "compensation" effect, followed by a "clustering" effect by coupling of (in this case) P-donors into QDs, is given elsewhere.[22] Here, we only point out that such dopant-induced QDs or non-compensated dopants' energy states can be expected to have a significant impact on the BTBT transport, beyond the simple tunneling from one lead into the other. In fact, previous works already reported the possibility of BTBT mediated by P-B pairs (or donor-induced and acceptor-induced energy levels) with deeper states, giving rise to enhanced, sharp current peaks at small forward bias.[4] In other works, it was also reported that "clusters"

of dopants can mediate BTBT by the Coulomb-blockade transport mechanism, giving rise to typical signatures similar to Coulomb diamonds in the stability diagrams.[3] Furthermore, it was shown that the excess-current region exhibits typically a number of current modulations that may be due to the presence of deeper energy states in the depletion layer,[23] likely induced by dopants, although other sources cannot be fully excluded at present.

Regarding the dimensions of the devices, we focused on some of the smallest available. For the batch described here, top-Si layer's thickness is estimated from processing conditions and AFM measurements to be approximately 16 nm (in the co-doped region; thicker in the *n*- or *p*-regions). The width of the EB-patterned nanostructure is used as a parameter, but there is a significant difference between the designed values and real (final) values because of the doping-enhanced oxidation rates and subsequent processing after patterning. As such, a device with a designed width of 220 nm is estimated to have effectively a final width of about 100 nm or less. In addition, it should be noted that the length of the critical region can be considered the depletion-layer width (estimated to be 10-20 nm from the high doping concentrations given above).

With such devices, we looked for examples of IV characteristics that might reveal signatures possibly ascribed to dopants in the depletion layer. For that, we measured the devices in high vacuum, and at low temperatures (typically 8-15 K, as indicated at the sample-stage level) in order to suppress the thermally-activated transport and to become able to focus more clearly on the BTBT transport mechanism. The measurements were carried out in a Nagase IV prober, connected to a semiconductor precision parameter analyzer (Keysight) with a noise level on the order of 10-100 fA. Temperature dependence measurements[21,23] can also show how the

devices generally behave towards room-temperature (which is the condition that we considered more in detail in our theoretical simulation analysis).

5.2.2. Fine features in BTBT tunneling transport

There are several examples obtained for devices as described above and reported in our previous publications or in different theses. Therefore, here we will only provide an example that illustrates such a set of data and that can provide an overview of the type of structures that we can consider in our further analysis. Such an example is given in **Figure 5.6**.

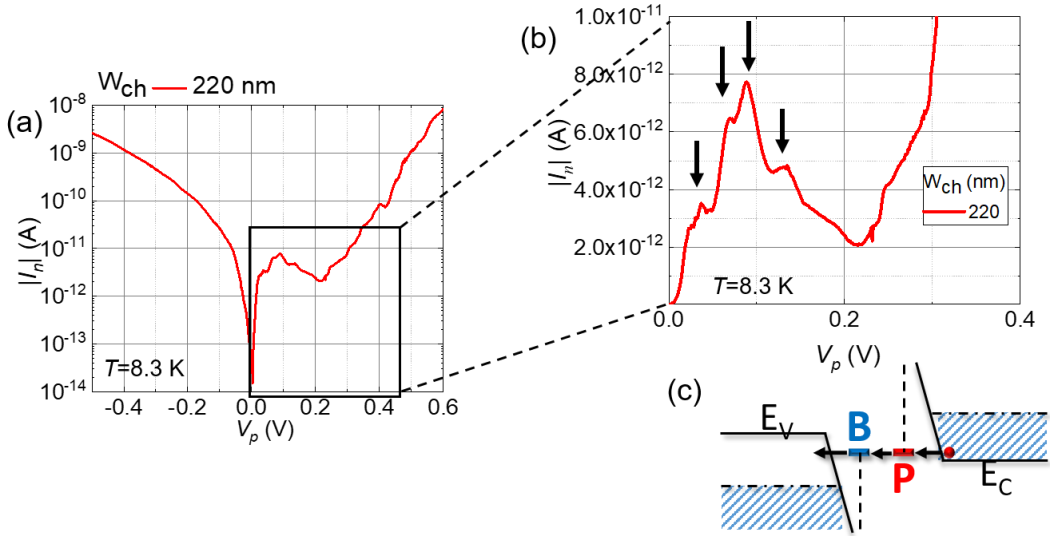

Fig. 5.6. (a) IV characteristics (showing $|I_n|=|I_p|$ on the vertical axis) as a function of V_p, at low temperature (T=8.3 K) in both reverse- and forward-bias regimes. For this device, clear signatures of tunnel (Esaki) diode are observed: a larger reverse-bias current as compared to forward-bias current and a negative differential conductance (NDC) region at small forward bias. (b) Zoom-in on the forward-bias region, indicating (by arrows) sharper current peaks superimposed on the broader NDC peak. (c) Schematic illustration of band diagram (partly drawn) for the small forward-bias regime, indicating a possible BTBT transport mechanism mediated by P-donor and B-acceptor energy states.

First, as shown in **Fig. 5.6(a)**, when plotting $|I|$ versus V_p at low temperatures (here, indicated as T=8.3 K at the sample-stage level), this device exhibits the typical signatures of a tunnel (Esaki) diode: (1) a larger reverse-bias current as compared to the forward-bias current at small biases; (2) a negative differential conductance (NDC)

peak at small forward biases.[7] It should be also noted that there are several current inflections present in both reverse-bias and forward-bias regimes (at higher V_p), which may also be associated with energy states present in the depletion layer. However, here we will focus mainly on the forward-bias regime within the NDC region, where a more distinguishable structure can be seen.

Figure 5.6(b) shows the zoom-in data in this region, with arrows indicating several sharper, enhanced-current peaks, superimposed on the broader NDC peak. These features are generally reproducible and can be expected to be due to BTBT mediated by some energy states in the depletion layer, working as stepping stones in transport. To illustrate this model schematically, **Fig. 5.6(c)** shows a trimmed band diagram picture under this regime, showing also the possibility of P-donor-induced or B-acceptor-induced energy states to bridge the transport path from lead to lead. It should be mentioned that this illustration does not aim at providing any final model about the actual transport mechanism, but only aims at suggesting that dopant states are “involved” likely in such BTBT transport.

5.2.3. Temperature dependence and room-T behavior

Temperature-dependence data are also available for analysis from previous measurements,[21,23] revealing that the fine features described above gradually wash out as temperature is increased. Here, in **Fig. 5.7**, we will only show examples at room temperature[21] (indicated as T=300 K) for several devices with nominally the same design (with designed widths of 200 nm in (a) and 220 nm in (b)).

There are several points to observe from these semi-log plots: (i) generally, reverse-bias current remains high (and even higher than forward-bias current in many cases) – indicating that BTBT occurs through a narrow depletion layer in reverse-bias conditions; (ii) except some noise features, it is difficult to identify distinguishable structures in the *I-V* characteristics at such temperature; (iii) even the presence of the NDC broader peak cannot be confirmed in any device at T=300 K – this may be due to larger excess-current levels that mask the NDC current peak significantly.

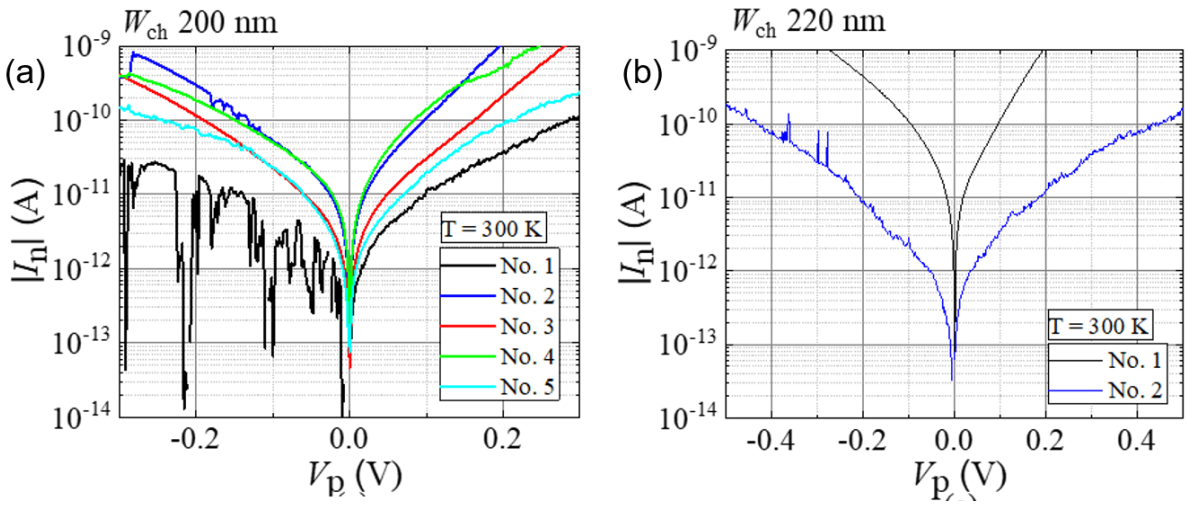

Fig. 5.7 (a)-(b) IV characteristics (showing $|I_n|=|I_p|$ on the vertical axis) as a function of V_p, at room temperature (T=300 K) in both reverse- and forward-bias regimes, for several devices with nominally the same design parameters (labeled as No. #). The only difference between the graphs is the designed width of the nanostructure: (a) 200 nm; (b) 220 nm (although the actual, final width is expected to be <~100 nm for both device types).

This data shows that the p^+-n^+ diodes of this batch still exhibit some signatures of tunnel diodes (such as point (i) explained above), but other signatures cannot be identified. In addition (as indicated in point (ii) above), fine features that could be related to BTBT via discrete dopant states are difficult to distinguish without a more careful and accurate analysis. As such, under the present design, room-temperature data does not allow a more in-depth correlation analysis with our theoretical simulation data (generally carried out at T=300 K). The main reason for this may be related to

the much larger dimensions of our experimental devices when compared to the simulated nanostructure (1-2 order of magnitude larger), which allows a number of transport paths to intermix and hide the features that can be associated with discreteness in the dopant distribution. Other reasons may be related to the doping conditions, such as diffusion length (since this device was fabricated by thermal-diffusion processes) leading to a depletion layer somewhat larger than ideal. Even by a standard calculation, the depletion layer width is estimated to be 10-20 nm, which is roughly one order larger than the active region considered in our simulations. A third reason may be related to the lack of treatment of the phonon-assistance in the simulations, while it is known that phonon-assistance is necessary to satisfy the momentum conservation condition due to indirect-bandgap nature of Si.[24,25] For the dimensions of the present devices, it is still expected that the indirect-bandgap nature is preserved, so the phonon effects must be carefully taken into consideration.

Considering the points above (and other technical details), it is understood that a direct correlation between simulations and experiments cannot be proposed at present, unless the device design is drastically modified. A few device design guidelines will be proposed in the next section, for that purpose.

5.2.4. Guidelines for device design

It is of utmost interest to design and fabricate Si nano-devices that can allow the observation of the features predicted by simulations, in particular due to the very high electric field (built-in electric field) and presence of discrete donor-acceptor pairs in such devices. As mentioned in the previous section, however, the present devices

lack several key properties to attempt such observation, mainly in terms of dimensionality, doping concentration and diffusion length, among others.

As a simple design rule for future devices, we suggest a stronger focus on device dimensionality. Since this mainly depends on the quality of the processing in the fabrication step involving EB-patterning and RIE etching for defining the nanostructure, one way for optimization is to increase the number of devices that could end up having a final width (and thickness) of <10 nm; this can be done by identifying the critical dimensions below which the nanostructures are consumed by subsequent processing and introducing devices with finer-pitch for the width around this value. By controlling also the top-Si layer thickness to be thinner, a nanowire p^+-n^+ diode may be fabricated. Although this can be conceived also by sacrificial oxidation and etching after the definition of the nanostructure, this approach is not suitable because it is known that segregation and aggregation effects are induced by oxidation processes, leading eventually to possible significant reductions of the doping concentrations (and implicitly increases in the depletion-layer width[7]), which is detrimental to our purposes.

As a second device design guideline, the diffusion length under the doping mask must be controlled more precisely, in order to form more abrupt *pn* junctions. For such purpose, the thermal-diffusion processes using furnaces, as used so far, should be replaced with rapid thermal annealing (RTA) processes, optimized to achieve high doping and dopant activation in a much shorter drive-in time than currently used. By implementing such process, it can be expected that higher doping concentrations may be obtained and that the depletion layers of smaller dimensions can be formed between the p^+ and n^+ regions. For obtaining such conditions, RTA tests are needed to find a suitable compromise between enhancing the doping concentration and limiting the diffusion lengths.

Finally, it is critical to have reference devices that can allow a more complete understanding of the physics involved in these devices. For that purpose, we should also fabricate the following types of reference devices: (a) p^+-n^+ diodes with larger dimensions (on the order of 100 nm~10 μm) – by which the macroscopic properties can be identified and analyzed, without considering a significant impact of surface roughness or quantum-confinement effects; (b) uniformly-doped p^+-only and n^+-only (as well as co-doped) transistors – in order to evaluate the contact resistances and to remove the possibility of transport modulation due to QDs formed, for instance, in the nanostructures, away from the depletion layer (not present in such devices); (c) p^+-*i*-n^+ diodes, with the *i*-layer (on the order of 10~100 nm, mainly) working as an additional barrier in the BTBT transport – ideally, such devices could work as tunnel field-effect transistors (TFETs)[26] if proper gating can also be designed.

With an optimal fabrication process, it is expected that the Si-nanowire p^+-n^+ abrupt-junction diodes can provide the low-dimensionality, high built-in electric field and narrow depletion layer to allow the observation of new physics, related also to the presence of discrete dopants in such structures.

5.3. Summary and conclusions

Although a direct parallel cannot be yet made between the extremely low-dimensional devices in simulations and relatively larger devices in our experiment, we showed in this Chapter that atomic-level (or cluster-level) effects likely due to dopants may be distinguishable in our experiments, especially when device dimensions are aggressively scaled down.

In nanoscale SOI-FETs with channels having dimensions on the order of 10-20 nm, counter-doping at high concentrations (at present, only with a specific ratio of N_D:N_A≈3:1) may work to create multiple-donor quantum dots (QDs) that can be probed by single-electron tunneling (SET) at low temperatures. Although further analysis is needed, one can also speculate that acceptors (or donors, which cannot be excluded yet) may also work as charge traps, giving rise to sudden current jumps in the IV characteristics. However, room-temperature operation and analysis requires further optimization of device design. Based on our preliminary results, we proposed several guidelines for future device fabrication that can bring us closer to the situation of treating “clusters” of a few P-donors in nanoscale transistor channels, while also becoming able to investigate the impact of counter-doping with B-acceptors.

In thin SOI p^+-n^+ diodes, when the doping concentrations are sufficiently high and dimensionality is maintained on the order of 10-100 nm at least, we could find examples of IV characteristics that contain signatures that may be ascribed to dopants contributing to band-to-band tunneling (BTBT) transport. Such features appear as current steps, and more prominently as current peaks superimposed on the broader negative differential conductance (NDC) peak typical for a tunnel (Esaki) diode. However, these features are only occasionally observed and only limited to low temperatures (8-15 K), while at higher temperature (or room temperature) such features cannot be distinguished. These devices have many parameters needed to be optimized: dimensionality (thinner and narrower, to become controllable in the scales <10 nm), doping concentration (as high as possible to reduce the depletion layer width to single-digit nm regime), and doping profile (as abrupt as possible, by implementing new techniques such as rapid thermal annealing (RTA)). Such

guidelines are suggested in this Chapter in order to extend the possibilities of bridging more closely the experiments and simulations in the future analysis.

Although the one-to-one correlation in device structures and physical mechanisms of transport cannot be achieved currently, we believe that such an effort of actively looking for, analyzing in depth and proposing ways for optimization from the available data pool is worth doing to aggressively move closer to the idealistic situations analyzed in the theoretical approach. On the other hand, the computational capabilities and software upgrades need also to be actively enhanced to help move toward larger dimensionality (for instance, to become able to simulate devices with typical dimensionality on the order of at least 10 nm).

References

[1]*Single Charge Tunneling*, ed. H. Grabert and M. H. Devoret, New York: Plenum (1992).

[2]L. Esaki, Phys. Rev. **109**, 603 (1958).

[3]G. Prabhudesai, M. Muruganathan, L. T. Anh, H. Mizuta, M. Hori, Y. Ono, M. Tabe, and D. Moraru, Appl. Phys. Lett. **114**, 243502 (2019).

[4]M. Tabe, H.N. Tan, T. Mizuno, M. Muruganathan, L.T. Anh, H. Mizuta, R. Nuryadi, and D. Moraru, Appl. Phys. Lett. **108**, 093502 (2016).

[5]R. Tsujimura, Master Thesis (2020, Shizuoka University).

[6]T. Kaneko, Bachelor Thesis (2021, Shizuoka University).

[7]S.M. Sze, *Physics of Semiconductor Devices*, Second Ed (John Wiley & Sons, Inc., 1981).

[8]K.W. Teng and S.S. Li, Solid State Electron. **28**, 277 (1985).

[9]C. Pandy *et al*., Proceedings of IEEE Silicon Nanoelectronics Workshop (SNW) 2020.

[10]E. Hamid, D. Moraru, J. C. Tarido, S. Miki, T. Mizuno, and M. Tabe, Appl. Phys. Lett. **97**, 262101 (2010).

[11]A. Udhiarto, D. Moraru, T. Mizuno, and M. Tabe, Appl. Phys. Lett. **99**, 113108-1-3 (2011).

[12]K. K. Likharev, "Single-Electron Devices and Their Applications", Proc. IEEE **87**, 606-632 (1999).

[13]P.P. Altermatt, A. Schenk, B. Schmithüsen, and G. Heiser, J. Appl. Phys. **100**, 113715 (2006).

[14]P.P. Altermatt, A. Schenk, and G. Heiser, J. Appl. Phys. **100**, 113714 (2006).

[15]B.I. Shklovskii and A.L. Efros, *Electronic Properties of Doped Semiconductors* (Springer-Verlag, Berlin, 1984).

[16]C. Pandy, G. Prabhudesai, K. Yamaguchi, V N Ramakrishnan, Y. Neo, H. Mimura, and D. Moraru, Appl. Phys. Express **14**, 055002 (2021).

[17]A. Debnath, Mather Thesis (2020, Shizuoka University).

[18]A. Samanta, M. Muruganathan, M. Hori, Y. Ono, H. Mizuta, M. Tabe, and D. Moraru, Appl. Phys. Lett. **110**, 093107 (2017).

[19]D. Moraru *et al*., Nanoscale Res. Lett. **6**, 479-1-9 (2011).

[20]D. Moraru *et al*., Nanoscale Res. Lett. **10**, 372 (2015).

[21]T. Negoro, Master Thesis (2020, Shizuoka University).

[22]G. Prabhudesai, PhD Thesis (2020, Shizuoka University).

[23]Y. Tamura, Bachelor Thesis (2021, Shizuoka University).

[24]A.G. Chynoweth, R.A. Logan, and D.E. Thomas, Phys. Rev. **125**, 877 (1962).

[25]A.G. Chynoweth, G.H. Wannier, R.A. Logan, and D.E. Thomas, Phys. Rev. Lett. **5**, 57 (1960).

[26]A.M. Ionescu and H. Riel, Nature **479**, 329 (2011).

Chapter 6: Conclusions and future work

The objective of this thesis was to study, mainly theoretically, the role of donors and acceptors in silicon nanodevices, focusing in particular on their influence on the tunneling transport properties. The fundamental analysis is organized around the concept of “closely coupled donor-acceptor pair” or “counter-doped nanostructures”, meaning that the co-existence of at least a donor-atom and an acceptor-atom is assumed to play a key role in the overall characteristics; with this assumption, the study aims at revealing what kind of effects are most dominant or most critical, what parameters become essential to control, and what physics can be enhanced or revealed based on such analysis.

The study is based on the background of devices such as metal-oxide-semiconductor field-effect transistors (MOSFETs), tunnel (Esaki) *pn* diodes, and single-electron tunneling (SET) transistors, which offer an extended interpretation of macroscopic and nanoscale devices, with plenty of experimental results to support this interpretation and to show, at the same time, the impact of nanoscale structures resulting from the miniaturization trend. On the other hand, the study is also founded on the background of extensive first-principles (*ab initio*) simulations that deal with Si nanowires (pristine or passivated, undoped or doped with single dopants etc.) or with Si nanocrystals (mainly aiming at revealing the importance of doping, and counter-doping, for photoluminescence and optoelectronics applications). These fundamental studies, including some carried out specifically on the role of dopant atoms or donor-acceptor pairs in Si nanostructures, provided valuable information and original approaches that allowed the work presented in this thesis to be further developed.

On this background, this thesis showed first the role of counter-doping in Si nanoscale transistors, with a simplified structure. In particular, it was shown that clusters of a few P-donors can modulate the current in such devices, while B-acceptors can influence the characteristics by modulating the overall potential in the channel. Although the position of the B-acceptors in these tiny nanostructures does not affect significantly the characteristics, the number of B-acceptors certainly matters and a systematic trend has been demonstrated.

Such donor-acceptor interaction is also expected to play a key role in band-to-band tunneling (BTBT) transport in *pn* diodes, as well, providing possibly an enhancement of the tunneling rates as an additional local electric field enhancement. For this analysis, donor-acceptor pairs have been analyzed in various configurations and different structures. It was found that there are systematic effects on the current level (and finer features) depending on the donor-acceptor distance, but most importantly on the coupling between the dopants and the respective leads. This unique analysis provides new insights into the critical parameters than can allow the modulation of current in Si tunnel diodes, as well as eventually in tunnel field-effect transistors (TFETs).

A summary of each chapter, focusing on the key approaches and findings, is provided next.

In **Chapter 1**, the background of this research was outlined, focusing on the main elements of the research platform. First, the Moore's law was described with the purpose of illustrating how the continuous miniaturization of the transistors brought the dimensionality of these devices (minimum features size) well below 10 nm, and also how the limits of this trend start to become critical (including dopant fluctuations).

Second, prospects for the next-generation electronics have been briefly overviewed; although there are several innovative proposals and intensive research is carried out on several directions, it remains beneficial to consider Si nanostructures as CMOS-compatible framework for such proposals. Third, following the previous point, it was shown how dopant-atoms can actually work as transport paths and what kind of results have been obtained in the past decade in this research direction. Finally, in order to establish the basics of the theoretical treatment, several approaches and main results have been indicated towards the end of this chapter.

In **Chapter 2**, several basic algorithms and approaches utilized in the Quantum ATK package have been presented, mainly focusing on the connection and meaning related to the specific simulations carried out in this thesis. As such, this chapter was aimed at providing all the information needed to understand how the calculations were done, what approximations have been used, and why some approaches were chosen rather than others. This chapter was designed as a platform for defining the procedures for the results reported in the following chapters.

In **Chapter 3**, the simulation results on Si nano-transistors have been presented. In particular, the cases of transport in *n*-type transistors, mediated by a few-donor "cluster", have been introduced, in correlation with cases in which such "clusters" are flanked by acceptor-atoms. It was found that the few-donor "cluster" introduces discrete energy states in the path of electrons, and this can be observed as current peaks in the simulated electrical characteristics. The role of acceptors is not to locally modify the potential, but rather to enhance the potential overall, leading to a shift of the entire characteristics. When the position of B-acceptors is changed, the effect is only minor, but when the number of acceptor-atoms is increased, the shift of the features in the electrical characteristics becomes significant.

In **Chapter 4**, the study was extended to *pn* diodes, with electrostatically-doped leads (at high concentrations), which possess a large built-in electric field in the active region. Furthermore, when dopants (especially donor-acceptor pairs) are introduced in this active region, it was expected that the BTBT current will be modified. It was observed that BTBT current depends most critically on the coupling of the front-most dopants and corresponding leads, increasing as the dopant-lead distance decreases. In addition, BTBT current also depends on the donor-acceptor distance, as also illustrated by the analysis in Chapter 4. Orientation of the Si nanowire (or of the donor-acceptor pair) can also play a significant role, although further analysis is needed. These findings have been analyzed from different perspectives in this chapter.

In **Chapter 5**, as possible targets for comparison with experimental results, a few examples were presented from the *I*-*V* characteristics of co-doped Si nano-transistors and, respectively, highly-doped Si nanoscale *pn* diodes. For the co-doped Si nano-transistors, our preliminary measurements showed that clusters of P-donors most likely dominate the transport, especially if the device dimensions are reduced to the order of ~10 nm. This was evidenced by the observation of single-electron tunneling (SET) behavior in several of such devices. Charging effects have also been observed, with a high likelihood of being due to B-acceptors, but further analysis is needed to confirm this point. For the nanoscale *pn* diodes, due to the high doping, we also expected that the depletion-layer dimensions are in the order of ~10 nm. As such, BTBT transport was confirmed in several devices, i.e., a high reverse-bias current and a negative differential conductance (NDC) peak in forward-bias regime. More importantly, however, we show examples which (as also reported previously) illustrate the possibility of BTBT mediated by donor-acceptor pairs (or, more precisely, energy states induced by donors and, respectively, acceptors). These results require further

analysis and new designs for full confirmation. Therefore, for both types of devices, some guideline for optimization of the device design are proposed, aiming for opening new pathways for addressing such physics experimentally and allowing more accurate comparisons with the simulation results.

Finally, **Chapter 6** presents the summary and conclusions of each chapter, making correlations between the parts and suggesting possible further extensions.

Overall, these results contribute to revealing new physics at atomistic level that could be leveraged for future ultimately-scaled Si nano-devices. This way, new insights can be incorporated into the operation mechanisms of future devices, but also new designs can be considered for the future generations of electronics.

As future work, it is also of interest to extend this kind of research to other nanoscale materials. For example, one topic of interest is the extension to carbon nanotubes (CNT), possibly working as bridges between nano-leads. It is expected that, if impurities (defects) are present in such structures, the physics contained in this thesis can be smoothly extended to such cases, as well.

List of Publications

1) Chitra Pandy, G. Prabhudesai, K. Yamaguchi, V N Ramakrishnan, Y. Neo, H. Mimura, and D. Moraru, “Electron transport via a few-dopant cluster in the presence of counter-dopants in silicon nanowire transistors”, Appl. Phys. Express **14**, 055002 (2021).

***Peer-reviewed international conference proceedings**

2) C. Pandy, A. Debnath, K. Yamaguchi, T. Teja Jupalli, G. Prabhudesai, V N Ramakrishnan, Y. Neo, H. Mimura, and D. Moraru, “Effects of co-doping on the transport characteristics of nanoscale *n*-type silicon-on-insulator transistors”, IEEE Silicon Nanoelectronics Workshop (IEEE SNW) 2020 (published in IEEE Xplore (2020)).

List of Conference Presentations

1) Chitra Pandy, K. Yamaguchi, Y. Neo, H. Mimura, M. Tabe, and D. Moraru, “Theoretical study of the impact of a donor-acceptor pair on tunneling current in Si nanodiodes”, The 19th International Conference on Global Research and Education (inter-Academia) 2021 (accepted for presentation in Oct. 2021).

2) A. Debnath, T. Teja Jupalli, Chitra Pandy, and D. Moraru, “Study of single-electron tunneling transport through coupled-donor molecule in low-doped SOI-FETs towards elevated temperature”, The 7th International Symposium towards the Future of Advanced Researches at Shizuoka University (ISFAR-SU) (Shizuoka Univ., virtual conference, Mar. 2021).

3) C. Pandy, G. Prabhudesai, K. Yamaguchi, V N Ramakrishnan, Y. Neo, H. Mimura, and D. Moraru, “Study of electrical characteristics of codoped Si-nanoscale transistors”, 6th International Conference on Nanoscience and Nanotechnology (ICONN) (SRM Institute of Science and Technology (SRM IST – virtual conference, Feb. 2021).

4) C. Pandy, A. Debnath, K. Yamaguchi, T. Teja Jupalli, G. Prabhudesai, V N Ramakrishnan, Y. Neo, H. Mimura, and D. Moraru, “Effects of co-doping on the transport characteristics of nanoscale *n*-type silicon-on-insulator transistors”, IEEE Silicon Nanoelectronics Workshop (IEEE SNW) (virtual conference, June 2020).

5) Singh Rohitkumar Shailendra, Chitra Pandy, V.N. Ramakrishnan, Hidenori Mimura, “AC gain analysis of Multi-stage common source amplifier using GAA-CNTFET”, 5th IEEE International Conference on Devices, Circuits and Systems (ICDCS’20) (virtual conference, March 2020).

6) Singh Rohitkumar Shailendra, Chitra Pandy, V.N. Ramakrishnan, Hidenori Mimura, “Power delay analysis of half and full adder circuits using GAA CNTFET”, The 67th JSAP Spring Meeting, (Tokyo - virtual conference, Mar. 2020).

7) Chitra Pandy, D. Moraru, and H. Mimura, “*Ab initio* study of the effects of co-doping on the electronic properties of silicon nanostructures”, The 4th International Symposium on Biomedical Engineering (ISBE) (Hamamatsu, Nov. 2019).

8) Chitra Pandy, V N Ramakrishnan, Hidenori Mimura, “Sensitivity study on different gate dielectric dependence of DG-CNTFET using atomistic simulation

NEGF approach", International Conference on Solid State Devices and Materials (SSDM 2019) (Nagoya, Sept. 2019), Extended Abstracts, pp 913-914.